Department of Physics and Astronomy
Heidelberg University

Bachelor Thesis in Physics
submitted by

Isabel Kantak

born in Hamburg (Germany)

2024

Developing an analysis task in O^{2}Physics for detection of the χ_c in ALICE at the CERN LHC

This Bachelor Thesis has been carried out by Isabel Kantak at the
Physikalisches Institut Universität Heidelberg, Heidelberg (Germany)
under the supervision of
Prof. Dr. Johanna Stachel

Abstract

The ALICE Run 3 O^{2}Physics analysis framework is divided into several Physics Working Groups (PWGs). This thesis focuses on implementing an analysis task in the Dilepton-Quarkonia (DQ) PWG analysis framework. The new analysis task, AnalysisDileptonPhoton, reconstructs the radiative decay of $\chi_c \to \gamma + J/\psi \to \gamma e^+e^-$ in Monte Carlo simulations and in ALICE Run 3 data. During the task development and to obtain several performance parameters, a Monte Carlo (MC) simulation was used with 5 forced χ_{c1} and 5 forced χ_{c2} radiative decays per event. The MC reconstructed matched triple candidates $\chi_c \to \gamma e^+e^-$ delta mass ($\Delta m = m_{\gamma e^+e^-} - m_{e^+e^-}$) distribution, which suppresses the experimental J/ψ mass resolution, exhibits two clear peaks corresponding to the masses of χ_{c1} and χ_{c2}, respectively. The masses of χ_{c1} and χ_{c2} were determined as $\mathrm{m}_{\chi_{c1}} = (3509.9 \pm 0.5)$ MeV/c and $\mathrm{m}_{\chi_{c2}} = (3554.9 \pm 0.7)$ MeV/c, respectively, by fitting an asymmetric Gaussian to the peaks. Moreover, it was possible to reconstruct χ_c down to a transverse momentum of 0 GeV/c. Furthermore, the study determined the acceptance and reconstruction efficiency of triple candidates γe^+e^- from χ_c as a function of transverse momentum p_T.

Das ALICE Run 3 O^{2}Physics Analysis Framework ist in mehrere Physics Working Groups (PWGs) unterteilt. Diese Arbeit konzentriert sich auf die Implementierung einer Analysestruktur in das Dilepton-Quarkonia (DQ) PWG Analysis Framework. Die neue Analysestruktur, AnalysisDileptonPhoton, rekonstruiert den Strahlungszerfall $\chi_c \to \gamma + J/\psi \to \gamma e^+e^-$ in Monte Carlo (MC) Simulationen und ALICE Run 3 Daten. Während der Entwicklung der Analysestrukur und um verschiedene Leistungsparameter zu erhalten, wurde eine Monte Carlo Simulation mit 5 erzwungenen χ_{c1} und 5 erzwungenen χ_{c2} Strahlungszerfällen pro Ereignis verwendet. Die drei MC rekonstruierten Teilchenkandidaten γe^+e^-, welche mit MC Informationen auf den gleichen χ_c Zerfall getestet wurden, weisen eine Delta-Massenverteilung ($\Delta m = m_{\gamma e^+e^-} - m_{e^+e^-}$) mit zwei deutlichen Maxima auf, deren Peaks den Massen von χ_{c1} beziehungsweise χ_{c2} entsprechen. Die Delta-Massenverteilung unterdrückt die experimentelle J/ψ Massenauflösung. Die Masse von χ_{c1} und χ_{c2} wurde als $\mathrm{m}_{\chi_{c1}} = (3509.9 \pm 0.5)$ MeV/c und $\mathrm{m}_{\chi_{c2}} = (3554.9 \pm 0.7)$ MeV/c bestimmt, indem eine asymmetrische Gaußfunktion an die Peaks angelegt wurde. Darüber hinaus konnte χ_c bis zu einem transversalen Impuls p_T von 0 GeV/c rekonstruiert werden. Außerdem wurde die Akzeptanz und die Rekonstruktionseffizienz der drei Teilchenkandidaten γe^+e^- von χ_c in Abhängigkeit vom transversalen Impuls p_T bestimmt.

Contents

Acronyms

O^2 Online-Offline

O^2Physics O2Physics analysis framework

ALICE A Large Ion Collider Experiment

AO2D Analysis Object Data

CA Cellular Automaton

CTF Compressed Time Frames

CYSS Cylindrical Structural Shell

DCA Distance of Closest Approach

DQ Dileptons-Quarkonia

EM Electromagnetic Probes

EMCal Electromagnetic Calorimeter

EPN Event Processing Nodes

FLP First Level Processor

GEM Gas Electron Multiplier

IB Inner Barrel

ITS2 Inner Tracking System 2

KF Kalman Filter

LHC Large Hadron Collider

MAPS Monolithic Active Pixel Sensors

MC Monte Carlo

MFT Muon Forward Tracker

MLs Middle Layers

OB Outer Barrel

OLs Outer Layers

PCM Photon Conversion Method

PHOS Photon Spectrometer

PID Particle Identification

PWG Physics Working Group

QCD Quantum Chromodynamics

QGP Quark Gluon Plasma

ROC ReadOut Chambers

SM Standard Model

TOF Time Of Flight

TPC Time Projection Chamber

TRD Transition Radiation Detector

List of Figures

List of Tables

1. Introduction

Charmonia ($c\bar{c}$) are bound states of charm and anticharm quarks and are distinguished by their differing masses and binding energies. They are useful probes to study the properties of the medium formed in heavy-ion collision as their production is influenced by the Quark-Gluon Plasma (QGP). At low energies (like RHIC), in the presence of a QGP there is a suppression of the J/ψ production, whereas at high energies (like LHC), the J/ψ production is enhanced [1]. The decay of higher charmonium mass states significantly contributes to J/ψ production [2]. This feed-down is mainly due to the radiative decay from $\chi_c \to \gamma + J/\psi$. Therefore, studying the radiative decay of χ_c is crucial.

In order to study the radiative decay of χ_c, it is necessary to be able to reconstruct it. However, the reconstruction of this decay is not yet implemented in the ALICE Run 3 O^2Physics analysis framework. This thesis presents the implementation of the analysis task for reconstructing $\chi_c \to \gamma + J/\psi \to \gamma e^+ e^-$ with O^2Physics, along with the full analysis of a Monte Carlo simulation to determine the mass resolution of χ_c and the p_{T} dependent reconstruction efficiency. To facilitate the understanding of the developed analysis task, AnalysisDileptonPhoton, it is necessary to review certain physical concepts and to provide an explanation of the ALICE detector, and particularly the corresponding Online-Offline (O^2) computing system, before introducing the new analysis task.

Firstly, Chapter 2 introduces briefly the physics fundamentals for this thesis, the standard model (SM), the Quark-Gluon Plasma (QGP) and the J/ψ and χ_c charmonium states. Secondly, the upgraded A Large Ion Collider Experiment (ALICE) detector during the Long Shutdown 2 with its research goal, as well as the main detector systems are described in chapter 3. The central barrel detectors Inner Tracking System 2 (ITS2) and Time Projection Chamber (TPC) are given in a bit more details (Section 3.2 and 3.3). The general tracking of particles in the ITS2 and TPC, the detection of photons using the Photon Conversion Method (PCM) and the reconstruction of V0 particles through two opposite charged daughter particles are described in Section 3.4.

Thirdly, the ALICE Run 3 Online-Offline (O^2) computing system developed for the processing and compression of the data from the continuous detector readout, as well as for the analysis of the compressed data is described in Section 4.1. The O^2Physics analysis framework is a component of the O^2 computing system and is responsible for the data analysis. Section 4.2 outlines the structure of the Physics Working Groups (PWGs) in the O^2Physics analysis framework. Section 4.3 explains the data workflow within the PWG, and the layout of an analysis task. The developed analysis task

was implemented in the Dileptons-Quarkonia (DQ) analysis framework (Section 4.4) because it allows for the reconstruction of electron-positron pairs. The DQ section focuses on the data skimming process and the files that are modified when implementing the new task. The reconstruction of the χ_c requires not only the electron-positron pairs but also a photon candidate table. This table is obtained from the Electromagnetic Probes (EM) analysis framework described in Section 4.5.

Chapter 5 provides a detailed description of the developed analysis task, AnalysisDileptonPhoton, which aims to reconstruct the radiative decay of χ_c. Section 5.2 outlines the structure of AnalysisDileptonPhoton. Sections 5.3, 5.4 and 5.5 provide a detailed description of the additions made to the DQ analysis framework to enable the reconstruction of χ_c in Monte Carlo simulations and ALICE Run 3 data. Three different types of reconstructions are considered: MC generated true, MC reconstructed and MC reconstructed matched. Finally, Section 5.6 defines the O2 executables required for running the task.

During the development of the analysis task, a specific Monte Carlo simulation with forced radiative χ_c decays was used for debugging and afterwards to estimate several performance parameters. Chapter 6 provides the parametrisation of the transverse momentum p_{T} distribution of χ_{c1} and χ_{c2} used for the Monte Carlo simulation. Chapter 7 analyses the Monte Carlo simulation, investigating photon reconstruction and dielectron reconstruction separately and together. The masses of χ_{c1} and χ_{c2} with their mass resolution, as well as the p_{T} dependent acceptance and reconstruction efficiency, are determined.

2. Theoretical Background

This chapter introduces the Standard Model, the Quark-Gluon-Plasma and two Charmoniums: the J/ψ and the χ_c. Section 2.1 provides a brief introduction to the Standard Model. Then the deconfined phase of matter, known as Quark-Gluon-Plasma, is explained in Section 2.2, since this phenomenon is being studied with the A Large Ion Collider Experiment (ALICE) aparatus. Next, the J/ψ meson and the χ_c meson are characterised in Sections 2.3.1 and 2.3.2, respectively, because they are key observables to study the Quark-Gluon-Plasma, and the main topic of this thesis.

2.1 Standard Model

The Standard Model (SM) is a theory in particle physics that explains how three fundamental forces and 12 fundamental spin-half particles interact (on the left of Fig. 2.1). The SM can describe nearly all experimental data. The 12 fundamental particles are made up of 6 leptons and 6 quarks as well as their antiparticles, grouped into pairs and generations. The first generation of quarks are consists of the up (u) and down (d) quarks which are the lightest and most stable quarks. This generation corresponds to the electron (e^-) and the electron neutrino (υ_e) which is the first generation of the leptons. The fundamental particles of the first generation make up all stable matter. The second and third generations of quarks are strange (s) and charm (c) as well as top (t) and bottom (b) quarks. These higher generations are heavier and less stable. The muon (μ) and tau (τ) and their corresponding neutrinos (υ_μ, υ_τ) form the second and third generations of leptons. The main difference between quarks and leptons is that quarks can only exist confined in hadrons due to the increasing force of their interaction as the distance between them increases, whereas leptons can exist freely [3, 4].

Figure 2.1 shows the SM with its fundamental particles and the exchange particles of the fundamental forces. The SM takes into account the electromagnetic, weak and strong forces in order to explain how these forces affect all matter. It neglects gravity because it is extremely weak on a minuscule scale. The electromagnetic force has an infinite range and is stronger than gravity. At the subatomic level, the weak and strong forces are dominant and only manifest themselves over a very short range. Each of the three forces uses force-carrying particles (bosons) to exchange energy. The force-carrying particle of the electromagnetic force is the photon (γ), the weak force has both the W and Z bosons, and the strong force uses the gluon (g) as the exchange boson [3, 4].

The SM is not yet complete and leaves some questions unanswered. For example, the theory only considers three of the four fundamental forces, and it cannot explain dark

matter or the loss of antimatter [4].

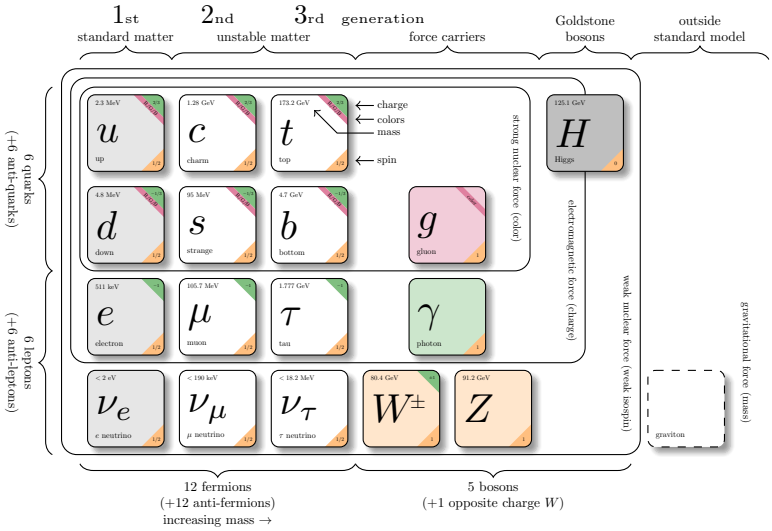

Figure 2.1: The fundamental particles and force carrier bosons of the Standard Model of particle physics as well as their corresponding forces [5]

2.2 Quark Gluon Plasma

The Quantum Chromodynamics (QCD) explains the strong interaction of the Standard Model. One component of the QCD is the theory of asymptotic freedom, which describes the effect that the strong coupling constant α_s approaches zero at high transferred momentum. This behaviour of α_s hits that there is a matter phase transition point between confined and deconfined matter. At high densities or temperatures nuclear matter undergoes a phase transition to deconfined matter where quarks and gluons exist freely which is called Quark Gluon Plasma (QGP). In this state, its constituents interact with each other through long-range gauge-fields, hence the name plasma [6, 7]. Depending on the plasma parameter (Γ), the plasma can be a gas, a liquid or a solid. In the case of the QGP, it behaves more like a perfect fluid [8].

The development of the QGP in a heavy-ion collision at LHC energies is shown in Figure 2.2. Firstly, in order to produce an extremely high density parton region above the critical energy density of the QGP ($T_c = (0.7 \pm 0.2)$ GeV fm^{-3} [1]), strongly accelerated massive ions must collide head-on. The centre distance of the colliding nuclei is represented by the collision parameter 'b'. The smaller the value of b, the greater the number of nucleus involved in an inelastic interaction. Nucleons that are not involved in the collision (spectators) continue to move along the beam direction after the impact. The initial state is immediately after the collision, where partons collide in smaller-Q^2 inter-

actions and large-Q^2 interactions. Q^2 represents the square of the 4-momentum transfer in a two-particle interaction. During the weakly coupled pre-equilibrium phase, softer partons are created through smaller-Q^2 interactions between the partons, allowing a strongly coupled QGP phase to develop. At large-Q^2 interactions, high-momentum gluons and heavy quarks can be generated. The figure illustrates a trajectory of a gluon and charm quark, for example. Less than 1 fm/c after the collision the QGP reaches a state of equilibrium and expands. The charm quark losses energy due to interactions with different quarks and gluons in the medium. The amount of energy loss by the quarks and gluons depends on various parameters, such as colour charge, momentum, mass, and whether the interaction is elastic or inelastic. This information can provide insight into the properties of the QGP. The QGP expands and cools down. The quarks and gluons which are below the transition temperature hadronise mainly into pions, kaons and protons. At approximately 10 fm/c after the initial collision, the temperature of the QGP reaches the freeze-out temperature and the particles as well as their momenta are fixed. The ALICE detector measures the particles 10^{15} fm/c after the heavy ions collided [1, 9, 10]. The measurement of the resulting hadronic particles with the ALICE detector in Run 3 is described during Chapter 3.

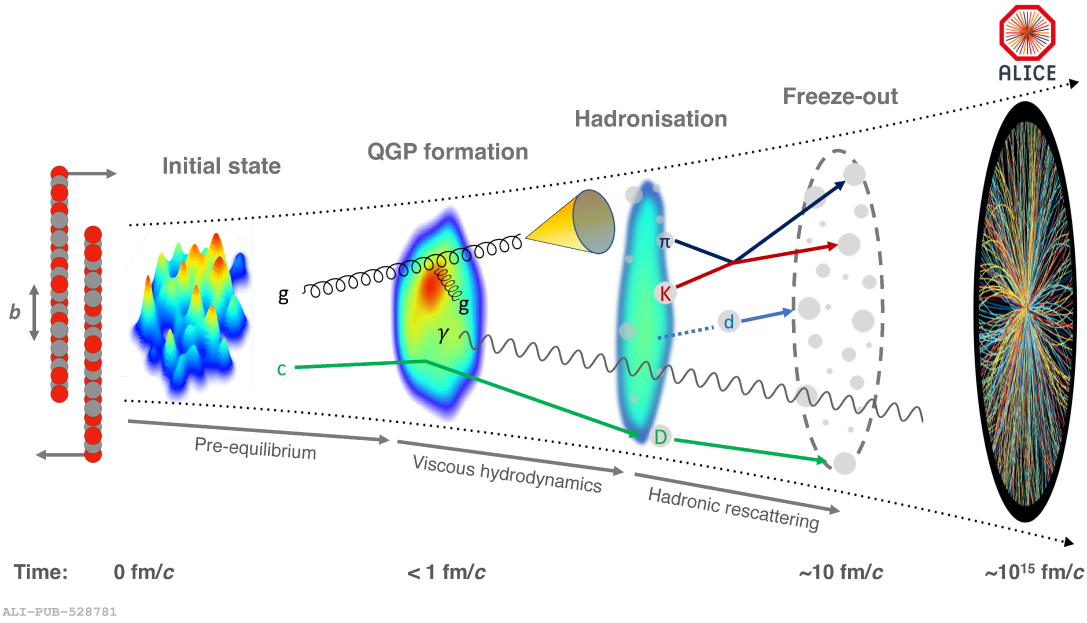

Figure 2.2: Phases of Quark-Gluon-Plasma beginning at the collision of the highly accelerated heavy ions until the detection with the ALICE detector [9].

In heavy-ion collisions at low energies (RHIC) the production of J/ψ is suppressed in the QGP whereas at high energies (LHC) the production in the QGP is enhanced (Figure 2.3). This suppression of J/ψ at low energies is due to the fact that the average number of charm-quark pairs (red dots) is less than one so that the charm quark or antiquark

interact with other quarks (u, d, s) to form D mesons (purple circles) during cooling phase. At high energies, the multiple produced charm (c) and anticharm ($\bar{c}$) quarks can interact again to D mesons or form a charmonium J/ψ particle at hadronization [1, 11].

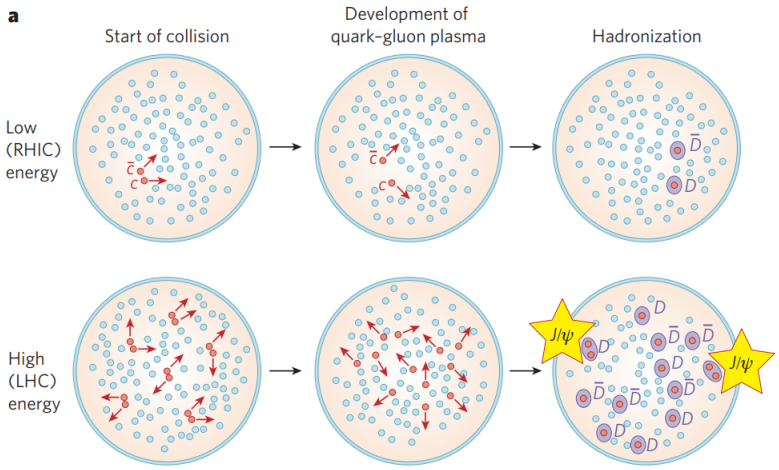

Figure 2.3: Charmonium suppresion: At low energies, the QGP reduces the interactions between the only $c\bar{c}$ pair (red dots) produced. During hadronisation, other quarks such as u, d and s pair up with c or $\bar{c}$ to form D mesons (purple circles). At high energies, numerous $c\bar{c}$ pairs are created. This time, at hadronisation, J/ψ mesons can be formed from various $c\bar{c}$ original pair [1]

2.3 Charmonium

With the discovery of the J/ψ in 1974 [12, 13], a new particle family was discovered: Charmonium ($c\bar{c}$). An overview of the different charmonium states with their most dominant transitions, excluding single photon transitons, is given in Figure 2.4. They are sorted after mass and quantum numbers J^{PC} [14]. The mesons J/ψ and χ_c are both members of the Charmonium family and are part of the developed task. They are described in more detail in the following subchapters.

2.3.1 The J/ψ meson

Almost 50 years ago, the particle J/ψ was discovered at the same time by two independent groups led by Samuel Chao Chung Ting and Burton Richter [12, 13]. The data from both groups showed a new heavy particle with a surprisingly small width. These data could only be explained by the fact that the measured particle was composed of a new quark (charm quark (c), which had already been proposed in the GIM Mechanism (1970). The J/ψ consists of a charm (c) quark and an anticharm ($\bar{c}$) quark. It has a full

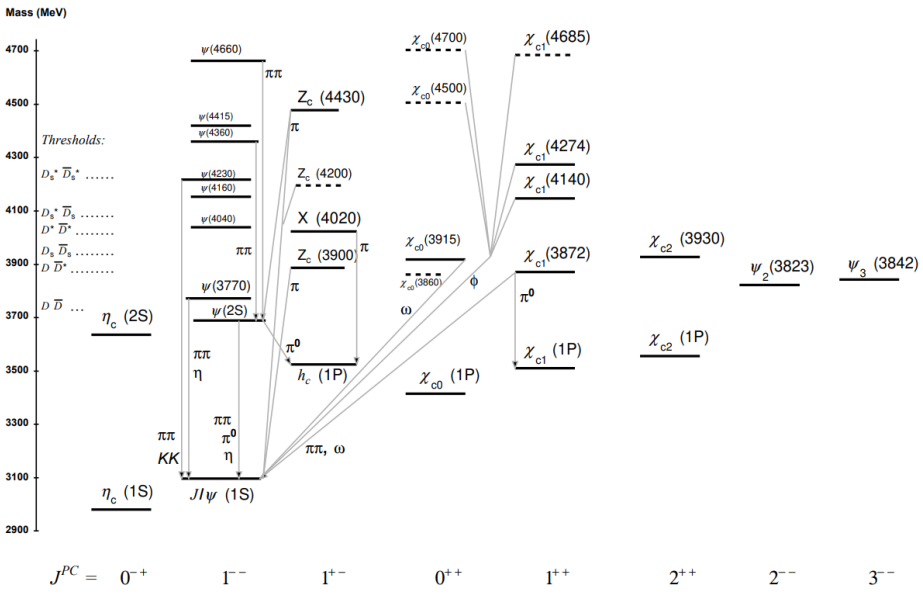

Figure 2.4: Charmonium states. Arrows show the most dominant hadronic transitions. For clarity, single photon transitions are omitted. The charmonium states are organised into columns based on their Quantum numbers J^{PC} (J=spin, P=parity, C=charge-conjugation) [14]

width at half maximum of $\Gamma = (92.6 \pm 1.7)$ keV/c^2 and a mass of $m = (3096.900 \pm 0.006)$ MeV/c^2 [14]. Although the J/ψ has a long lifetime for such a heavy particle which is due to the $D\bar{D}$-threshold, it is unstable. Table 2.1 lists the most important branching ratios of the J/ψ decay modes.

$J/\psi(1S)$ DECAY MODES		Fraction (Γ_i/Γ)	Scale factor/ Confidence level	p (MeV/c)
hadrons		(87.7 ± 0.5) %		–
virtual $\gamma \rightarrow$ hadrons		(13.50 ± 0.30) %		–
ggg		(64.1 ± 1.0) %		–
γgg		(8.8 ± 1.1) %		–
e^+e^-		(5.971 ± 0.032) %		1548
$e^+e^-\gamma$	[*hhaa*]	(8.8 ± 1.4) $\times 10^{-3}$		1548
$\mu^+\mu^-$		(5.961 ± 0.033) %		1545

Table 2.1: Decay channels and branching ratios of J/ψ meson [14]

The J/ψ can be produced in both prompt or non-prompt modes. J/ψ from the decay of higher charmonium mass states (indirect production) and from hard scattering in hadron collisions (direct production) are termed prompt productions. Whereas J/ψ from the decay of beauty hadrons are non-prompt productions [15, 16, 17].

2.3.2 The χ_c meson

The χ_c (1P) triplet P-wave states are heavier charmoniums than the J/ψ, but are still below the D$\bar{\text{D}}$-threshold [18]. The χ_c triplet states differ in their spin-orbit and tensor interactions, leading to different masses (Table 2.2). In the case of e^+e^-annihilation, χ_c cannot be produced directly due to the quantum numbers $J^{PC} = J^{++}$ [19]. χ_c mesons can be promptly produced at the interaction point in hadronic collisions or as a result of the decay of higher-mass quarkonium states. Whereas, the decay of B-hadrons produces non-prompt χ_c [18, 20].

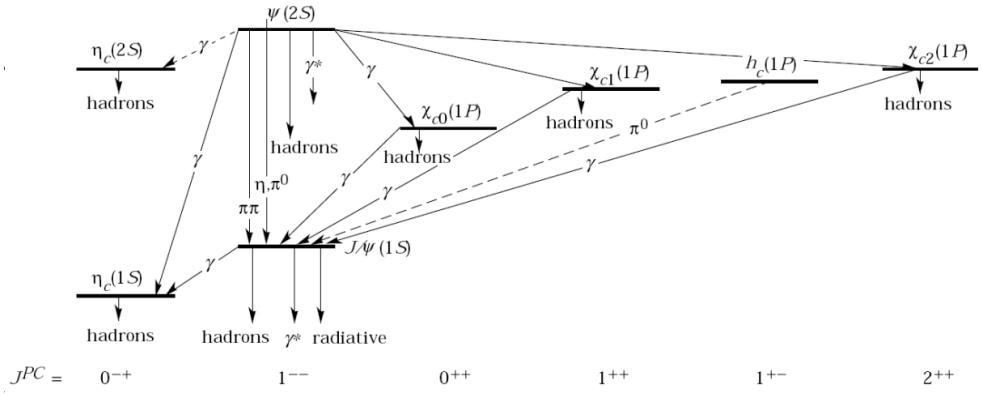

Figure 2.5: Charmonium states below D$\bar{\text{D}}$ threshold with Quantum numbers J^{PC} (J=spin, P=parity, C=charge-conjugation) and decay channels [21]

Figure 2.5 shows the possible decays of charmonium states below the D$\bar{\text{D}}$-threshold. This includes the radiative decay of χ_c to J/ψ: $\chi_c \to J/\psi + \gamma$. This electric dipole transition accounts for about 25% of the prompt J/ψ production [18, 19].

	$n^{2S+1}L_J$	J^{PC}	mass $[MeV/c^2]$	full width Γ $[MeV/c^2]$	$\mathcal{BR}$ [%]
χ_{c0}	1^3P_0	0^{++}	3414.71 ± 0.30	10.8 ± 0.6	1.40 ± 0.05
χ_{c1}	1^3P_1	1^{++}	3510.67 ± 0.05	0.84 ± 0.04	34.3 ± 1.0
χ_{c2}	1^3P_2	2^{++}	3556.17 ± 0.07	1.97 ± 0.09	19.0 ± 0.5

Table 2.2: Selected χ_c properties; $\mathcal{BR}$ (branching ratio) of the radiative decay $\chi_c \to \gamma + J/\psi$; numbers taken from [14]

Table 2.2 lists some of the properties of the χ_c states. The branching ratio $\mathcal{BR}$ of $\chi_{c0} \to \gamma + J/\psi$ (only 1%) is significantly smaller than $\mathcal{BR}$ of χ_{c1} (34%) and χ_{c2} (19%). Therefore, χ_{c0} will not be taken into account in the developed task.

3. The ALICE detector

The European Organization for Nuclear Research (CERN) [22] uses several accelerators, such as the Linear accelerator (Linac) or the Proton Synchroton (PS), to accelerate protons or lead ions before they enter the Large Hadron Collider (LHC) [22]. On the 27 km long ring of the LHC there are four collision points equipped with detectors [23]. One of these detectors is the A Large Ion Collider Experiment (ALICE) detector. The ALICE collaboration has constructed the ALICE detector to investigate the physical properties of strongly interacting matter at extremely high energy densities, known as QGP. The aim of this research is to study how QGP evolves in order to learn more about how matter is organised and the processes that bind quarks and gluons [24, 25, 26].

Section 3.1 discusses the layout of the ALICE detector and briefly describes the detectors that are important for reconstructing the χ_c radiative decay ($\chi_c \rightarrow \gamma + J/\psi$). Sections 3.2 and 3.3 provide a detailed description of the Inner Tracking System 2 (ITS2) and Time Projection Chamber (TPC), respectively, as they serve as the main tracking detectors for the ALICE detector. Section 3.4 deals with the reconstruction of particles in Run 3. The general approach to particle tracking in the detector is outlined in Section 3.4.1. Next, the tracking of particles in ITS2 and TPC in ALICE Run 3 are discussed. Section 3.4.3 describes the method used to measure photons that will be used in the new task and finally the reconstruction of V0 particles is described (Section 3.4.4).

3.1 The ALICE detector layout

The ALICE detector was upgraded during the Long Shutdown 2 in order to increase the data acquisition rate and to improve the track resolution, as well as to detect more precisely particles with a short lifetime [27]. The new setup for Run 3 and Run 4 of the ALICE detector is shown in Figure 3.1. The detailed upgrades for each system are described in [28].

The entire ALICE detector with all its different detectors weighs 10,000 tonnes and has dimensions of 26x16x16m^3 [29]. At the centre of the detector is the Inner Tracking System 2 (ITS2) [30, 31, 32], which surrounds the beam pipe. Next, is the Time Projection Chamber (TPC) [33, 34], which tracks and identifies particles by measuring their specific energy loss $\mathrm{d}E/\mathrm{d}x$. The ITS2 and TPC are followed the by the Transition Radiation Detector (TRD) [35, 36] and Time Of Flight (TOF) [37, 38], which are particle identification detectors. The TRD uses transition radiation to identify electrons. It can also provide up to six track points for charged particles to improve the momen-

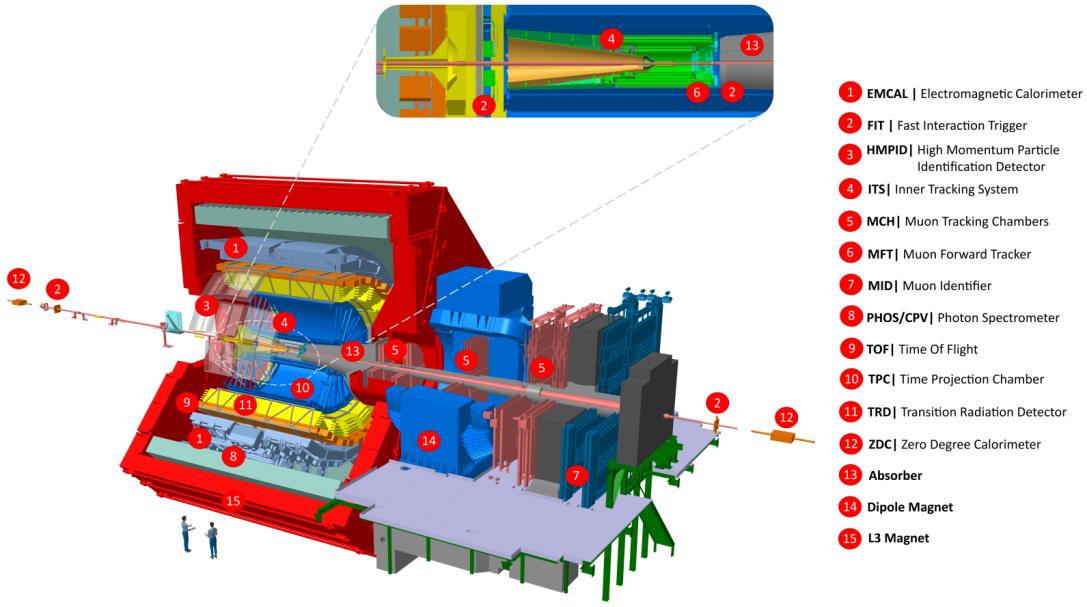

Figure 3.1: The upgraded setup of the ALICE detector for Run 3 [28]

tum determination and the particle identification [28]. The TOF detector measures the time particles need to reach it from the interaction point. These high-precision times, obtained using Multigap Resistive Plate Chambers (MRPCs), are used to determine the velocities of the particles. The detector helps to identify hadrons and electrons [28, 38]. The two electromagnetic Calorimeter, Electromagnetic Calorimeter (EMCal) [39, 40] and Photon Spectrometer (PHOS) [41, 42, 43], are important for the measurement of electrons and photons. The EMCal is a Pb-scintillator sampling calorimeter split into two different regions in azimuth (EMCal and DCal (Di-Jet Calorimeter)), both located 4.5m from the beamline [28, 40]. Both EMCal and PHOS use Avalanche Photo Diode (APD) as readout. The PHOS is made of lead-tungstate crystals ($PbWO_4$) and surrounded by DCal. It measures electromagnetic showers to determine the total energy of photons and assumes they originate from the primary vertex. It also determines the photon yield (for energies from 0.1 to 100 GeV) [28, 43]. The other parts of the ALICE detector are not relevant to the decay in this study.

3.2 The Inner Tracking System 2

The Inner Tracking System 2 (ITS2) can reconstruct the primary and secondary vertices of heavy flavour hadron decays, identify low-momentum particles and improve the resolution of high-momentum particles which are detected in the TPC. During the Long Shutdown 2 of the LHC, the ITS2 was upgraded to a seven-layer layout, as compared to the six layers of the original setup. The layout of the seven layers of the ITS2 is shown

in Figure 3.2. The seven layers are grouped into Inner Barrel (IB) and Outer Barrel (OB). The IB consists of the three innermost layers, starting at a radial distance of 22 mm from the interaction point. The OB consists of four layers divided into two groups ending at 400 mm from the beam line. The OB can be split further in the Middle Layers (MLs) and Outer Layers (OLs) consisting each of 2 layers. The exact radii of the seven layers are given in Table 3.1. The layers comprise ALIPIDE chips, which are Monolithic Active Pixel Sensors (MAPS) utilising CMOS imaging technology. This technology enables the integration of the sensor and the readout circuit to be integrated into a single silicon layer, resulting in allowing the thinning of the silicon layers down to 50 μm and 100 μm. This reduces the material budget to 0.36% X_0 in the inner barrel per layer and 1.10% X_0 in the outer barrel per layer[27, 28, 31, 30, 32].

The upgrade of the ITS2 enhanced the precision of track reconstruction for primary vertex and heavy flavour hadron decays. This improvement was achieved by increasing the resolution of impact parameters in the transverse plane and beam axis by at least a factor of three each. The tracking efficiency and transverse momentum resolution for low momentum particles were also further optimised. Additionally, the readout rate was increased for pp and Pb–Pb collisions [27, 28, 31, 30, 32].

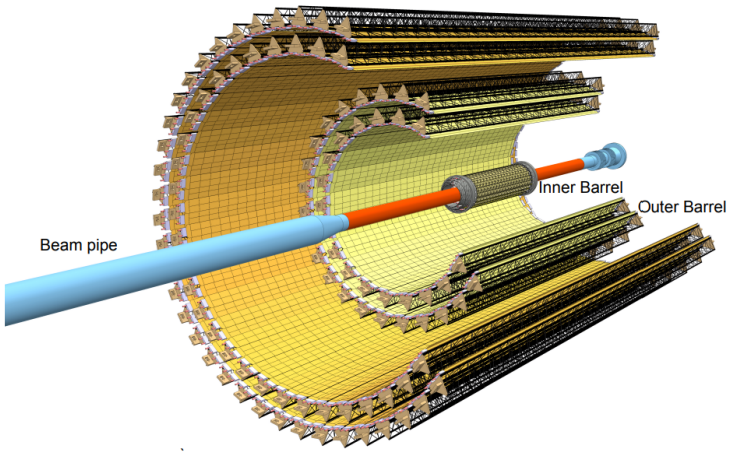

Figure 3.2: Layout of the Inner Tracking System 2 with the three layers in the Inner Barrel and four layers in the Outer Barrel consisting of silicon Monolithic Active Pixel Sensors (MAPS) [30]

Layer number	0	1	2	3	4	5	6
R_{min} [mm]	22.4	30.1	37.8	194.4	243.9	342.3	391.8
R_{max} [mm]	26.7	34.6	42.1	197.7	247.0	345.4	394.9

Table 3.1: ITS2 chip layer radii, numbers taken from [30, Table 1.1, p. 7]

3.3 The Time Projection Chamber

The Time Projection Chamber (TPC) can track and identify both low-momentum and high-momentum particles. It is the main detector in the central barrel of the ALICE detector. The TPC was upgraded to continuous readout during the Long Shutdown 2, as it could not otherwise handle an interaction rate of 50 kHz. The continuous readout could only be achieved with novel gas amplification, which was realised with Gas Electron Multiplier (GEM) foils [28, 34]. The layout of the TPC is shown in Figure 3.3. It has a cylindrical shape and starts from 0.85 m to 2.5 m. It is filled with a gas mixture $Ne - CO_2 - N_2$ (90/10/5) [28]. A central electrode splits the detector in two drift regions. The end plates are divided into 18 azimuthal sections containing Readout Chamber (ROC). When charged particles drift through the TPC, then they ionise the gas along the way. The electrons drift towards the Readout Chambers where the GEMs amplify the signal [28, 34, 33].

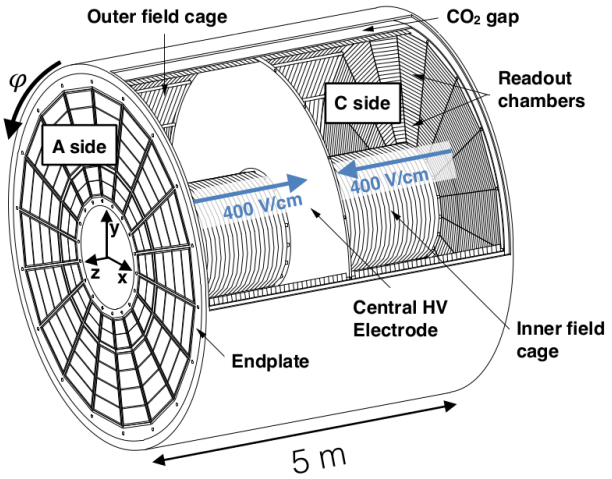

Figure 3.3: Layout of the Time Projection Chamber with labeling of the different parts [44]

The charged particles that travel through the gas of the TPC ionise electrons from atoms, losing energy in the process. The specific ionisation energy loss $\mathrm{d}E/\mathrm{d}x$ can be calculated using with the Bethe-Bloch equation [45, 46]:

$$\left\langle -\frac{\mathrm{d}E}{\mathrm{d}x} \right\rangle = K\rho z^2 \frac{Z}{A}\frac{1}{\beta^2}\left[\frac{1}{2}ln\left(\frac{2m_e c^2\beta^2\gamma^2 T_{max}}{I^2}\right) - \beta^2 - \frac{\delta\left(\beta\gamma\right)}{2}\right] \tag{3.1}$$

This function takes into account the density of the medium (ρ), the charge number of the medium (Z), the charge of the incident particle (z), the atomic mass of the medium (A), the velocity of the particle (β), the density correction (δ), the electron

mass (m_e), the speed of light (c), the Lorentz factor ($\gamma = \frac{1}{\sqrt{1-\beta^2}}$) and the mean excitation energy of medium (I) as well as the constant $K = 4\pi N_A r_e^2 m_e c^2 = 0.307$ MeVg^{-1}cm^2. The formula for calculating the maximum energy transfer in a single collision with an incident particle of mass M is:

$$T_{max} = \frac{2m_e c^2 \beta^2 \gamma^2}{1 + \frac{2\gamma m_e}{M} + (\frac{m_e}{M})^2} \tag{3.2}$$

With N_A representing the Avogadro's number and r_e as the classical electron radius. Different shapes of the Bethe-Bloch function are obtained for various particles. However, it is possible to divide the Bethe-Bloch function into three general regions. At low energies or momenta, the specific energy loss decreases sharply by a factor of $\frac{1}{\beta^2}$ to its lowest value. The minimum ionizing particles (MIPS) occur at $\beta\gamma \approx 3-4$. For larger $\beta\gamma$, the specific energy loss increases logarithmically with energy, which is known as the relativistic rise ($\sim ln(\beta^2\gamma^2)$). At higher energies, there is a plateau in dE/dx [45, 46, 47].

Particle identification (PID) can be performed by measuring momentum and energy loss of the particles. Figure 3.4 shows the specific energy loss of different particles measured with the TPC. By applying cuts to the dE/dx signal, only specific particles can be selected.

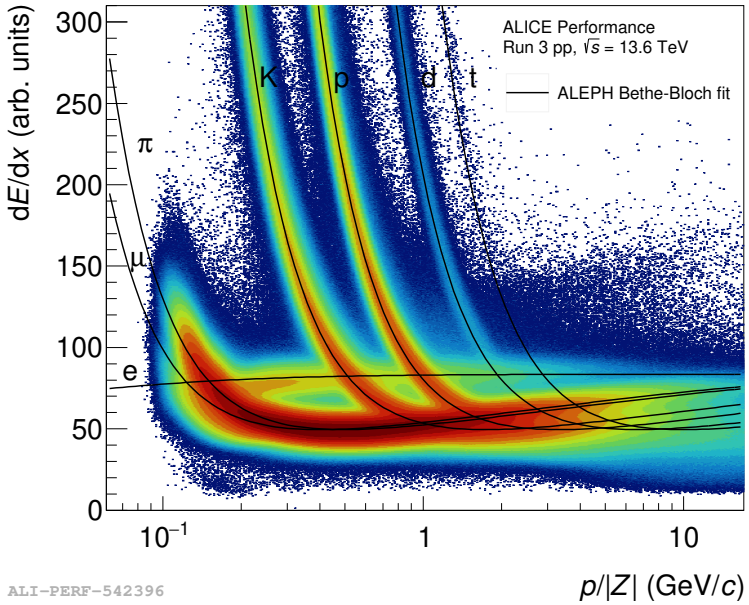

Figure 3.4: ALICE TPC dE/dx performance - Run3 pp 13.6 TeV - dE/dx signal as a function of $p/|z|$ with fitted ALEPH Bethe-Bloch parameterization to different particles dataset LHC22q apass3) [48].

3.4 Tracking and reconstruction of particles

Section 3.4.1 provides a general concept of tracking particles in detectors. Then, Section 3.4.2 explains the tracking of ITS2 standalone, TPC standalone and ITS-TPC together. In order to reconstruct the radiative decay of χ_c, it is essential to reconstruct photons. Section 3.4.3 describes the Photon conversion method used to detect photons in the ITS2 and TPC. Section 3.4.4 explains how the electron-positron pair from the photon is used for reconstruction, introducing the concept of reconstructing V0 particles.

3.4.1 General concept of particle tracking

In general, the concept of tracking typically incorporates 5 steps, as shown in Figure 3.5. However, the implementation of tracking may vary from experiment to experiment due to differences in the detectors and the algorithms used. The initial step, seeding, involves creating 'short tracks' that serve as the foundation for longer tracks. The next step is the expansion of the track seeds to more detector layers by the search for further hits. This procedure is known as track finding or pattern recognition. Thirdly, the track fitting process involves calculating the track parameters and covariance matrix based on the track points. Next, bad-quality or fake tracks are removed through quality cuts during the track selection process. For iterative tracking, steps 2-4 are repeated to remove allocated clusters and start again with clusters not in use. The beam collision point, i.e. the minimum distance point between the tracks, is identified in the final step, primary vertexing [49].

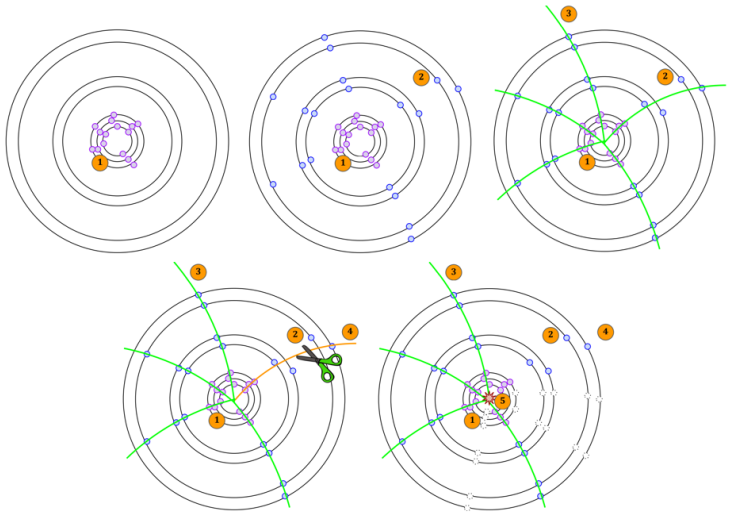

Figure 3.5: Five common steps of the basic concept of tracking: 1. Seeding, 2. Track finding/Pattern recognition, 3. Track fitting, 4. Track selection, 5. Primary vertexing [49]

3.4.2 Tracking in ALICE Run 3

ALICE Run 3 offers three different types of tracking are possible: ITS2 standalone tracking, TPC standalone tracking and ITS2-TPC tracks.

The process of standalone tracking in the ITS2 begins with the primary vertex seeding, which is divided into three partial steps. In the three innermost ITS2 layers, correlations among the hits are sought to form tracklets. Combinatorial matching and linear extrapolation are then applied to those tracklets, followed by unsupervised clustering to identify the collision point(s). The second stage of standalone ITS2 tracking involves track finding and fitting, which comprises also three sub-steps. The primary vertex position is used to reduce combinatorics in matching the hits. The track segments, also known as cells, are linked together to form a tree of potential track candidates called roads. This tracking technique is referred to as Cellular Automaton (CA) track seeding. The Kalman Filter (KF) is then employed to fit tracks from the candidate tracks. Quality criteria are used to identify and remove low-quality tracks A track quality criterion example is that an ITS2 track must have a minimum of 4 conservative hits in the ITS2 [49, 50, 51].

There are two main steps to the TPC standalone tracking process: tracking within a ϕ sector and track merging between sectors. The tracking within a ϕ sector consists of CA track seeding and an initial KF is applied to the track candidates within the sector. The second part of the TPC standalone tracking starts with the extension to segments in neighbouring sectors. Then additional clusters are acquired and a final KF fit is performed [49].

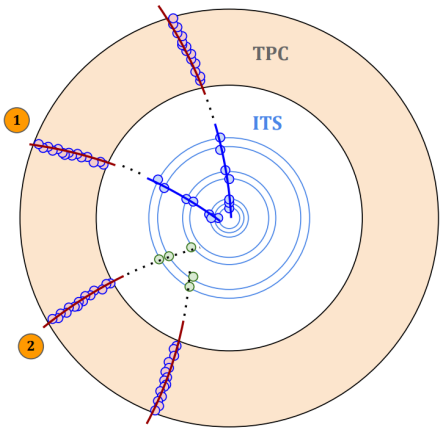

Figure 3.6: Schematic view of tracking in the ITS2 and TPC in ALICE Run 3 [49]

The ITS2-TPC tracks can be divided into two processes (Figure 2): Time-matching between ITS2 and TPC and Afterburner algorithm. Time-matching matches the ITS2 and TPC standalone. The Afterburner algorithm, on the other hand, takes the TPC

standalone tracks and the remaining ITS2 clusters and matches them. The Afterburner algorithm is used to improve the recovering efficiency for V0/cascade decay within the ITS2. This algorithm requires a minimum of 2 hits in the ITS2 for matching with TPC standalone tracks [49, 51].

3.4.3 Photon conversion method

Photons have to interact with the detector material in order to be able to detect them. Depending on their energy, photons interact differently with matter: Rayleigh scattering, Compton scattering (around 1 MeV), photoelectric effect (below 100 keV) and pair production (above 1.022 MeV) [45, 52]. Figure 3.7 shows the total photon cross section in lead versus photon energy.

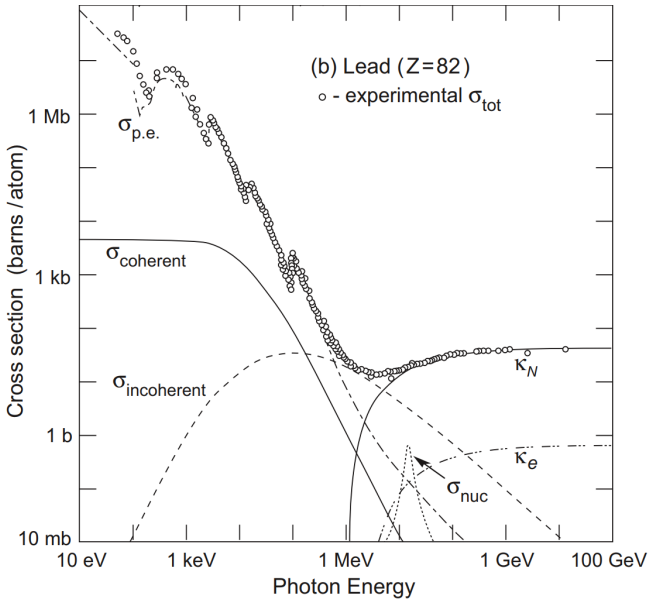

Figure 3.7: Total photon cross section in lead as a function of the photon energy. The different contributions are indicated by: $\sigma_{p.e.}$: photoelectric effect, $\sigma_{coherent}$: Rayleigh scattering at the whole electron shell, $\sigma_{incoherent}$: Compton scattering, σ_{nuc}: photoelectric effect with nucleus, κ_N: pair production in nuclear field, κ_e: pair production in electron field (asymptotic $\kappa_e \to \kappa_N/Z$) [45].

The ALICE detector measures above 100 MeV, where the pair production is the dominant effect. Pair production involves the conversion of a photon into an electron-positron pair. This method of measuring a photon through pair production is called Photon Conversion Method (PCM). Pair production can only happen in the presence of a nucleus, and the energy of the photon has to exceed the threshold energy, which is approximately the rest mass of the electron-positron pair: $E_\gamma \geq 2m_e c^2$. The Feynman diagram of pair conversion is drawn in Figure 3.8.

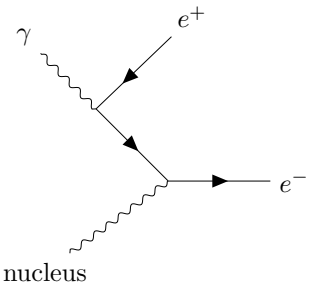

Figure 3.8: Feynman diagram of photon pair production

At high photon energies, the differential cross section for photons can be approximated for pair production:

$$\frac{d\sigma}{dx} = \frac{A}{x_0 N_A}\big(1 - \frac{4}{3}x(1-x)\big) \tag{3.3}$$

The differential cross section is dependent on the atomic number (A), the Avogadro constant N_A, the radiation length (X_0) and the fractional energy transfer (x). The radiation length, denoted by X_0, is defined as the average distance that higher energy electrons travel before losing all but 1/e of their energy through Bremsstrahlung. This distance is dependent on the material through which the electrons are travelling. The fractional energy transfer x is the ratio between the energy of the electron or positron and the photon energy ($x = \frac{E_{e^+e^-}}{E_\gamma}$). The differential cross section can be integrated to obtain the high-energy limit for photon pair production [45, 52]:

$$\sigma_p = \frac{7}{9}\big(\frac{A}{X_0 N_A}\big) \tag{3.4}$$

Depending on the position of the conversion point and on the photon energy the e^+e^-pair leaves signals in the ITS2 and TPC or only TPC. Sometimes, signals are also observed in outer detectors like TOF or TRD. The TPC, for example, measures the electron or positron by their energy loss in the gas mixture see Section 3.3. The signals from the electron or positron can be reconstructed into tracks, which together can be used to calculate the conversion point and other parameters such as the momentum in all three spatial directions of the original photon [53, 54]. The following section, Reconstruction of V0 particles (3.4.4), explains how the tracks are reconstructed to provide directional information for the photon.

3.4.4 Reconstructing V0 particles

V0 particles are subatomic particles that are heavy, unstable, and have no charge. They decay weakly into two daughter particles with opposite charges, creating a distinctive 'V'-shaped decay path. This shape is caused by the 0.5T magnetic field in the central barrel and the opposite electrical charge of the daughter particles. The particles are

named V0 due to their neutral charge and unique decay path. The most common V0 particles are Λ, $\overline{\Lambda}$, K_s^0 and γ. These particles are detected through their daughter particles because of their short lifetime and neutral charge, which prevents electromagnetic interaction with the detector material. Technically, photons γ cannot be classified as V0 particles since they convert into an electron-positron pair instead of decaying, and they are not massive. However, the procedure used to reconstruct V0 particles is also used for photon conversion.

Figure 3.9 shows the weak decay of a V0 particle into two daughter particles. The Distance of Closest Approach (DCA) is the smallest distance between the two daughter tracks. The figure also shows the location of the primary vertex which is the location where the pp collision happens [55, 56].

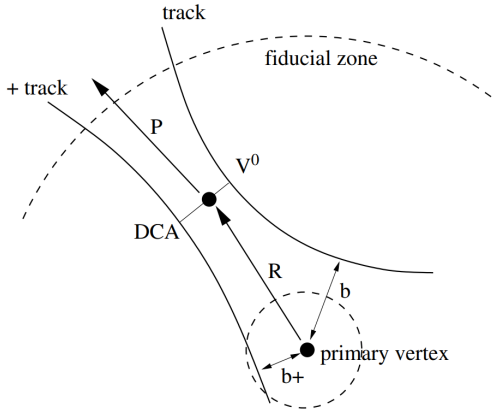

Figure 3.9: Geometry of V0 particle reconstruction from two daughter particles with oppisite charge [55]. DCA = Distance of Closest Approach, R = vector from primary vertex to the V0 vertex position.

The reconstruction process begins by selecting the seconday tracks. Only tracks with a sufficient impact parameter to the primary vertex are considered. Next, the two secondary tracks with opposite charges are combined, and various cuts are applied to the tracks. For instance, paired tracks are cut, if the DCA between the two tracks is greater than a specific value. After determining the vertex position, only secondary vertices within a specific fiducial area are retained. The size of the fiducial area depends on the expected particle density as well as the tracking precision, which in turn depends on the ITS2 detector layers. At the end of the V0 finding process, a cut is applied to the cosine of the pointing angle $cos(\theta_{PA})$ to verify the pointing direction of the V0 momentum is verified with respect to the primary vertex. The pointing angle θ_{PA} is defined as the angle between the V0 momentum (P arrow in Figure 3.9) and the vector (R) from the primary vertex to the V0 vertex position. The momentum of V0 can be calculated by using the track momenta of the two daughter particles at the DCA [55].

4. The Online-Offline computing system

The ALICE detector upgrades for Run 3 included implementing a continuous readout of the detectors, resulting in the generation of approximately 3.5 TB of raw data per second [27]. A new readout system was created to be able to handle this large amount of data: the Online-Offline (O^2) computing system [28, 57]. The O^2 computing system consists of the O^2 facilities (Figure 4.1) as well as the O^2 software framework. The Physics Data Processing (PDP) project is responsible for the development of the framework, software components and software infrastructure of the O^2 software framework [58]. The name Online-Offline (O^2) system comes from the synchronous online reconstruction of raw data and the asynchronous offline reconstruction [28, 57]. The physics analysis framework of the ALICE experiment was later separated from the O^2 framework and is now referred to as O^2Physics.

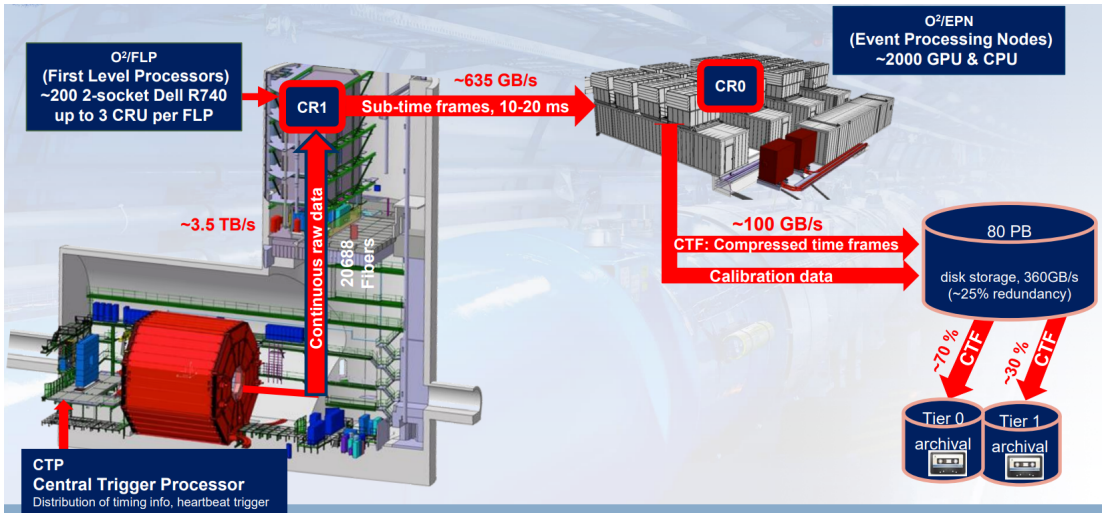

Figure 4.1: Data flow of the ALICE experiment during Run 3 [59].

In Section 4.1 the process from raw data to calibrated and compressed Analysis Object Data (AO2D) files and the associated facilities are described. This is followed by a brief summary of the O^2 software and the framework used to analyse the data (see Section 4.2). Next, the workflow of an analysis task in the O^2Physics framework and the general structure of an analysis task are explained in Section 4.3. Section 4.4 provides a detailed description of the Dileptons-Quarkonia (DQ) analysis framework, as the analysis task developed during this work is an extension of it. Specifically, the task combines the existing dilepton analysis with reconstructed photons by the Electromagnetic Probes (EM) analysis framework (Section 4.5) to identify triple candidates γe^+e^- from the

radiative decay of the χ_c meson. Within the DQ framework ALICE Run 3 data are analyzed using the tableReader.cxx file with different analysis tasks (Section 4.4.1). The dqEfficiency.cxx contains the analysis tasks for analysing Monte Carlo simulations (Section 4.4.2). Both files are linked to other files in the DQ analysis framework. Section 4.4.3 discusses the necessary files and their role in the developed analysis task.

4.1 Data flow in the O^2 computing system and facilities

In order to process the measured 3.5TB/s of data in Run 3 of the ALICE experiment, a new data flow had to be established. The data flow within the O^2 software framework of the ALICE experiment, encompassing the associated facilities is displayed in Figure 4.1. The data flow with the calibration and reconstruction of the data can be sectioned into five steps (Figure 4.2).

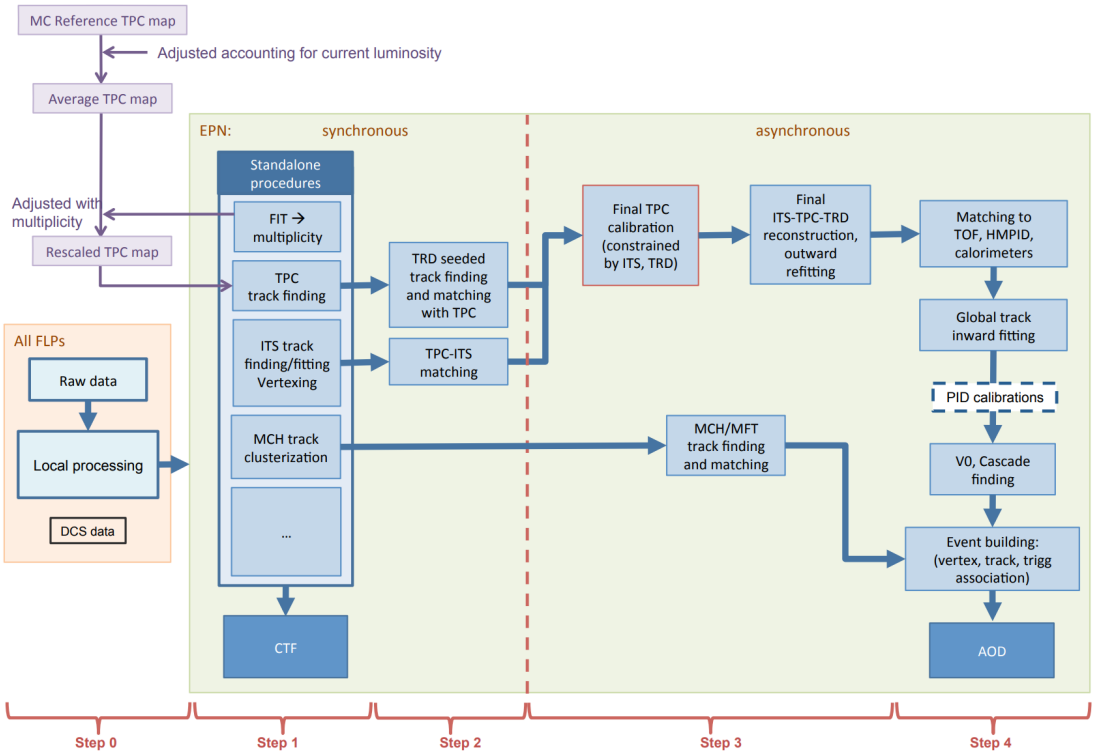

Figure 4.2: Schematic outline of the reconstruction and calibration data flow [57]

In Step 0, all raw data from the readout electronics is sent to the Counting Room 1 (CR1). This is where the First Level Processor (FLP) are located, which read the raw data and split it up into Sub-Time Frames. The Sub-Time Frames are calibrated and a local partial reconstruction is performed as well as compressing the data by zero suppression. The FLPs also include the data quality control (QC) system. In Step 1, the compressed Sub-Time Frames, approximately 635 GB/s, are forwarded to the

Counting Room 0 (CR0). There, the Event Processing Nodes (EPN) carry out an online reconstruction in real-time, which involves standalone track finding for the ITS2 and TPC detectors, as well as a final reduction of the data. The algorithm used for the data compression are based on the reconstructed steps. In Step 2, the ITS2 and TPC data is matched and the TPC tracks are used as seeds to find the tracks in the TRD detector. After the finished synchronous processing the data is stored in Compressed Time Frames (CTF) and sent to a remote storage location along with the calibration data. There, it can be accessed for asynchronous processing. In Step 3, the compressed TPC data gets a final calibration to achieve the final quality level. Also the tracks are outward reconstructed through all three detectors ITS2, TPC and TRD based on the updated calibration. In the last step, the reconstructed tracks are matched with TOF, HMPID and calorimeters. Additionally, another inward tracking is done as well as PID, V0 finding and event extraction. The processed data is then stored in AO2D and the CTF are deleted to get free disk space [57, 59, 60, 49, 61].

The technical design report of the created Online-Offline (O^2) computing system with more information can be found [57].

4.2 The ALICE O^2 software and analysis framework

As already mentioned in the beginning of the chapter, the ALICE O^2 software framework was split in 2021 into O^2 [62] and O^2Physics [63]. Both frameworks work with AO2D files consisting of arrow data tables (`https://arrow.apache.org/`) because they allow for high processing speed. Further information on the functioning of these data tables can be found in Ref. [64].

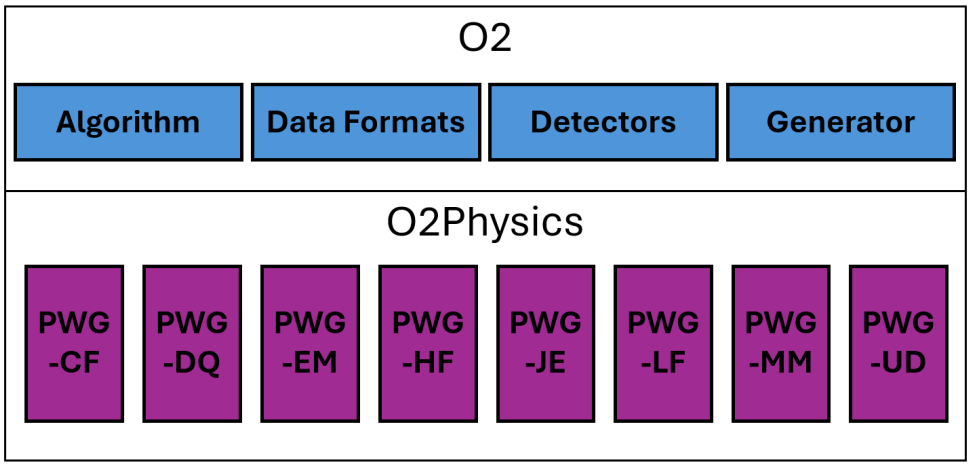

Figure 4.3: The layout of O^2 and O^2Physics software

In Figure 4.3 the main parts of the O^2 and the O^2Physics software are shown. The O^2 software has four main parts: Algorithm, Data Formats, Detectors and Generators. The O2Physics analysis framework is divided into eight Physics Working Group (PWG)s, each of which specializes in analyzing different physics topics. The abbreviation of the different PWG stands for: Correlations and fluctuations (CF), Dileptons-Quarkonia (DQ), Electromagnetic Probes (EM), Heavy flavour (HF), Jets (JE), Light-flavour (LF), Monte carlo and minimum-bias (MM) and Ultra-peripheral collisions and diffraction (UD) [65].

Each PWG directory has the following structure: Core, DataModel, TableProducer and Tasks. The Core folder has all the files with the common code, for example, the cuts for the tables, a library to define the histograms and signals, as well as, a file which manages the variables. In DataModel the derived data tables are defined through namespaces. The TableProducer contains the tasks which create the tables which are specified in DataModel. The Tasks folder has the files with the analysis tasks created for each physics analysis. Analysis tasks utilise the tables created and have the ability to edit and create new tables. The resulting data can also be used to populate histograms [66]. How such an analysis task is structured and which features it has, is described in the next section.

The documentation of the ALICE O^2Physics analysis framework can be found in Ref. [65].

4.3 Workflow and Analysis Tasks in O^2Physics

The O^2Physics analysis framework is organized in modular, flexible and interconnected analysis tasks. These tasks are C++ structures and are managed in workflows. A workflow consists of one or multiple tasks with specified input and output as well as a set of configurations. The workflow starts with data tables consisting of tracks and collisions which are saved in the AO2D files. Then the analysis tasks in the workflow are executed. The tasks reads tables from the input and depending on the task it edits the table or creates a new table. The new or edited table can be used as input for another task (transient output). At the end of most workflows analysis objects like histograms with the analysed data are created (persistent output). The output produced is saved in an AnalysisResult.root file. To execute a workflow, the user has to select the corresponding O2 executables and specify the configurations. Multiple workflows can be executed by piping ("|") the O2 executables of each workflow together. This pipeline connects the output of one workflow to the input of the next workflow [64, 67, 68, 69, 70]. The O2 executables required for the developed analysis task are specified in Section 5.6.

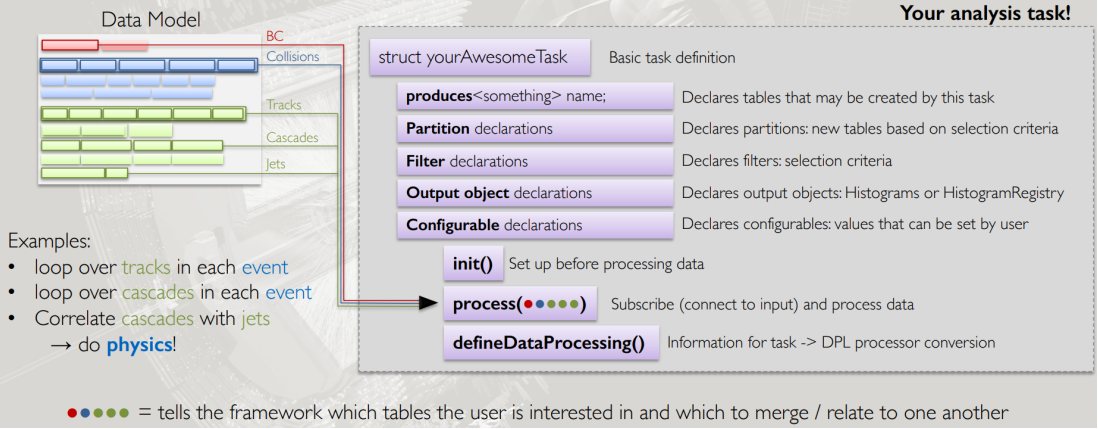

Figure 4.4: General analysis task structure [71]

All analysis tasks in the O^{2}Physics analysis framework follow the same file structure. This includes a specific structure in the C++ struct, as shown in Figure 4.4. The C++ struct requires some initial declarations: produces, Partition, Filter, Output object and Configurable. The tables produced in the task are defined by the produces statement. Partition creates additional tables based on the chosen options in the configuration file. The Filter enables the selection criteria from the input data, such as particles within a specific mass range. The output's structure, including the Histogram folders, is determined by the Output object. The Configurable object declares the variables that are used in the configuration file (json). Configuration variables may include the cut for the event tracks, the selected MCSignals, or the filter settings such as the lowest mass for the mass filter. All structures require an initialization function that is executed once at the start of the task. The process functions defines the input data tables, which can be any known data table. In the process function the input data gets analysed. Here, new code with functions and conditions for processing events are defined. It is possible to have several process functions in one struct. All structs typically have a processDummy() function that performs no action. This ensures that only the relevant structs are executed for the analysis task. In order to link the task with the analysis workflow, it has to be included in the defineDataProcessing() function. The location of defineDataProcessing() declaration depends on whether the file contains multiple task structures. It is either stated within the structure or after all task structures [64, 68, 71].

The analysis task file must meet additional requirements beyond those specified for a C++ analysis struct. The file should begin with the License agreement to confirm that the written code is free software. Following the License agreement, the header files are included. The header files that have to be included are at least "Framework/runDataProcessing.h" and "Framework/AnalysisTask.h" [70]. The remaining

header files are dependent on the created analysis task. To prevent name conflicts, it is necessary to add at least the namespaces o2 and o2::framework [68, 70].

4.4 The Dileptons-Quarkonia (DQ) analysis framework

The Dileptons-Quarkonia (DQ) analysis framework focuses the analysis on events with single leptons and dileptons especially electrons and muons. The table structure of the DQ Data Model is shown in Figure 4.5. The bold names in the boxes are the names of the corresponding table. The parameters stored in the tables are named in the other lines of the boxes. The red boxes are all tables which are specific for muons. The green tables are for electrons. The blue bubbles correspond to all events. The violet boxes are filtered dileptons tables.

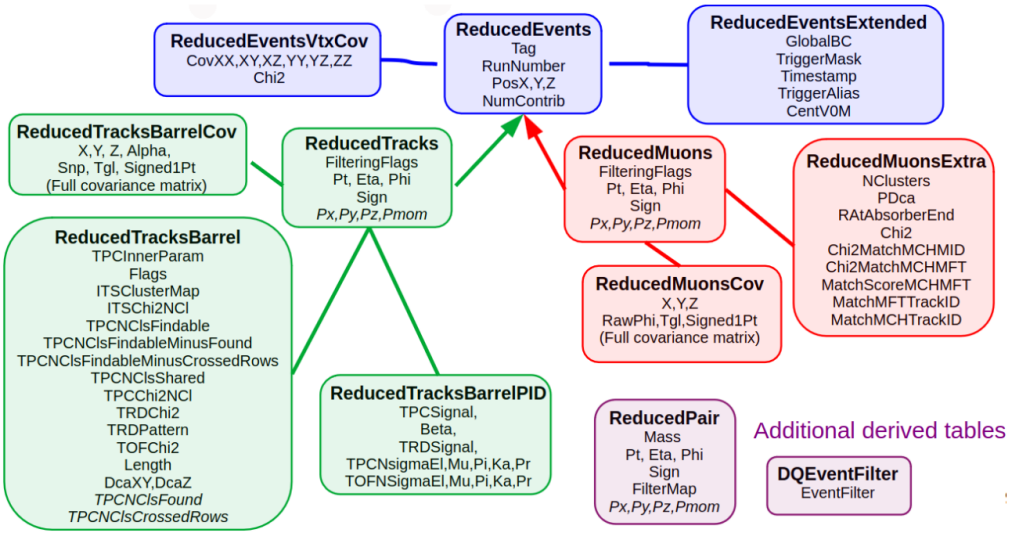

Figure 4.5: The O^{2}Physics DQ Data Model with all different tables [68]

Prior to analysing stored or simulated data (AO2D.root), it must undergo the skimming workflow (see Figure 4.6) to condense the data and retain only the necessary information for analysis. This data reduction enables a relatively small output. The skimming process uses common utilities of the O^{2}Physics framework such as event-selection, track-selection, event-timestamp, PID tasks as well as, functions of the DQ framework such as filter-pp, v0-selector or dalitz-selection. During the final stage of the skimming process, the TableMaker generates condensed data tables that include event and track details, as well as other relevant output. The skimmed workflow can be configured to create tables containing specific event and track information [68]. TableMakers are selected based on whether data from the ALICE detector or data from Monte Carlo (MC) simulations are skimmed. The TableMakerMC generates skimmed data tables

for both reconstructed particles and MC true particles based on the MCSignal class [72].

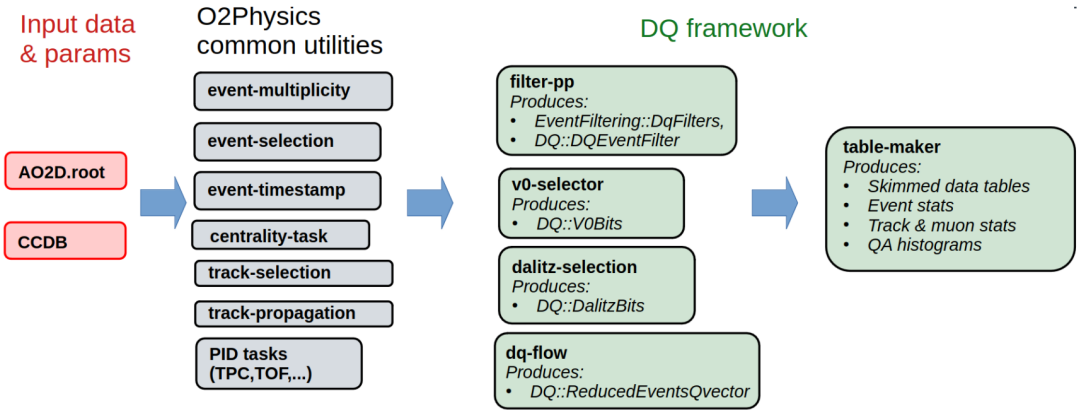

Figure 4.6: The skimming workflow of DQ analysis framework for data [68]. The skimming workflow for Monte Carlo is mostly the same. For instance, table-maker is replaced with table-maker-mc.

The workflows of interest for the created task are the tableReader.cxx and the dqEfficiency.cxx. The tableReader workflow analyses skimmed data tables from measured ALICE Run 3 detector data, while the dqEfficiency examines Monte Carlo Simulations. The two following subsections provide a more detailed description of both files. The Core folder contains crucial files for the task at hand which are outlined in Section 4.4.3.

4.4.1 DQ tableReader

The tableReader [73] performs seven analysis tasks: AnalysisEventSelection, AnalysisTrackSelection, AnalysisMuonSelection, AnalysisPrefilterSelection, AnalysisEventMixing, AnalysisSameEventPairing and AnalysisDileptonHadron. How the tasks in the TableReader interact with each other, as well as, the required input and the resulting output of the tasks are shown in Figure 4.7. All tasks except the AnalysisPrefilterSelection create histograms as output.

The AnalysisEventSelection chooses specific events in the input data tables, as the name implies. The AnalysisTrackSelection and AnalysisMuonSelection also perform selection, but on the tables for barrel tracks and muon tracks, respectively. The AnalysisTrackSelection can be further filtered using the AnalysisPrefilterSelection, which operates on reduced tracks. The resulting output is necessary for certain processes in the AnalysisSameEventPairing. The AnalysisEventMixing requires the cut event, track and muon tables as input, along with MixingHashes produced from the AnalysisEventSelection. The AnalysisEventMixing technique involves using particles from

different events to obtain the background for the analyzed decay in the SameEvent-Pairing. The AnalysisSameEventPairing has the most processing functions and can be used to analyse different decays with dileptons. For example, it can be used to analyse the decay of J/ψ, $\psi(2s)$ or the decay of ω, ρ and ϕ to low mass dileptons. The AnalysisSameEventPairing tasks generate various dilepton tables and analysis histograms. The AnalysisDileptonHadron task requires the dilepton tables as input. In this tasks, the dileptons are combined with tracks. This enables the analysis of decays such as $B \to J/\psi + K$ because the electron-positron pairs from J/ψs are considered as one of the decay products, rather than two separate particles [72, 73, 74].

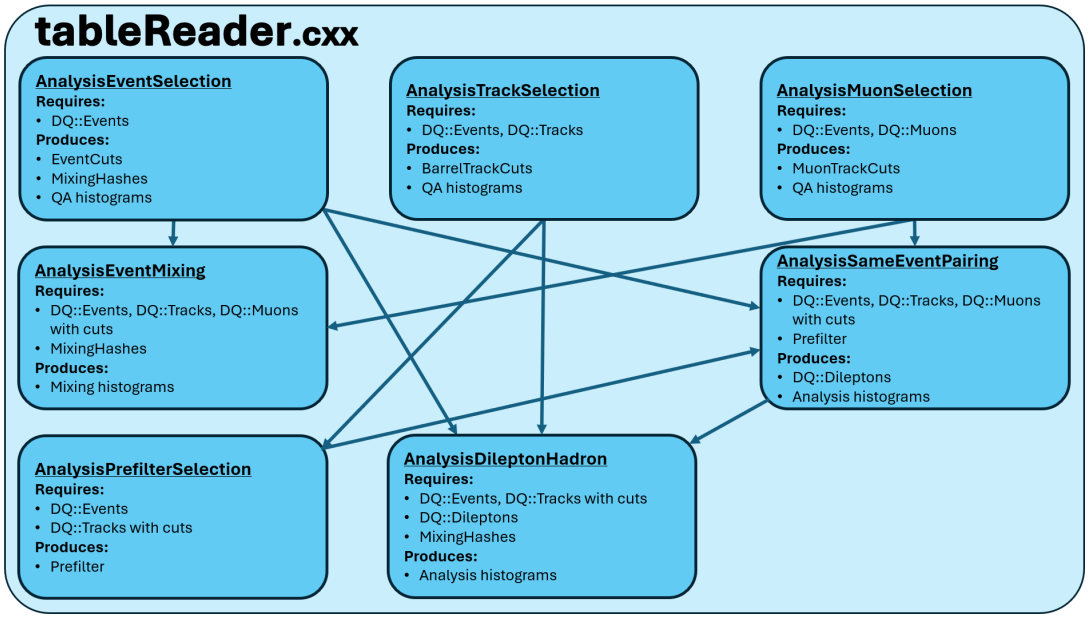

Figure 4.7: Schematic view of DQ tableReader structures and workflows for analysis of skimmed data using tableMaker data tables, based on [72, 73].

4.4.2 DQ dqEfficiency

The dqEfficiency [75] workflow (Figure 4.8) is used to analyse MC data tables. The file outlines a workflow that comprises of five tasks: AnalysisEventSelection, AnalysisTrackSelection, AnalysisMuonSelection, AnalysisSameEventPairing and AnalysisDileptonTrack. All tasks produce edited or new data tables and histograms based on the processed data tables. The AnalysisEventSelection, AnalysisTrackSelection and AnalysisMuonSelection are responsible for selecting events, barrel tracks and muon tracks, similar to the tableReader. The AnalysisSameEventPairing analyses the given event, track and muon tables for decays with dilepton pairs of opposite sign only which are then saved in several dilepton tables and analysing histograms. The Analysis-

DileptonTrack[1] utilises the dilepton tables to analyse particle decays to dimuon-muon ($B_c \rightarrow J/\psi + \mu \rightarrow \mu\mu\mu$) and dielectron-kaon ($B^+ \rightarrow J/\psi + \text{Kaon} \rightarrow e^+e^- + \text{Kaon}$). The function runMCGen is used by both structs AnalysisSameEventPairing and AnalysisDileptonTrack to generate MC true diagrams. It takes grouped Monte Carlo tracks as input and verifies them for MC true signals with one-prong or two-prongs [72, 74, 75].

The term 'one-prong' can refer to either single particle signals (such as χ_c, J/ψ, B, etc.) or to a decay product, like an electron from a J/ψ or a photon from π^0 decays. The term 'two-prongs' is used to describe two particle signals, like dielectrons or dimuons, or two decay products such as an electron-positron pair from J/ψ [75, 76].

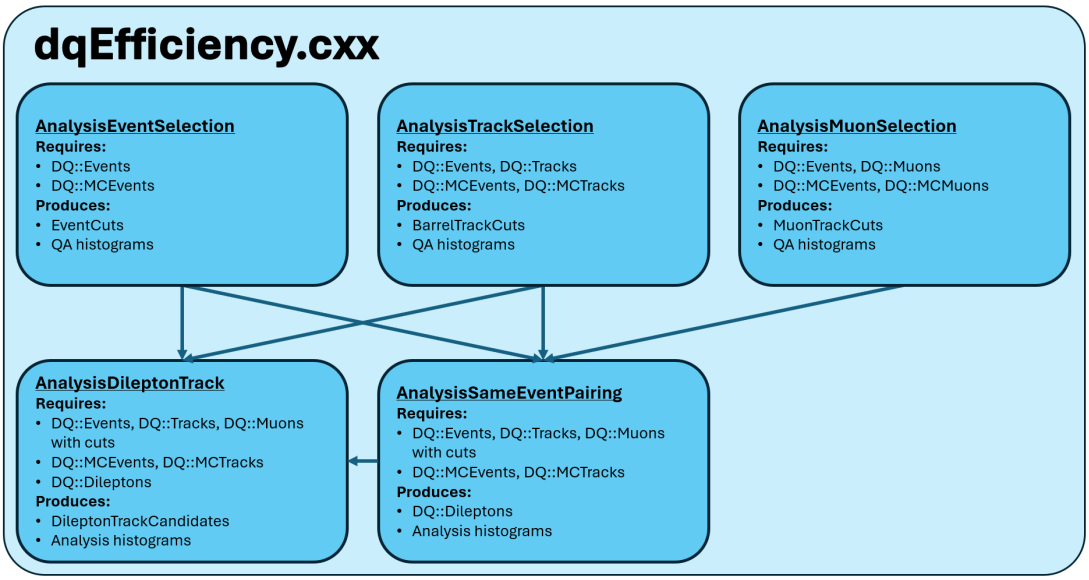

Figure 4.8: Schematic view of DQ dqEfficiency structures and workflows for analysis of skimmed MC using tableMakerMC data tables, based on [72, 75].

4.4.3 DQ files for tableReader and dqEfficiency workflow

To perform a data analysis in the DQ framework, multiple files are utilized beyond dqEfficiency and tableReader. Analysis tasks call functions and classes from other files in the Core, DataModel and TableProducer folders. In this part only the files important for the created tasks are mentioned to run an analysis.

The Core folder contains several important files, including CutsLibrary, HistogramLibrary, HistogramManager, MCProng, MCSignal, MCSignalLibrary and VarManager. The CutsLibrary defines potential cuts for the input data tables. Various types of cuts

[1]The AnalysisDileptonTrack is not completely implemented. Currently it can only determine MC reconstructed and MC reconstructed matched triple candidates and only one-prong MC generated true candidates

are defined, including those based on variables such as p_{T}, mass, opening angle, η as well as cuts based on TPC, ITS2 or TOF variables. After applying the cuts to the input data tables, they can be analysed using the tasks in dqEfficiency or tableReader [72, 74, 77].

After reconstructing events, tracks or pairs, the VarManager functions are used to populate the analysis variables. The analysis variables in the VarManager are used to fill the histograms [72, 74, 78]. The HistogramManager declares the functions to create and fill histograms [72, 74, 79, 80]. The HistogramLibrary defines the types of histograms available and their settings, including their variables [72, 81].

The MCProng, MCSignal and MCSignalLibrary are essential for analysing of Monte Carlo data. The MCProng class defines the particle PDG codes for PID and includes prong functions that specify the decay order of particles with their mother and daughter particles, as well as whether they originate from the primary vertex or not [72, 74, 82, 83].

The MCSignal class is responsible for transforming one prong or multiple prongs into a signal and includes the CheckSignal function to verify if MC particles meet the defined prongs of a requested signal. A signal can be defined in two orders: a mother particle to daughter particles or daughter particles from a mother particle. The CheckSignal function is crucial for obtaining MC reconstructed matched and MC generated true candidates. It checks whether the MC particles have the correct particle type (PDG number) and have the correct mother or daughter particles (PDG code and particle number). For instance, if the CheckSignal function is given three MC particles and the signal eePhotonFromChic1(2) (which is defined in the MCSignalLibrary.cxx as first particle e^+ or e^- from J/ψ from $\chi_{c1(2)}$, second particle e^+ or e^- from J/ψ from $\chi_{c1(2)}$ and third particle γ from $\chi_{c1(2)}$, see Section 5.5). The function verifies whether the first and second particles form an electron-positron pair by checking their PDG code. It also checks if the both particles have a common mother particle J/ψ with the same globalIndex and whether the J/ψ has a mother particle $\chi_{c1(2)}$. The third particle is tested to determine whether it is a photon (PDG code) and if it originates from a $\chi_{c1(2)}$ meson. The globalIndex of the χ_{c1} from the third particle (γ) is compared with the $\chi_{c1(2)}$ globalIndex of the first and second input particles (electron-positron pair) to confirm that all three particles originate from the same radiative decay of $\chi_{c1(2)}$ [72, 74, 84].

The MCSignalLibrary utilises prong functions and MCSignal functions to create a library that contains all MCSignals, such as the signal of an electron and a positron that originate from the same J/ψ [72, 74, 76].

4.5 The Electromagnetic Probes (EM) analysis framework

The Electromagnetic Probes (EM) analysis framework focus on reconstruction of photons and low mass dileptons which is why the code in the framework is split into Dilepton and PhotonMeson before it has the general structure Core, DataModel, Tasks and TableProducer as described in Section 4.2. The directory PhotonMeson is dedicated to the measurement of photons from neutral mesons like π^0 or η. For the developed analysis task only the photon part of PhotonMeson is important.

There are several asynchronous reconstruction workflows for reconstructing V0 candidates. This text will only cover the steps necessary to obtain the photon candidates table from PCM. However, it is also possible to obtain photons from PHOS and EMCal using other steps. The asynchronous reconstruction for V0 starts with the SVertexer which is a V0 finder. It identifies secondary tracks in the ITS-TPC tracks to reconstruct V0 particles. As of December 2023, a new SVertexer [85] was introduced, which additionally reconstruct photons using TPC only tracks. The new SVertexer was developed because the old SVertexer could only reconstruct photons up to a maximum radius of 30 cm. Further information on the new SVertexer can be found in reference [85]. Between the old and new SVertexer, the EM analysis framework had an extra V0 finder called 'createPCM' at the analysis level, which reconstructs photons from PCM. This V0 finder was used for material studies, as in the Bachelor Thesis [86]. The EM analysis framework utilises the V0 candidates table from the SVertexer. The Photon Conversion Builder then selects the photons to create a table of photon candidates from photon conversion [51, 87].

5. Description of the new χ_C analysis task

This chapter focuses on the new analysis task, AnalysisDileptonPhoton, which was created for the reconstruction of radiative χ_c decays from electron-positron pairs and photons within the O^2Physics analysis framework. Firstly, the goal of the analysis task is specified in Section 5.1. A general outline of the analysis task is provided in Section 5.2. Followed by a detailed description of AnalysisDileptonPhoton task inside the tableReader (Section 5.3) and dqEfficiency (Section 5.4). Section 5.5 outlines the added variables, functions and histograms necessary for the AnalysisDileptonPhoton struct in some of the Core folder files of the DQ analysis framework. Finally, Section 5.6 provides information on how to run the AnalysisDileptonPhoton task with Monte Carlo simulations and ALICE Run 3 data, specifying the required O2 executables.

5.1 The aim of the analysis task

The goal of the newly created analysis task in the DQ analysis framework is to be able to reconstruct the decay: $\chi_c \rightarrow \gamma + J/\psi \rightarrow \gamma e^+e^-$. This means that the task has to connect dilepton tables from DQ with photon candidate tables from EM. The task has to be designed to allow the analysis of data from ALICE Run 3 and Monte Carlo simulations. In order to be able to analyse not only radiative χ_c decays, but also other decays resulting in a dilepton pair and a photon ($\pi^0 \rightarrow \gamma e^+e^-$, $\eta \rightarrow \gamma e^+e^-$), a mass filter has to be added. This mass filter specifies the selected dilepton pair invariant mass. The initial task implementation is done using PCM photons, because the PCM photons have a good momentum resolution at low transverse momentum p_{T} and photons from χ_c decays have low p_{T} (see Section 7.1.1). A next step could be to do a similar task but using PHOS or EMCal photons.

5.2 Outline of the AnalysisDileptonPhoton task

The DQ analysis framework already investigates decays with dileptons. For instance, the $J/\psi \rightarrow e^+e^-$ or the $\psi(2S) \rightarrow e^+e^-$ decays are already implemented. However, the DQ currently lacks an analysis workflow involving photons that is needed for reconstruction of the χ_c. Therefore, the development of the new AnalysisDileptonPhoton task connecting photons from EM and dileptons from DQ was necessary in order to reconstruct the χ_c decay. Figure 5.1 shows the workflow of AnalysisDileptonPhoton. First, the AnalysisEventSelection and AnalysisTrackSelection apply the cuts specified

in the configuration file (see Appendix B) to the DQ event and track tables. Those cut tables are utilized in the AnalysisSameEventPairing task to generate the DQ dilepton tables (Green to purple boxes in Figure 5.1). The AnalysisDileptonPhoton task selects only the necessary electron-positron pairs from the dilepton tables. To get the photon candidates table the SVertexer (red box) finds in the asynchronous reconstruction the V0 candidates. In the EM analysis framework the Photon Conversion Builder (orange box) generates a photon candidates table by selecting the PCM photons among all V0 candidates from the V0 candidates table. The AnalysisDileptonPhoton takes this photon candidates table as input. Then the photons corresponding to the same event as the dileptons are identified, giving us triple candidates γe^+e^-. With Monte Carlo information, photons and dileptons cannot only be assigned to the same event, but also to the same decay, allowing the reconstruction of the decay $\chi_c \to \gamma + J/\psi \to \gamma e^+e^-$.

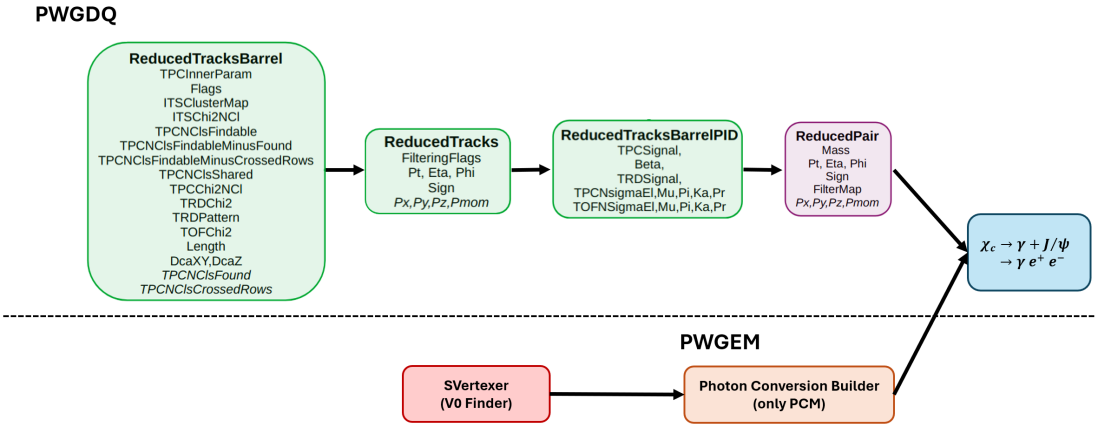

Figure 5.1: Workflow of the new AnalysisDileptonPhoton task using data tables from the DQ and EM analysis frameworks, based on [68]

The new AnalysisDileptonPhoton task for the reconstruction of the radiative χ_c decay was added as a new struct to both the tableReader and the dqEfficiency workflows. The radiative χ_c decay reconstruction was implemented as a struct in the existing files rather than in a separate file or as an additional process function in the AnalysisSameEventPairing task because the required dilepton tables are generated by the AnalysisSameEventPairing task and the connection to photons, although new, is not necessary for all analyses.[1]

The AnalysisDileptonPhoton task in the dqEfficiency for Monte Carlo simulations has additional features compared to the AnalysisDileptonPhoton task in the tableReader for ALICE Run 3 data. This additional features are due to the fact that the Monte Carlo information allows the reconstruction of MC generated true and MC reconstructed

[1]The created task bears some resemblance to the AnalysisDileptonHadron in the tableReader.cxx and the AnalysisDileptonTrack in the dqEfficiency.cxx. This similarity is evident in the selection of the dilepton pairs. That is why the new analysis task was designed with them in mind.

matched tracks. This is explained in more detail in Section 5.4.

The experts are currently reviewing the pull request for the AnalysisDileptonPhoton task. This repository `https://github.com/ikantak/O2Physics/tree/chic240205` contains the current version of the AnalysisDileptonPhoton task.

5.3 DQ tableReader with AnalysisDileptonPhoton task

This section describes all the changes made to the tableReader file to enable the reconstruction of the χ_c radiative decay in ALICE Run 3 data. The general modifications made to the tableReader file to allow the execution of the new AnalysisDileptonPhoton task are presented first, and then the subsequent focus is on the contents of the AnalysisDileptonPhoton task itself.

The EM photon candidate tables are added at the beginning of the file, which will be used later as input for the task. To execute the AnalysisDileptonPhoton task in the tableReader, it has to be added in the defineDataProcessing function to become part of the analysis workflow. To call the definitions from HistogramsLibrary.cxx for the new histograms in AnalysisDileptonPhoton task, they have to be specified in the DefineHistograms void at the end of the tableReader. For the AnalysisDileptonPhoton task, three histogram groups, DileptonPhotonInvMass, DileptonPhotonInvMass_cut and DileptonsSelected_cut, were added. The DileptonPhotonInvMass histogram group comprises histograms for the reconstructed triple candidates γe^+e^-. The DileptonsSelected histogram group has previously been defined and contains the definition of the histograms when plotting the reconstructed dileptons, in our case the electron-positron pairs e^+e^-. The histograms DileptonPhotonInvMass_cut and DileptonsSelected_cut are similiar to DileptonPhotonInvMass and DileptonsSelected, respectively. The only difference is that they are filled only when the triple candidates and the electron-positron pairs meet the rapidity and η cut criteria ($|y| < 0.9$ and $|\eta| < 0.9$) .

The tasks and workflows of the DQ tableReader are shown schematically in Figure 5.2. Additionally, it illustrates the connections between the new task AnalysisDileptonPhoton highlighted in green and the other tasks in the tableReader, as well as the input and output of the AnalysisDileptonPhoton. The AnalysisDileptonPhoton task requires dileptons table from the AnalysisSameEventPairing as input, as well as cut events table from the AnalysisEventSelection and cut tracks table from AnalysisTrackSelection. The new analysis task receives photon candidates table and EM event table as input from the EM analysis framework. The output of AnalysisDileptonPhoton task consists of analysis histograms.

The struct of the AnalysisDileptonPhoton task begins by defining the configuration

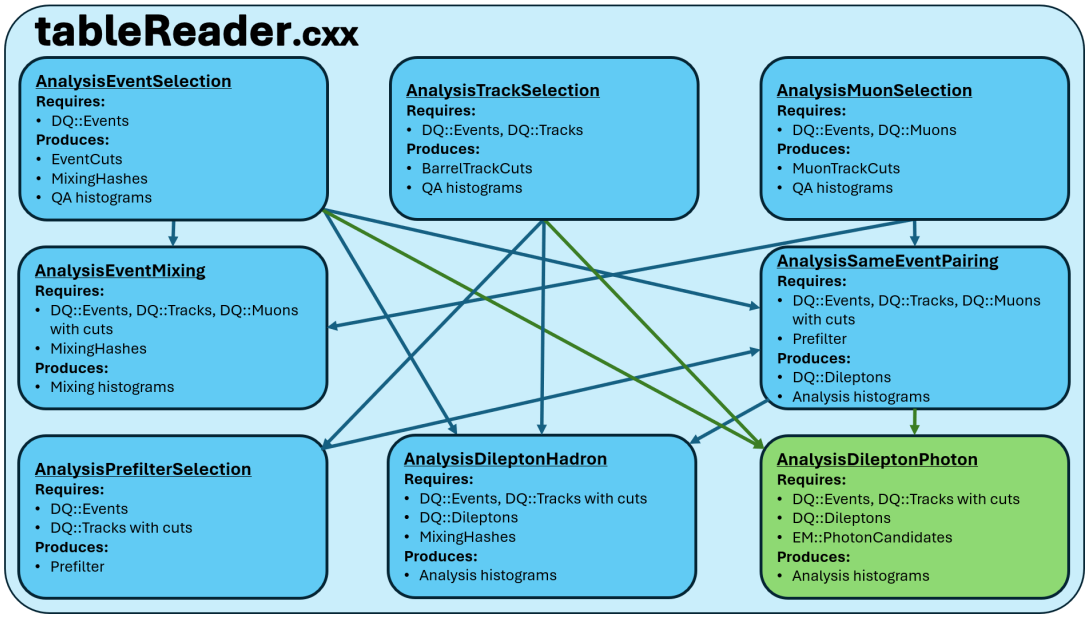

Figure 5.2: Schematic view of the DQ tableReader structures and workflows with new AnalysisDileptonPhoton task, based on [72, 73].

variables: cfgPhotonCuts, cfgDileptonLowMass, cfgDileptonHighMass and cfgDetectorCut. The cfgPhotonCuts enables the definition of a cut that is applied to the photon candidates table, such as nocut or qc. The mass range to select the dileptons is given by the cfgDileptonLowMass and cfgDileponHighMass. The cfgAcceptanceCut is a bool configurable which will create additional histograms with an rapidity cut $|y| < 0.9$ and η cut $|\eta| < 0.9$ if the configurable is set to true. The η cut is applied to both the electron and the positron, while the rapidity cut is applied to either the photon and triple candidate or the dilepton pair, depending on which histograms are being filled. The configuration file (see Appendix B) can be used to provide all necessary configurations when running the analysis workflow. If the configuration setting are not provided in the configuration file, the analysis task will use the default settings. The default setting for cfgPhotonCuts is nocut to keep as many photon candidates as possible. The mass range for the dileptons is set between 2.5 GeV/c^2 and 3.3 GeV/c^2. The cfgAcceptance cut is default true. After the configuration variables, the filters on events and dileptons are applied. Following this, variables for the analysis are defined.

Figure 5.3 displays the member functions within the AnalysisDileptonPhoton task, including their new features and connections to changed files in the DQ analysis framework. The initialization function creates all the analysis histograms without any input by calling the DefineHistograms function at the bottom of the tableReader, which in turn accesses the histogram definitions in the HistogramLibrary.cxx file.

The runDileptonPhoton function was created to reconstruct the triple candidates $\gamma e^+ e^-$

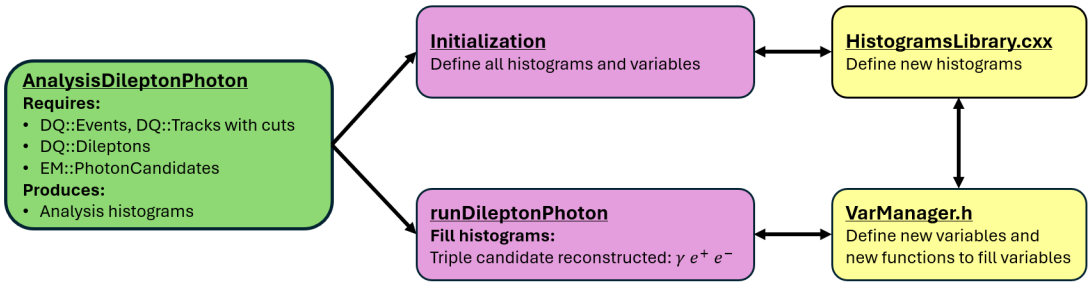

Figure 5.3: Schematic view of AnalysisDileptonPhoton task in the DQ tableReader with connections to changed DQ files

from χ_c radiative decay using the event, track, photon candidates and dilepton tables. The structure of reconstructing the triple candidates can be seen in Figure 5.4. Firstly, each reconstructed dilepton pair in an event is checked to determine if the two leptons have opposite charges, indicating that they can form an electron-positron pair[2]. The DileptonsSelected histograms containing only the dileptons without the photons are filled and the DileptonsSelected_cut histograms are filled if the cfgAcceptanceCut is true and they pass the rapidity and η cuts. Secondly, the photon candidates table is checked for a photon in that event. If the event has both an opposite sign dilepton pair and a photon in the event then a triple candidate was found. The triple candidates can be from the decay of the same mother particle or a random conbination. The triple candidate variable gets filled with the new FillDileptonPhoton function defined in the VarManager and the DileptonPhotonInvMass histograms get filled. Additionally, if the configurable cfgAcceptanceCut is set to true and the triple candidate particles fulfill the rapidity and η cuts they fill DileptonsSelected_cut and DileptonPhotonInvMass_cut histograms.

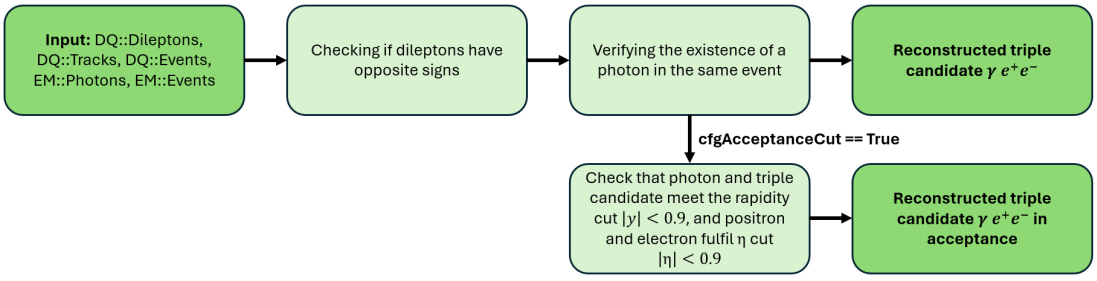

Figure 5.4: Reconstruction of triple candidates γe^+e^- in ALICE Run 3 data defined in the tableReader.cxx

The processSkimmed and processDummy process functions are located at the end of the AnalysisDileptonPhoton struct. The processSkimmed function calls the runDileptonPhoton for each event, while the processDummy function does not perform any

[2]This part is similar to the runDileptonHadron from the AnalysisDileptonHadron

action. If the AnalysisDileptonPhoton settings are not defined in the configuration file when the tableReader is run, the processDummy function is executed by default.

5.4 DQ dqEfficiency with AnalysisDileptonPhoton task

The AnalysisDileptonPhoton task in the dqEfficiency has additional components compared to the one in the tableReader due to the fact that the full Monte Carlo information is stored such as particle decay tree, MC momentum, products of particle interaction with the detector (electron-positron pair from Photon conversion) and many more. This information enables the reconstruction of the χ_c radiative decay as MC generated true and as MC reconstructed matched, rather than solely reconstructing it as in the tableReader. MC generated true means that all generated χ_c and all the decay products[3] are stored, independently whether the decay products are reconstructed or not. The reconstruction of MC generated true is useful for checking the χ_c generation was set properly, as well as the task works properly. The MC reconstructed matched means that each reconstructed track is matched to the corresponding MC track and it is checked for the particle ID and the mother particle. This Section explains the additional components of the AnalysisDileptonPhoton task.

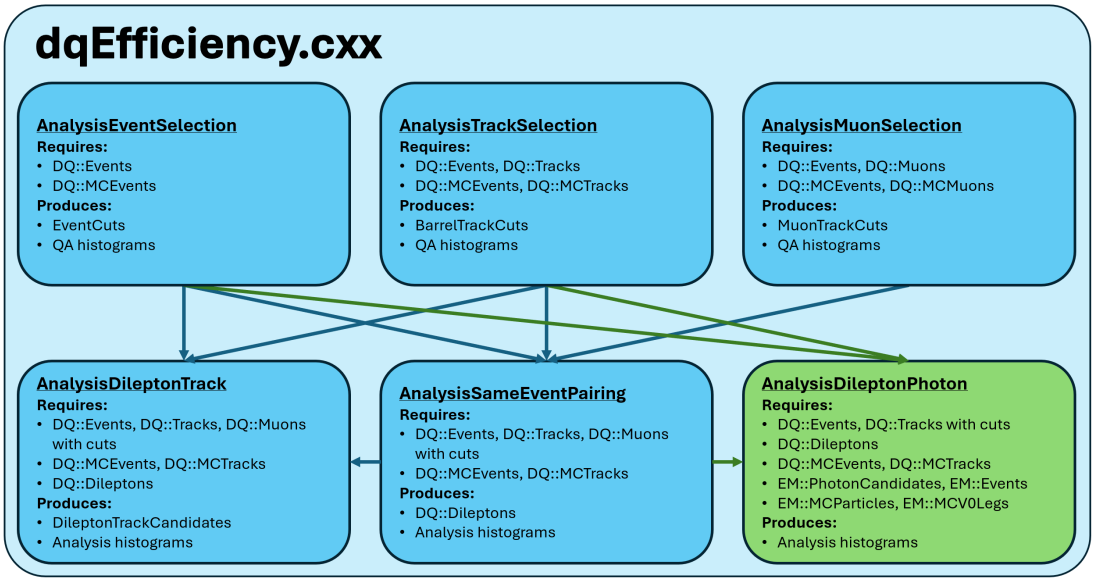

Figure 5.5: Schematic view of DQ dqEfficiency structures and workflows with new AnalysisDileptonPhoton task, based on [72, 75]

Figure 5.5 provides a schematic view of the structures and workflows in the dqEfficiency. The new AnalysisDileptonPhoton task and its connections to other tasks are highlighted in green. The input for the AnalysisDileptonPhoton in the dqEfficiency

[3] forced decay to $\gamma e^+ e^-$

differs a bit to the one in the tableReader. To perform the two additional reconstructions, the AnalysisDileptonPhoton in the dqEfficiency requires extra input information compared to the AnalysisDileptonPhoton in the tableReader. Specifically, it requires MC events, MC tracks, EM MC particles and EM MC V0legs tables in addditon to the DQ events, DQ tracks, DQ dileptons, EM photon candidates and EM events tables in the tableReader.

The photon candidates and the EM MC V0legs tables are added at the beginning of the dqEfficiency. The AnalysisDileptonPhoton is added into defineDataProcessing function for workflow of dqEfficiency as in the tableReader. The DefineHistograms function obtains the connection to the histograms for the MC generated true with acceptance cuts for one, two and three prongs, as well as for photon histograms with and without the acceptance cuts additionally to the added connections as in the tableReader.

The AnalysisDileptonPhoton struct in the dqEfficiency has the same four configurables as in the tableReader (cfgPhotonCuts, cfgDileptonLowMass, cfgDileptonHighMass and cfgAcceptanceCut), as well as two additional configurables (cfgBarrelMCGenSignal, cfgBarrelMCRecSignal) (see Appendix Figure B.7). These extra configurables are used to specify the created MC generated true histograms (cfgBarrelMCGenSignal) and to specify the MC reconstructed matched histograms (cfgBarrelMCRecSignal). The initialization function is similar to that in the tableReader, with the exception of the definition of additional and different histograms, as well as more variables.

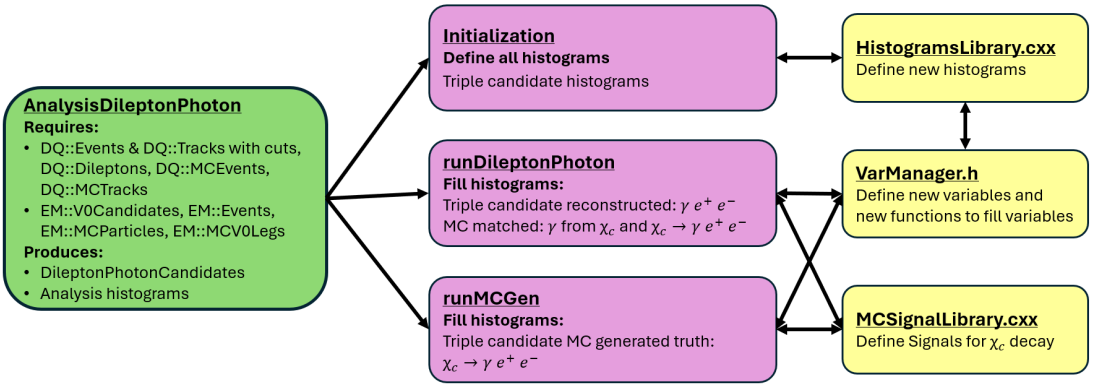

Figure 5.6: Schematic view of AnalysisDileptonPhoton in the DQ dqEfficiency with connections to DQ files with changes

After the initialization function, the AnalysisDileptonPhoton struct has not only a runDileptonPhoton function as in the tableReader but also the runMCGen function. Figure 5.6 shows the initialization function, the runDileptonPhoton and the runMCGen along with their new components as well as their connection to DQ Core files with changes. The runDileptonPhoton calculates the MC reconstructed and the MC reconstructed matched, whereas the runMCGen function computes the MC generated

true combinations. The CheckSignal function, already defined in the MCSignal.h file located in the DQ Core folder (see Section 4.4.3), is crucial for identifying MC generated true and MC reconstructed matched signals [84].

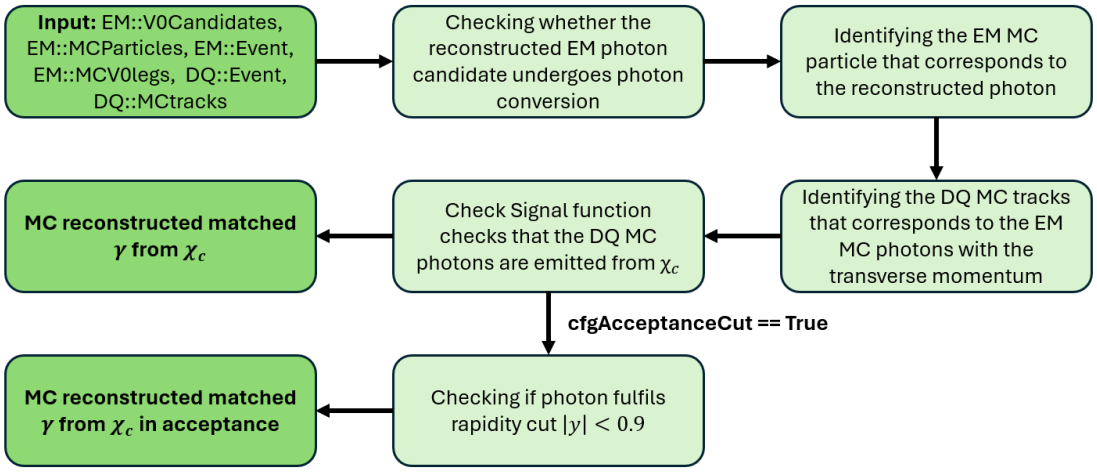

Figure 5.7: Reconstruction of MC matched γ from χ_c

The runDileptonPhoton and runMCGen are run through for each event. The runDileptonPhoton starts with finding the MC reconstructed matched photons from χ_c for an event which is illustrated in Figure 5.7. The EM photon candidates table is split into the photon candidates of the different EM events. Then only the photon candidates from the current event are taken by comparing the DQ event globalIndex with the collisionId of the photon candidate. Next, the photon candidate is checked to ensure that it has undergone photon conversion and is indeed a photon. For that the daughter particles consisting of a positive (e^+) and a negative track (e^-) are identified in the MC V0legs. Those are used to identify the corresponding MC daughters in the EM MC particles. The EM function FindCommonMotherFrom2Prongs takes the two MC daughters, all the EM MC particles and the PDG codes of the electron, positron and photon. It checks the MC daughters if they are an electron-positron pair and have a common mother in the EM MC particles which is a photon. The FindCommonMotherFrom2Prongs function returns the index of the MC photon in the EM MC particles if the condition was fulfilled. Otherwise, the returned index is negative, and the photon candidate is not a photon. The index is used to get the EM MC photon in the EM MC particles. In order to determine if the photon originated from a χ_c, it is necessary to identify the DQ MC track that corresponds to the EM MC photon. The EM MC particles have different indices than the DQ MC tracks. The challenges arising from the varying indices are outlined in Appendix D. Therefore, the photon is identified in the DQ MC tracks based on its transverse momentum, and the PDG code is checked to confirm that it is a photon. Next, the MC photon track is checked to have a mother particle with the method has_mother(). The CheckSignal function verifies then if the photon is from a χ_{c1} or

χ_{c2}. If the MC photon track passes the test then the reconstructed photon is added to the Selected_matchedMC_PhotonFromChic histograms. If the cfgAcceptanceCut configuration is set to true, the rapidity of the photon is tested to meet the cut $|y| < 0.9$. If the photon passes, then the Selected_cut_matchedMC_PhotonFromChic histograms are filled.

After the photons, the reconstructed dilepton pairs in an event are checked to see if the two leptons have opposite signs, as in the AnalysisDileptonPhoton task in the tableReader. The DileptonsSelected and DileptonsSelected_cut histograms are filled. The corresponding dilepton MC tracks are identified with the reducedMCtrack() method for the reconstructed dilepton pair. The CheckSignal function is then used to verify if the dileptons originate from the same J/ψ. If true, the DileptonsSelected_matchedMC histograms are filled with the reconstructed dilepton pair. With cfgAcceptanceCut set to true, both leptons must have $|\eta| < 0.9$ and the dilepton must have a rapidity of $|y| < 0.9$ in order to be added to the DileptonsSelected_cut_matchedMC histograms.

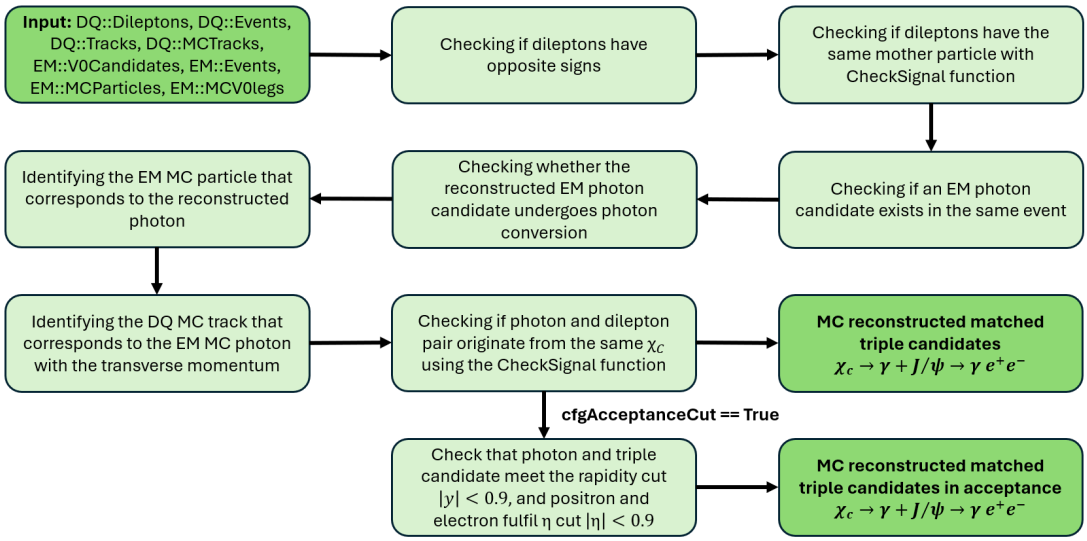

Figure 5.8: Reconstruction of MC matched triple candidates $\chi_c \rightarrow \gamma + J/\psi \rightarrow \gamma e^+e^-$

The next part in the runDileptonPhoton is the identification of the MC reconstructed matched triple candidates $\chi_c \rightarrow \gamma e^+e^-$. The reconstruction structure for them is shown in Figure 5.8. The initial two steps involving the dileptons have already been completed. Subsequently, the photon candidates are examined to determine if a photon is reconstructed in the same event as the reconstructed electron-positron pair. This is achieved by comparing the globalIndex of the DQ event with the collisionId of the photon candidates. If a photon candidate is found, then the first three steps of identifying the MC reconstructed matched photon from χ_c are performed. Once the DQ MC photon track is identified, the MC dilepton tracks and the MC photon track are verified using the

CheckSignal function to determine whether they originate from the same radiative χ_c decay. If the reconstructed electron-positron pair and reconstructed photon pass the check, they are considered a MC reconstructed matched triple candidate $\chi_c \to \gamma e^+ e^-$ and the DileptonPhotonInvMass_matchedMC histograms are filled. If cfgAcceptanceCut is set to true, the DileptonPhotonInvMass_cut_matchedMC histograms are filled if the MC reconstructed matched triple candidate particles pass all the cuts.

At the end of the runDileptonPhoton, the reconstructed triple candidates $\gamma e^+ e^-$ as in the tableReader are reconstructed (see Figure 5.4).

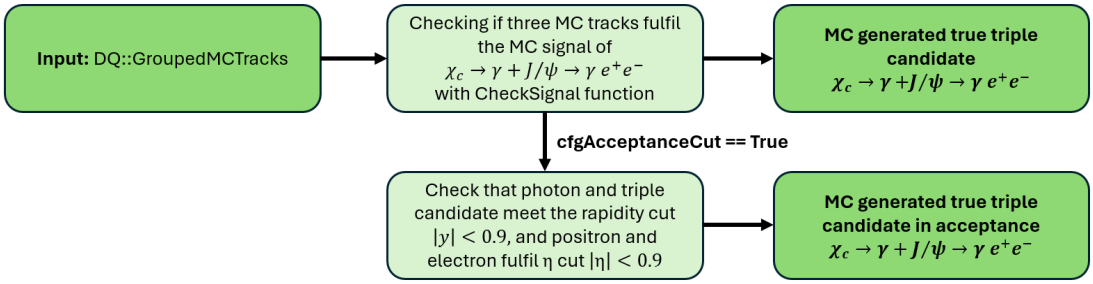

Figure 5.9: Reconstruction of MC generated true triple candidates $\chi_c \to \gamma + J/\psi \to \gamma e^+ e^-$

The runMCGen function generated the Monte Carlo true histograms, providing all events in the Monte Carlo simulation. It requires groupedMCTracks as input, which are the MC tracks grouped into events. The AnalysisDileptonTrack uses runMCGen for one-prong signals, while the AnalysisSameEventPairing uses it for one-prong and two-prong signals. However, the radiative decay of χ_c into an electron-positron pair and a photon produces a three-prong signal. Therefore, the runMCGen function from the AnalysisSameEventPairing can be used and complemented with a three-prong case. In the one-prong and two-prong cases, the acceptance cut must be added. For one-prong signals, if cfgAcceptanceCut configurable is selected to true, the particles are verified that they have an absolute value of rapidity less than 0.9. For MC generated true two-prong, for example $e^+e^-$from J/ψ, the electron and positron are checked for an absolute value of η smaller than 0.9 and that the pair has $|y| < 0.9$. If these conditions are met, the MCTruthGen_cut and MCTruthGenPair_cut histograms will be populated. The 3-prong case in the runMCGen function works similarly to the two-prong case, but with three particles. Figure 5.9 displays the steps for reconstructing MC generated true triple candidates $\chi_c \to \gamma e^+ e^-$. The CheckSignal function controls that three particles meet specific criteria. Specifically, it checks that they are constituted by an electron, a positron and a photon, and that the electron and positron originate from the same J/ψ. Additionally, the photon and J/ψ are checked if they result from the decay of the same radiative χ_c decay. If the CheckSignal function returns true, the MCTruthGenTriple

histograms get filled. When cfgAcceptanceCut is set to true, the MC tracks are tested to ensure they pass the rapidity and η cuts. The MCTruthGenTriple_cut histograms are populated only when these cuts are passed.

The AnalysisDileptonPhoton struct has like in the tableReader two process functions: processDielectronPhotonSkimmed and processDummy (see Appendix B). The processDielectronPhotonSkimmed function not only runs the runDileptonPhoton function for each event but additionally executes the runMCGen function with grouped MC tracks for each event.

5.5 Additional changes in DQ connected with AnalysisDileptonPhoton task

The VarManager.h, MC SignalLibrary.cxx, HistogramsLibrary.cxx, and CutsLibrary.cxx have been updated with the required variables, functions, and histograms to execute the AnalysisDileptonPhoton tasks in tableReader.cxx and dqEfficiency.cxx. This section outlines these updates.

VarManager.h
The VarManager was updated to include new variables and functions to accommodate the changes in the tableReader and dqEfficiency. The PairCandidateType variable group now includes the new decay variable kTripleCandidateToEEPhoton for decays into triple candidates consisting of a photon and an electron-positron pair. The PairCandidateType variables serve as conditions in certain VarManager funtions to accurately calculate the parameters for decays. For instance, when using the mass of the particle from the O2 tables. When executing the AnalysisDileptonPhoton task, the PairCandidateType variable is set within <> brackets in the call of the runDileptonPhoton function by the process function of the AnalysisDileptonPhoton. Furthermore, the variables kDeltaMass and kDeltaMass_jpsi were declared, which are necessary for the Δm (see Equation 6.5) and $\Delta m + m_{J/\psi}^{\mathrm{PDG}}$ (see Equation 6.6) histograms. Table 5.1 presents the key variables and their meanings for the AnalysisDileptonPhoton analysis task.

To calculate the triple candidates in the runDileptonPhoton in the tableReader, it was necessary to create the function FillDileptonPhoton. This function takes the electron-positron pair and a photon, as input and optionally a variable to save the output parameters are saved as input. If the optional variable is not given then the output parameters are saved in fgValues of the VarManager. The FillDileptonPhoton function calculates the parameters of the triple candidates, which are the mass, transverse momentum, η, rapidity, Δm and $\Delta m + m_{J/\psi}^{\mathrm{PDG}}$ as well as saves the mass, transverse

momentum and η values of the dilepton and the photon.

Variable name	**Definition**	
kPairMass	mass of triple candidates	$m_{\gamma e^+e^-}$
kPairMassDau	mass of dileptons	$m_{e^+e^-}$
kMassDau	mass of reconstructed photons	m_γ
kPairPt	transverse momentum of triple candidates	$p_{\mathrm{T},\gamma e^+e^-}$
kPairPtDau	transverse momentum of dileptons	p_{T,e^+e^-}
kPt	transverse momentum of photons	$p_{\mathrm{T},\gamma}$
kPt1	transverse momentum of lepton 1	$p_{\mathrm{T,\ lepton\ 1}}$
kPt2	transverse momentum of lepton 2	$p_{\mathrm{T,\ lepton\ 2}}$
kPairEta	η of triple candidates	$\eta_{\gamma e^+e^-}$
kDeltaEta	η of dileptons	$\eta_{e^+e^-}$
kEta	η of photons	η_γ
kEta1	η of lepton 1	$\eta_{\mathrm{lepton\ 1}}$
kEta2	η of lepton 2	$\eta_{\mathrm{lepton\ 2}}$
kRap	Rapidity of triple candidates	$y_{\gamma e^+e^-}$
	Rapidity of dileptons	$y_{e^+e^-}$
	Rapidity of photons	y_γ
kDeltaMass	delta mass of triple candidates	Δm
kDeltaMass_jpsi	delta mass with added PDG mass of J/ψ	$\Delta m + m^{\mathrm{PDG}}_{J/\psi}$

Table 5.1: Variables used in VarManager.h

The VarManager for the AnalysisDileptonPhoton task in the dqEfficiency now includes three new functions: FillPhoton, FillTriple, and FillTripleMC. The FillPhoton function is utilized before filling the histograms photons from χ_c MC reconstructed matched. It gets all the variables from the reconstructed EM photon and saves the corresponding values in a given input variable to fill the histograms. The FillTriple function is called prior to the MC reconstructed matched triple candidates $\chi_c \to \gamma e^+e^-$ histograms. FillTriple takes as input the three particles of the triple candidates and an optional variable where the calculated parameters are saved. The function checks the PairCandidateType before calculating all the variables listed in the Table 5.1 (kRap as rapidity of triple candidates). The PairCandidateType is checked because FillTriple uses the masses of electrons and photons from the O2 tables. If other triple candidates consist-

ing of different particles are implemented in the future, the function can obtain their masses with a new condition. The FillTripleMC function is called during runMCGen to calculate the MC generated true triple candidates. Currently, FillTripleMC is identical to FillTriple, but in the future, additional parameters may be saved from the MC information. This is why two separate functions were created.

MCSignalLibrary.cxx

The MCSignalLibrary defines the signals of particles and decays. The χ_{c1} and χ_{c2} signals with their PDG code had to be declared. Additionally, the signal for the radiative decay of χ_{c1} and χ_{c2} to γe^+e^- had to be specified as well. In order to create histograms for various stages of the radiative decay, signals for J/ψ from χ_{c1} or χ_{c2}, electron and/or positron from J/ψ which originates from χ_{c1} or χ_{c2}, and photon from χ_{c1} or χ_{c2} were included. The MCSignalLibrary already contained the signal for the electron or/and positron from J/ψ implemented. Table 5.2 lists the PDG numbers for the different particles involved in the radiative decay of χ_c.

particle	χ_{c1}	χ_{c2}	J/ψ	γ	e^-	e^+
PDG number	20443	445	443	22	11	-11

Table 5.2: MC particle type PDG number defined in the MCProng.cxx file.

HistogramsLibrary.cxx

The HistogramsLibrary now includes new histograms for the triple candidates γe^+e^- in the case of the Monte Carlo true (mctruth_triple) and for the reconstructed or MC reconstructed matched events (dilepton-photon-mass). The histograms comprise one- and two-dimensional histograms of the mass, the transverse momentum p_{T} and η of e^+e^-, γ and γe^+e^- as well as Δm, $\Delta m + m^{\mathrm{PDG}}_{J/\psi}$ and rapidity y. Additionally, new histograms for photons were declared, consisting of p_{T}, η, m and rapidity y diagrams. The MC generated true histograms for one-prong (mctruth) and two-prong (mctruth_pair) got some additional diagrams or the range and the binning was increased. The histogram definitions are called using the DefineHistogram function at the end of the tableReader and the dqEfficiency.

CutsLibrary.cxx

One new event cut, eventStandardtest, was added to the CutsLibrary. This cut is set to exclude events that fall outside of -30 cm and 30 cm in the z-direction from the Vertex. The eventStandardtest was created to avoid cutting any events, ensuring that the EM photon candidates table and the DQ event table have the a common indexing (see the difficulties outlined in the Appendix D).

5.6 Executing the AnalysisDileptonPhoton task

To execute the AnalysisDileptonPhoton analysis task the input data, a configuration file and the O2 executables are required. The input data for the developed analysis task was already defined in Sections 5.3 and 5.4. The configuration file for running Monte Carlo simulations is based on the DQ configuration files configTableMakerMCRun3.json and configAnalysisMC.json. For running over ALICE Run 3 data, the configuration files configTableMakerDataRun3.json and configAnalysisData.json are needed. The configuration file for executing the AnalysisDileptonPhoton task contains not only the configurables for the reconstruction of the radiative decay of χ_c, but also the settings for the other O2 executables that are run beforehand. The configuration file used for the Monte Carlo Simulation analysis (see Chapter 7) was added to the Appendix B. Table 5.3 lists the required O2 executables for the AnalysisDileptonPhoton in both the dqEfficiency and in the tableReader. The O2 executables differ depending on whether dqEfficiency is run with Monte Carlo simulation or tableReader is executed with ALICE Run 3 data.

The o2-analysis-timestamp, o2-analysis-event-selection and o2-analysis-multiplicity-table provide corresponding to their name columns in the event tables. The o2-analysis-track-propagation adds columns to the track tables with $\mathrm{DCA}_{xy/z}$ and the tracks are propagated to primary vertices. The o2-analysis-tpc and o2-analysis-tof supplies TPC and TOF columns to the track tables [71]. The o2-analysis-tpc-full is important because it provides the electron identification [87]. The o2-analysis-dq-table-maker-mc and o2-analysis-dq-table-maker creates the tables corresponding with or without Monte Carlo information. The o2-analysis-em O2 executables are for the EM photon candidates tables. The o2-analysis-em-photon-conversion-builder and o2-analysis-em-skimmer-gamma-conversion reconstruct the photons from photon conversion. The o2-analysis-em-pcm-qc(-mc) creates analysis histograms from the photon conversion. The o2-analysis-dq-efficiency and o2-analysis-dq-table-reader are the O2 executables to run the dqEfficiency and tableReader, respectively.

O2 executable for χ_c	MC	Data
o2-analysis-timestamp	✓	✓
o2-analysis-event-selection	✓	✓
o2-analysis-multiplicity-table	✓	✓
o2-analysis-ft0-corrected-table		✓
o2-analysis-trackselection	✓	✓
o2-analysis-track-propagation	✓	✓
o2-analysis-tracks-extra-converter		✓
o2-analysis-pid-tof	✓	✓
o2-analysis-pid-tof-base	✓	✓
o2-analysis-pid-tof-full	✓	✓
o2-analysis-pid-tof-beta	✓	✓
o2-analysis-pid-tpc-base	✓	✓
o2-analysis-pid-tpc-full	✓	✓
o2-analysis-dq-table-maker-mc	✓	
o2-analysis-dq-table-maker		✓
o2-analysis-dq-efficiency	✓	
o2-analysis-dq-table-reader		✓
o2-analysis-em-pcm-qc-mc	✓	
o2-analysis-em-pcm-qc		✓
o2-analysis-em-create-emreduced-event	✓	✓
o2-analysis-em-photon-conversion-builder	✓	
o2-analysis-em-skimmer-gamma-conversion		✓
o2-analysis-em-associate-mc-info	✓	
o2-analysis-em-create-pcm		✓

Table 5.3: O2 executables for MC and Run 3 data; highlight colors of the O2 executable mean: yellow=general, orange=track, magenta=PID, cyan=DQ, lime=EM

6. Monte Carlo simulation

This chapter focuses on the Monte Carlo simulation created for this work. Firstly, Section 6.1 describes the parametrisation of the χ_c meson for the Monte Carlo simulation which employs the results of C. Rosenthal's Bachelor thesis [88]. Sections 6.2 and 6.3 analyse the specific production created with the given parametrisation.

6.1 Parametrisation of the χ_c mesons

The Monte Carlo simulation employs as parametrisation for the χ_c mesons the results of C. Rosenthal's Bachelor thesis [88], supervised by Priv. Doz. Dr. Yvonne Pachmayer. In chapter 4.1 of [88], C. Rosenthal parameterised the transverse momentum p_{T} distribution for χ_{c1} and χ_{c2} mesons using the p_T distribution of J/ψ [16] measured by ALICE and the cross section ratios $R = \frac{\sigma(\chi_c)}{\sigma(J/\psi)}$ [89] and $R_{12} = \frac{\sigma(\chi_{c2})}{\sigma(\chi_{c1})}$ [20] measured by LHCb. Only χ_{c1} and χ_{c2} were considered for the Monte Carlo simulation because χ_{c0} has only a branching ratio of $(1.40 \pm 0.05)\%$ [14].

The total cross section of χ_c with neglecting χ_{c0} and applying R_{12} is

$$\sigma(\chi_c) = \sigma(\chi_{c1}) + \sigma(\chi_{c2}) = \sigma(\chi_{c1}) + R_{12}\sigma(\chi_{c1}) \tag{6.1}$$

Next, the cross sections of χ_{c1} and χ_{c2} can be calculated from $\sigma(\chi_c)$ and R_{12}:

$$\sigma(\chi_{c1}) = \frac{1}{1+R_{12}} \cdot \sigma(\chi_c) \text{ and } \sigma(\chi_{c2}) = \frac{R_{12}}{1+R_{12}} \cdot \sigma(\chi_c) \tag{6.2}$$

Then, substituting the transverse momentum for the cross section for each χ_c results in

$$p_{\mathrm{T}}^{\chi_{c1}} = \frac{1}{1+R_{12}} \cdot p_{\mathrm{T}}^{\chi_c} \text{ and } p_{\mathrm{T}}^{\chi_{c2}} = \frac{R_{12}}{1+R_{12}} \cdot p_T^{\chi_c} \tag{6.3}$$

Thereafter, to get the transverse momentum of χ_{c1} and χ_{c2} independent from the p_{T}-distribution of χ_c the ratio $R = \frac{p_{\mathrm{T}}^{\chi_c}}{p_{\mathrm{T}}^{J/\psi}}$ is used. When the ratio is converted to $p_{\mathrm{T}}^{\chi_c}$ and inserted in $p_{\mathrm{T}}^{\chi_{c1}}$ and $p_{\mathrm{T}}^{\chi_{c2}}$ it gives:

$$p_{\mathrm{T}}^{\chi_{c1}} = \frac{R}{1+R_{12}} \cdot p_{\mathrm{T}}^{J/\psi} \text{ and } p_{\mathrm{T}}^{\chi_{c2}} = \frac{R}{1+\frac{1}{R_{12}}} \cdot p_{\mathrm{T}}^{J/\psi} \tag{6.4}$$

The used ratios $R = \frac{\sigma(\chi_c)}{\sigma(J/\psi)}$ and $R_{12} = \frac{\sigma(\chi_{c2})}{\sigma(\chi_{c1})}$ for the Monte Carlo simulations are shown in Figure 6.1a and 6.1b [88].

Both the p_{T} distributions of J/ψ and χ_c exhibit a strong dependence on the centre-of-mass energy $\sqrt{s}$, but they are quite similar to each other. To be able to use cross section

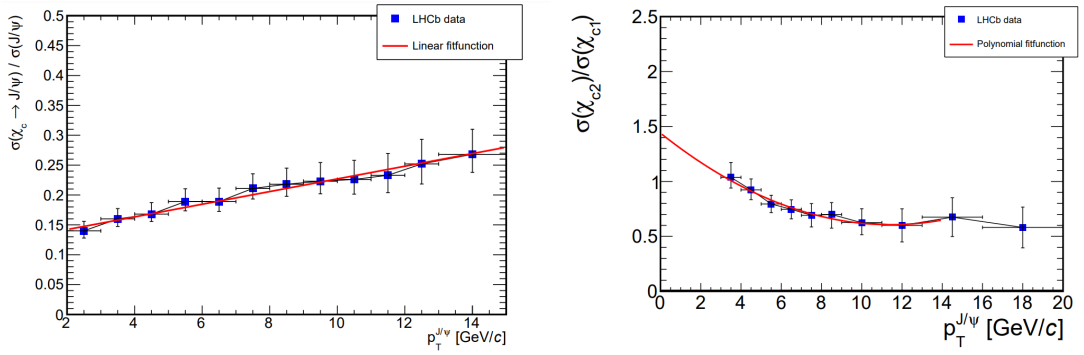

(a) **(b)**

Figure 6.1: **(a)** Ratio $R = \frac{\sigma(\chi_c \to J/\psi)}{\sigma(J/\psi)}$ depending on $p_{\mathrm{T}}^{J/\psi}$ in the range $2 < p_{\mathrm{T}}^{J/\psi} < 15\frac{GeV}{c}$ measured by the LHCb collaboration at $\sqrt{s}$= 7 TeV. A linear polynomial $R = 0.121 + 0.11 \cdot p_{\mathrm{T}}^{J/\psi}$ is fitted to the ratio. The data points have squared sum of statistical and systematic errors but without the polarization systematic error [88]. **(b)** Ratio $R_{12} = \frac{\sigma(\chi_{c2})}{\sigma(\chi_{c1})}$ depending on $p_{\mathrm{T}}^{J/\psi}$ in the range $4 < p_{\mathrm{T}}^{J/\psi} < 20\frac{GeV}{c}$ measured by the LHCb collaboration at $\sqrt{s}$= 7 TeV. A 2nd degree polynomial was fitted to the ratio: $R_{12} = 1.43953 - 0.145874 \cdot p_{\mathrm{T}}^{J/\psi} + 0.00638469 \cdot (p_{\mathrm{T}}^{J/\psi})^2$ [88].

ratios R and R_{12} from different centre-of-mass energies than the p_{T} distributions, their independence from the beam energy is assumed [88].

6.2 Monte Carlo simulation of χ_c mesons

The parameterisations described in the previous section were included into the following Cocktail generator GeneratorCocktailChiCToElectronEvtGen_pp13TeV.C. A Cocktail generator is necessary for creating Monte Carlo simulations. A pull request for the Cocktail generator was submitted and can be found at `https://github.com/AliceO2Group/O2DPG/pull/1430`. Once the pull request is approved, then the class for generating χ_{c1} and χ_{c2} with this parameterisation will be available to everyone. As the pull request is still open, local Monte Carlo simulations were conducted at GSI (Helmholtzzentrum für Schwerionenforschung GmbH). The created Monte Carlo simulations have 5 χ_{c1} and 5 χ_{c2} mesons per event which decay into $\gamma + J/\psi \to \gamma e^+ e^-$. Two hundred Monte Carlo simulations were generated, each with 10000 events, resulting in a total of 10^7 χ_{c1} and 10^7 χ_{c2} decays. The photons in the developed analysis task are detected via the Photon conversion method due to the low photon conversion probability (around 10% [53]) and due to the applied acceptance cut this large number of decays are required in order to obtain a significant number of detectable χ_c.

To compare MC generated true better with MC reconstructed and MC reconstructed matched, the rapidity ($|y| < 0.9$) and pseudorapidity ($|\eta| < 0.9$) cuts were set to the

Applied cuts	**min**	**max**
rapidity y	-0.9	0.9
pseudorapidity η	-0.9	0.9
Event vertex z	-30.0 cm	30.0 cm

Table 6.1: Acceptance cuts and event cut applied to all events and particles

same values as those of the ALICE detector in Run 3 (see Table 6.1). Therefore, Monte Carlo true only considers decays that occur within the detector's detectable area. These two cuts are the acceptance criteria for MC candidates in this analysis. The rapidity cut is applied to the photons, dileptons, triple candidates (γe^+e^-), and MC true one-prong candidates. One-prong candidates include χ_{c1}, χ_{c1}, J/ψ, electron or positron from J/ψ or χ_c and photon from χ_c. The pseudorapidity η cut is applied to the tracks of electrons and positrons. The rapidity and pseudorapidity cuts do not cut any candidates from the MC reconstructed and MC reconstructed matched.

candidates	**before cuts**	**after cuts**	%
J/ψ	20930970	18855580	90.08
χ_{c1}	10465480	9432710	90.13
χ_{c2}	10465480	9435415	90.16
$J/\psi \to e^+e^-$	20679630	8684527	42.00
$e^+e^-$from χ_{c1}	10392280	4415135	42.48
$e^+e^-$from χ_{c2}	10394020	4269392	41.08
γ from χ_{c1}	10465480	7173709	68.55
γ from χ_{c2}	10465480	7064071	67.50
$\chi_{c1} \to \gamma e^+e^-$	10387020	3226492	31.06
$\chi_{c2} \to \gamma e^+e^-$	10388860	3074983	29.60

Table 6.2: Effects of the rapadity cut $|y| < 0.9$ and pseudorapidity cut $|\eta| < 0.9$ on the number of reconstructable MC generated true candidates in column 2 and 3. The percentange of the candidates after cuts to before cuts are listed in column 4.

Table 6.2 shows the impact of rapidity and pseudorapidity cuts have on the MC generated true candidates. The numbers in the third column display the possible reconstructable MC generated true candidates. After the rapidity cut on the χ_c, only 90% of the forced decays are remain because χ_{c1} and χ_{c2} were generated with a rapidity setting of $|y| < 1$ in the Monte Carlo simulation. Less than half of the dielectrons from the χ_c are within the range of the ALICE detector during Run 3. Roughly two-thirds of the photons meet the rapidity cut, and the dielectrons resulting from photon conversion

must also fall within the range of the ALICE detector, which is true for two-thirds of the photons. Overall, less than one-third of the forced radiative decays of the χ_c in the Monte Carlo simulations fulfill the y and η cut resulting in only 6301475 possible reconstructable triple candidates compared to over 20 million decays. For all decay products in this MC simulation, more decay particle candidates from χ_{c1} lie in the acceptance cut than from χ_{c2}. The difference between reconstructable triple candidates of χ_{c1} and χ_{c2} is 151509 which means that χ_{c2} has 4.70% less reconstructable triple candidates than χ_{c1}.

Furthermore, the various O^{2}Physics analysis frameworks have their own skimming processes and reindex the events and tracks after selecting only those that are necessary for their analysis. To ensure that the tables from DQ and EM have matching indices, the event vertex cut in the z-direction was set to -30 cm and 30 cm (see Table 6.1). This criteria does not cut away any events, which makes it possible to connect the photons and dielectrons for the reconstruction of the χ_c.

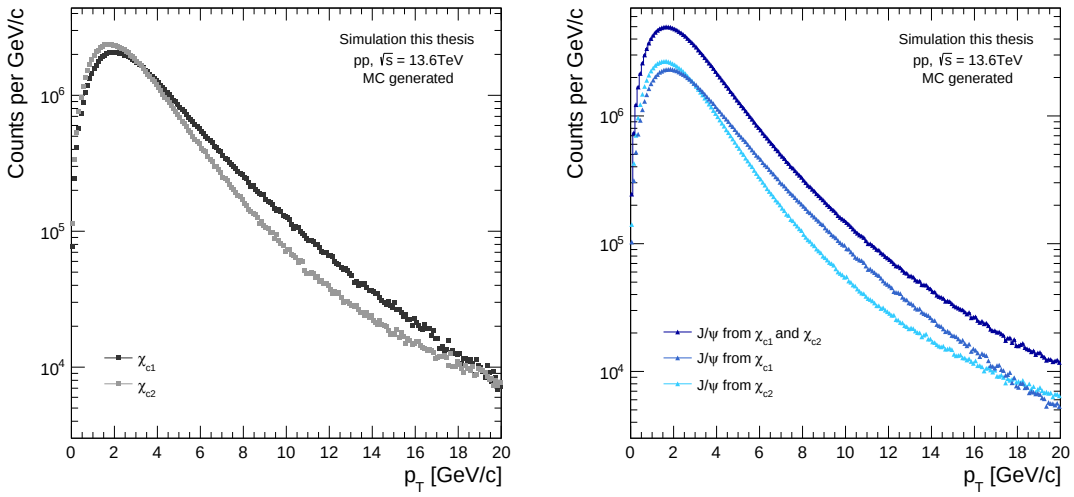

(a) **(b)**

Figure 6.2: **(a)** Transverse momentum p_{T} distribution of χ_{c1} and χ_{c2}; **(b)** Transverse momentum p_{T} distribution of J/ψ from χ_{c1} and/or χ_{c2}, as obtained from Monte Carlo simulation that employ the parameterisations described in C. Rosenthal Bachelor thesis [88].

The transverse momentum p_{T} distributions of χ_{c1} (in dark grey) and χ_{c2} (in grey) obtained from the Monte Carlo simulation with the acceptance cut are displayed in Figure 6.2a. Both distributions exhibit a broad maximum at approximately 1.75 GeV/c. The p_{T} distribution of χ_{c2} has a slightly higher maximum and a steeper slope after the maximum compared to χ_{c1}. Figure 6.2b shows the p_{T} distribution of J/ψ in the Monte Carlo simulations, which is comparable to the p_{T} distribution of χ_c. The blue p_{T}

distribution of J/ψ from χ_{c1} has a higher peak and a steeper negative slope than the light blue p_{T} distribution of J/ψ from χ_{c2}. However, the peak of J/ψ from χ_{c1} is not directly below that of J/ψ from χ_{c2}, but rather 0.2 GeV/c to the right at 1.85 GeV/c. The dark blue triangles is the p_{T} distribution of J/ψ from χ_{c1} and χ_{c2}. It peaks at 1.65 GeV/c, like J/ψ from χ_{c2} due to the higher peak. This behaviour of χ_{c1}, χ_{c2} and J/ψ is as expected based on the parameterisation.

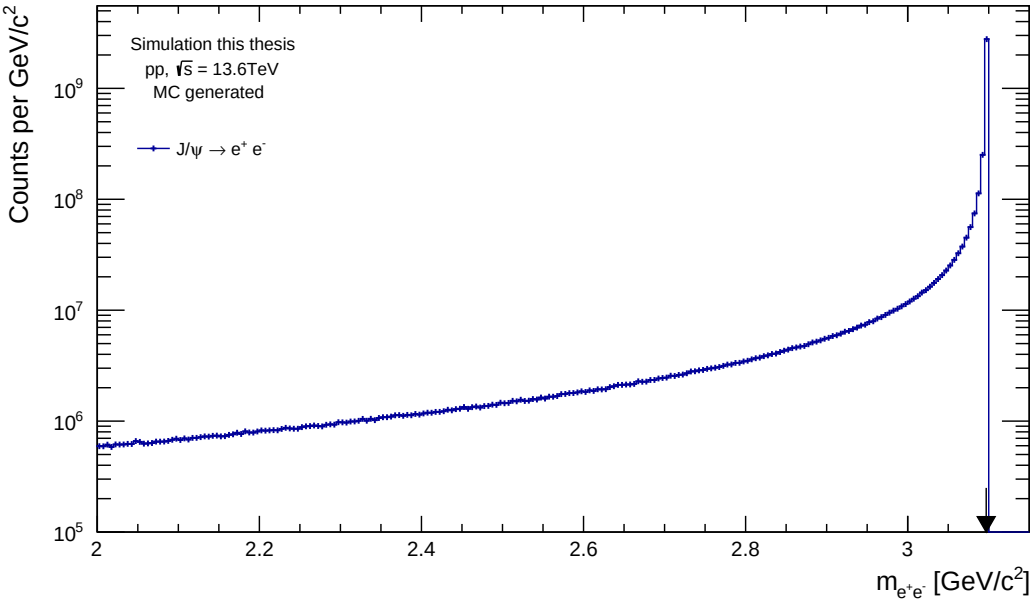

Figure 6.3: The mass distribution of MC generated true $J/\psi \to e^+e^-$; the PDG mass of J/ψ is marked with an black arrow

Figure 6.3 shows the mass distribution of the MC generated true $J/\psi \to e^+e^-$. The electron-positron pair mass exhibits a narrow, asymmetric Gaussian peak at the mass of the J/ψ. The peak is asymmetric due to the internal Bremsstrahlung tail before the peak. This internal Bremsstrahlung is a QED radiative correction to the forced decay of J/ψ to an electron-positron pair and it is described in more detail in this reference [90].

The plots corresponding to MC generated true photons are in Section 7.1.2 for the comparison with the MC reconstructed and MC reconstructed matched.

6.3 MC generated true triple candidates $\chi_c \to \gamma e^+e^-$

The developed analysis task, AnalysisDileptonPhoton, enables reconstructing MC generated true triple candidates $\chi_c \to \gamma e^+e^-$. Figure 6.4a shows the mass distribution of the MC generated true triple candidates from χ_{c1} in orange, from χ_{c2} in red and

for both χ_c in dark red markers. The triple candidates from χ_{c1} and from χ_{c2} appear as narrow peaks at 3.51 GeV/c^2 and 3.555 GeV/c^2, respectively, which correspond to their rest mass ($m^{\mathrm{PDG}}_{\chi_{c1}} = (3.51069 \pm 0.00005)$ GeV/c^2, $m^{\mathrm{PDG}}_{\chi_{c2}} = (3.55617 \pm 0.00007)$ GeV/c^2). Both peaks have Bremsstrahlungs tails consisting of internal Bremsstrahlung from J/ψ [90]. The mass peak from χ_{c1} is narrower than the mass peak from χ_{c2} because natural width of χ_{c1} ($\Gamma_{\chi_{c1}} = (0.84 \pm 0.05)$ MeV/c^2) is smaller than of χ_{c2} ($\Gamma_{\chi_{c2}} = (1.97 \pm 0.09)$ MeV/c^2). The χ_{c1} mass peak is higher due to being narrower and because more radiative χ_{c1} decays are inside the acceptance cut.

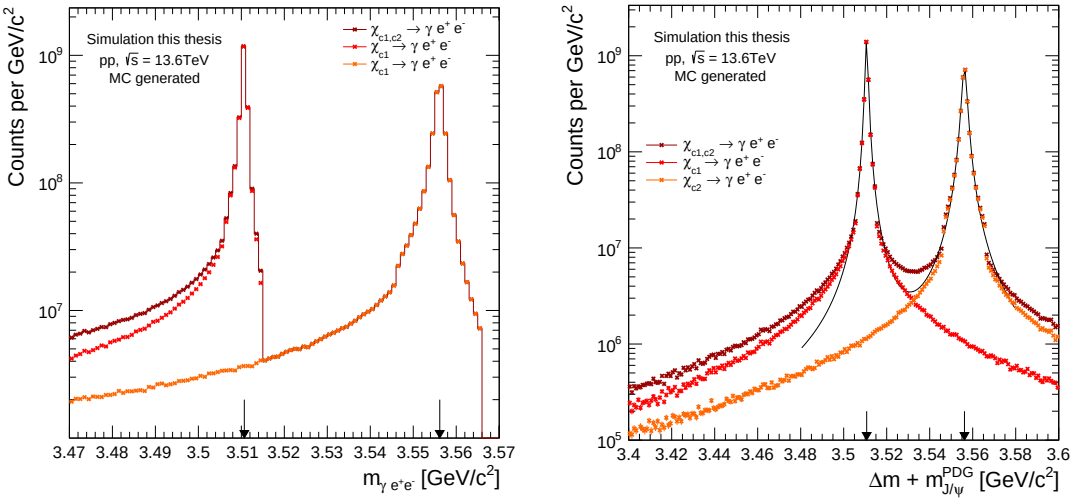

(a) **(b)**

Figure 6.4: **(a)** The mass $m_{\gamma e^+e^-}$ distribution of MC generated true triple candidates $\chi_c \to \gamma e^+e^-$ with two sharp peaks at the mass of χ_{c1} and χ_{c2}; **(b)** The $\Delta m + m^{\mathrm{PDG}}_{J/\psi}$ distribution of MC generated true triple candidates $\chi_c \to \gamma e^+e^-$ with Breit-Wigner function fits to the peaks of χ_{c1} and χ_{c2}. In both figures the locations of the PDG masses of χ_{c1} and χ_{c2} are marked with arrows.

In addition to the mass, the delta mass Δm is calculated to remove the experimental width of the J/ψ, making it possible to resolve the two mass peaks of the χ_{c1} and χ_{c2}. The delta mass Δm represents the difference between the mass of the triple candidate and the mass of the electron-positron pair:

$$\Delta m = m_{\gamma e^+e^-} - m_{e^+e^-} \tag{6.5}$$

The PDG mass of the J/ψ is added to the delta mass values to be in the mass range of the χ_c:

$$\Delta \mathrm{m} + \mathrm{m}^{\mathrm{PDG}}_{J/\psi} \tag{6.6}$$

Figure 6.4b displays the delta mass $\Delta m + m^{\mathrm{PDG}}_{J/\psi}$ distribution of the reconstructed MC generated true triple candidates $\chi_c \to \gamma e^+e^-$. The colour scheme is the same as in

the mass plot. The delta mass has also two narrow peaks. Due to removing the J/ψ width the peaks are narrower and do not have a Bremsstrahlungs tail. To determine the precise position of the mass peaks, two Breit-Wigner functions are fitted to the χ_{c1} and χ_{c2} peaks:

$$f(x) = \frac{A}{\pi} \frac{\left(\frac{\Gamma}{2}\right)^2}{(x-\mu)^2 + \left(\frac{\Gamma}{2}\right)^2} \tag{6.7}$$

The variable x represents $\Delta m + m_{J/\psi}^{\mathrm{PDG}}$, while A denotes the amplitude. The Γ corresponds to the width of the peak and the mean μ equals to the mass of the χ_c. The Breit-Wigner fits determined the mass of χ_{c1} as $m_{\chi_{c1}}^{\mathrm{generated}} = (3510.65 \pm 0.0007)$ MeV/$c^2$and the χ_{c2} mass as $m_{\chi_{c1}}^{\mathrm{generated}} = (3556.14 \pm 0.0010)$ MeV/c^2. Those values fit well with the PDG masses as expected. The determined width of the χ_{c1} mass peak is $\Gamma_{\chi_{c1}} = (1.3140 \pm 0.0011)$ MeV/c^2, while the mass peak width of χ_{c2} is $\Gamma_{\chi_{c2}} = (2.5773 \pm 0.0023)$ MeV/c^2. These determined widths are the natural width of χ_{c1} ($\Gamma_{\chi_{c1}}^{\mathrm{PDG}} = (0.84 \pm 0.04)$ MeV/c^2) and χ_{c2} ($\Gamma_{\chi_{c2}}^{\mathrm{PDG}} = (1.97 \pm 0.07)$MeV/$c^2$). The determined widths are larger than the PDG natural widths. The difference in the widths of the two peaks is visible in the Figure 6.4b. The mass peak of χ_{c1} is higher than the peak of χ_{c2} due to 151509 more forced decays in the acceptance range and because of the narrower width.

All distributions and determined values fit the expectations. Therefore, the Monte Carlo simulation was set up correctly and the new analysis task is also working properly.

7. Analysis of the Monte Carlo simulation

This chapter describes the analysis of the χ_c Monte Carlo simulation from Section 6 using the new analysis task AnalysisDileptonPhoton. Firstly, Section 7.1 focuses on the photons resulting from the radiative decay of χ_c. The photon's conversion points and reconstruction are characterised. Secondly, Section 7.2 investigates the reconstruction of dielectrons in general and in the context of J/ψ and χ_c. Thirdly, the reconstructions of the triple candidates $\gamma e^+ e^-$ are looked at in Section 7.3. The analysis considers not only the transverse momentum p_{T} distributions of photons and/or dielectrons but also other parameters, such as acceptance and efficiency. The analysis includes three types of candidates: MC generated true candidates (were explained in Section **??**), MC reconstructed matched candidates and reconstructed candidates. They were explained in Section 5.4. All three types are examined and compared in the analysis.

Analysis scripts (macros) were created to analyze the histograms in the output file (AnalysisResults.root) and to create all plots presented in Chapter 6 and 7. They have been uploaded at `https://github.com/ikantak/ChicAnalysisScripts`.

7.1 Photon reconstruction

The section on photon reconstruction is divided into three parts. The section begins by presenting the transverse momentum p_{T} distributions of all photons, as well as those that have been converted and reconstructed. Next, a comparison is made between the reconstructed, Monte Carlo matched and Monte Carlo generated true photon conversion points. Furthermore, section 7.1.3 discusses the photon conversion probability and the photon reconstruction efficiency.

The photon cut option 'nocut' applies additional cuts to the EM V0 candidates tables, in addition to the general cuts listed in Table 6.1, to obtain the photon candidates table. Table 7.1 lists the cuts used in 'nocut'. The key cuts are the TPC specific energy loss of the electrons $\frac{\mathrm{d}E}{\mathrm{d}x}\big|_e$, the cosine of pointing angle $cos(\theta_{PA})$ cut and the Armenteros-Podolanski cut. The TPC $\frac{\mathrm{d}E}{\mathrm{d}x}\big|_e$ cut only accepts electrons within a three σ area around the expected electron $\mathrm{d}E/\mathrm{d}x$. Therefore, only V0 candidates are detected which can be reconstructed with electron-positron pairs. The cosine of the pointing angle $cos(\theta_{PA})$ cut only considers V0 candidates which originate from the primary vertex. The Armeteros-Podolanski cut rejects the V0 candidates Λ, $\overline{\Lambda}$ and K_s^0 to only get photon candidates. The histograms corresponding to the three cuts are shown in the Appendix C.

Applied cuts	**min**	**max**
TPC accept electrons around $\frac{\mathrm{d}E}{\mathrm{d}x}\big\|_e$	-3σ	3 σ
cosine of pointing angle $cos(\theta_{PA})$	0.95	-
Armenteros-Podolanski cut α	-0.95	0.95
Armenteros-Podolanski cut q_{T}	0.01	-
Track p_{T}	0.04 GeV/c	10^{10} GeV/c
V0 p_{T}	0.1 GeV/c	10^{10} GeV/c
TPC number of crossed rows	20	-
TPC number crossed rows over findable clusters	0.8	-
TPC χ^2 per cluster	0.0	4.0
ITS2 χ^2 per cluster	$-1 \cdot 10^{10}$	5.0
ITS2 mean cluster size	0.0	16.0
Point of Closest Approach (PCA)	-	3.0 cm
conversion radius R_{xy}	1 cm	90 cm

Table 7.1: 'nocut' photon cuts which are applied to EM V0 candidates to get the photon candidates table

Furthermore, track quality cuts are applied to the photon candidates tables, consisting of ranges for the number of rows crossed by the signal or cluster in the TPC, average cluster size in ITS2, and ranges for the χ^2 goodness-of-fit values for each cluster in the ITS2 and TPC. Moreover, transverse momentum p_{T} cuts are applied to the tracks and V0 particles. Additionally, the Point of Closest Approach (PCA) and the conversion radius R_{xy} are tested as well for specific values.

7.1.1 Photon p_{T} distribution

Figure 7.1a displays the transverse momentum p_{T} distributions of photons. All photons which exists in the Monte Carlo simulations are represented by the dark green points. The converted photons are displayed in green, while all reconstructed photons are drawn in light green. At the beginning of all photons and converted photons, there is a dip before the sharp incline to the peak. In contrast, reconstructed photons only have a sharp increase to the peak. The dip is likely a mixture of the input distibution (p_{T}, y) of χ_c and the cuts applied. All three p_{T} distributions peak between 0.4 GeV/c and 0.5 GeV/c. The maximum is located at this transverse momentum because it is the momentum available in the χ_c radiative decay. After the maximum, the counts for all

three types of photons decrease similarly. The decrease in counts at higher energies is a result of the distribution of the kinematic energy of χ_c between the J/ψ and the photon to maintain momentum conservation, J/ψ requiring most of that energy.

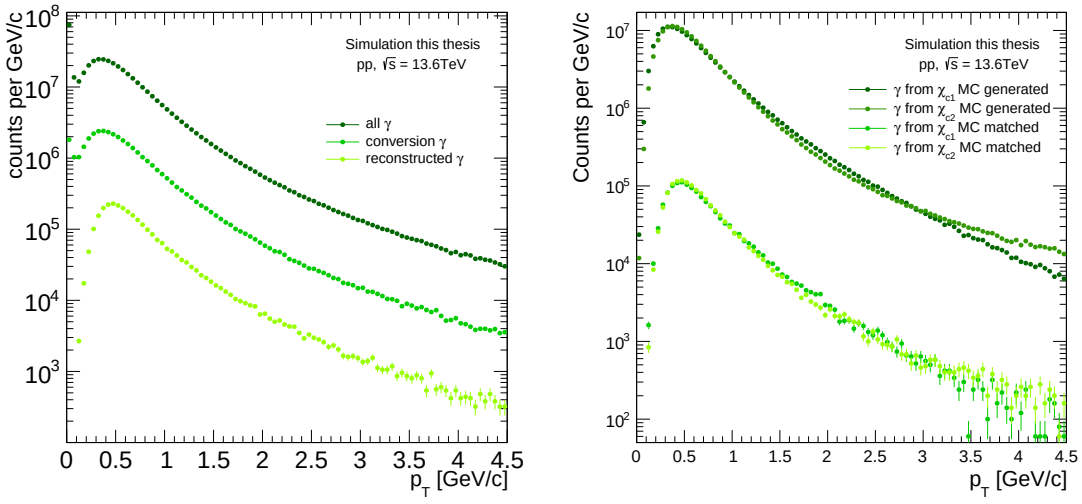

(a) **(b)**

Figure 7.1: (**a**) The transverse momentum p_{T} distributions of γ; (**b**) the transverse momentum p_{T} distributions of γ from χ_{c1} and χ_{c2} MC generated true and MC matched

Figure 7.1a displays the p_{T} distributions of the photons without any reference to other particles, while Figure 7.1b shows the photons connected to the radiative decay of χ_c. Due to the fact that all photons in the current Monte Carlo simulations are from χ_c, adding the p_{T} distributions of photons from χ_{c1} and χ_{c2} in Figure 7.1b will result in the same distribution as shown the Figure 7.1a. This is only possible because the same cuts are applied to all photons, such as the rapidity cut: $|y| < 0.9$. The MC reconstructed matched photons from χ_{c1} and χ_{c2} are represented by the two light green p_{T} distributions. Together, they represent the reconstructed p_{T} distribution shown in Figure 7.1a. The two dark green colored dots are the MC generated true photons from χ_{c1} and χ_{c2}. When combined, they provide the distribution of all the photons in the previous figure. The p_{T} distributions described below applies to both MC generated true and MC reconstructed matched photons from χ_c. Firstly, there is a sharp increase in counts until the broad maximum at 0.5 GeV/c. At the maximum of the p_{T} distributions the photons from χ_{c1} and χ_{c2} have a similar number of counts. During the decline following the peak, photons with higher counts alternate between photons from χ_{c1} and from χ_{c2}. At approximately 1.5 GeV/c, the photon count from χ_{c1} exceeds of χ_{c2}. This trend reverses at around 2.8 GeV/c, where the photon count from χ_{c2} surpasses that of χ_{c1}. The difference in photon p_{T} distribution between photons from χ_{c1} and χ_{c2} is attributed to their respective p_{T} distributions in the Monte Carlo

simulations (see Figure 6.2a). The low p_{T} of the most photons from the radiative χ_c decays indicates that the Photon conversion method is highly suitable.

7.1.2 Photon conversion points

The Figures 7.2, 7.3b and 7.3a show the MC generated true, MC matched and reconstructed conversion points of the photons in the xy vs. z plane. The x-axis corresponds to the z component of the conversion point $\mathrm{V_z}$ and the y-axis represents the conversion radius $\mathrm{R_{xy}}$:

$$\mathrm{R_{xy}} = \sqrt{V_x^2 + V_y^2} \tag{7.1}$$

The MC generated true photon conversion points are displayed in Figure 7.2. The different structures of the ALICE detector ITS2 and TPC are clearly visible. The red lines in Figure 7.2 indicate the average radius location of the ITS2 and TPC components, as listed in Table 7.2.

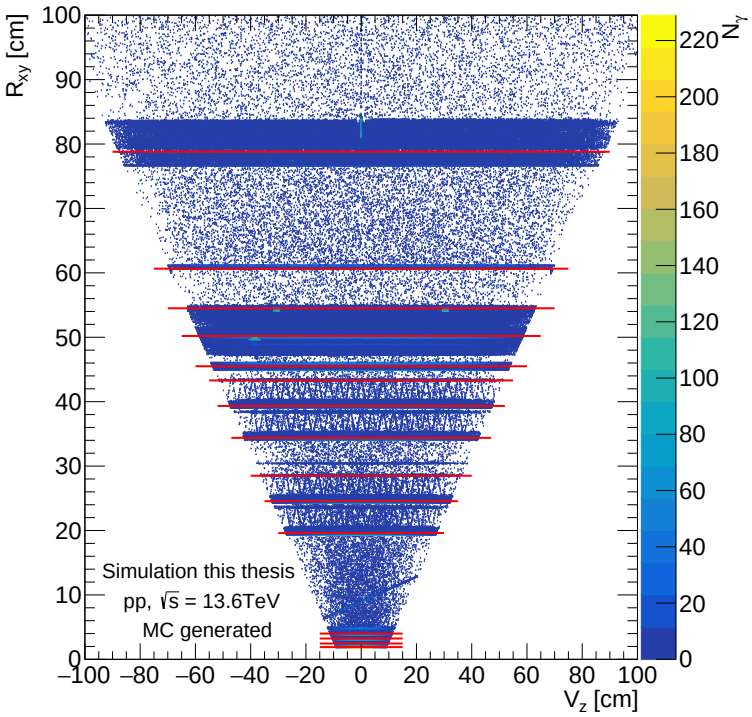

Figure 7.2: MC generated true Photon conversion points (conversion radius $\mathrm{R_{xy}}$, z-component of conversion points V_z)

As R_{xy} increases, the largest concentration of photon conversion occurs at the beam pipe at 19 mm. Then the 3 inner layers of the ITS2 silicon pixel detectors become visible between 2 cm and 4 cm of the conversion radius which fit the red lines. A calibration wire made of tungsten results in photon conversions, which is represented

by a inclined straight line from 6 cm to 12 cm in conversion radius. The four outer ITS2 layers are located at a conversion radius of 20 cm to 26 cm and 35 cm to 40 cm. They are clearly identifiable by the photon conversion taking place in the material of the layers. The thin lines located at a distance of 30 cm and 43 cm are the ITS2 support cones of the Middle Layers (MLs) and Outer Layers (OLs). After the ITS2 OLs support cones, the ITS2 Cylindrical Structural Shell (CYSS) induces the photon conversion at a conversion radius of 45 cm. The structure between 48 cm and 54 cm in conversion radius is caused by photon conversions on the support structure of the ITS2 Muon Forward Tracker (MFT). The inner containment vessel of the TPC also triggers photon conversion, which can be seen at a conversion radius of 61 cm. The photon conversions in the TPC inner field cage vessel are visible at around 80 cm.

Component	R_{xy} **[mm]**
beam pipe	19
ITS2 layer 0	24.55
ITS2 layer 1	32.35
ITS2 layer 2	39.95
ITS2 layer 3	196.05
ITS2 layer 4	245.45
ITS2 support cones Middle Layers (MLs)	285
ITS2 layer 5	343.85
ITS2 layer 6	393.35
ITS2 support cones Outer Layers (OLs)	433
ITS2 Cylindrical Structural Shell (CYSS)	445
ITS2 Muon Forward Tracker (MFT) barrel	502
ITS2 Muon Forward Tracker (MFT) cage	545
TPC inner containment vessel	606.5
TPC inner field cage vessel	788

Table 7.2: The radius R_{xy} of ITS2 and TPC components which are marked as red lines in the photon conversion points figures

The reconstructed photon conversion points matched to MC true conversion points are shown in Figure 7.3b. While, Figure 7.3a displays the reconstructed photon conversion points, i.e. including the experimental resolution. The structure of the ITS2 and TPC components in the ALICE Run 3 detector is no longer as clearly visible as it was in

Figure 7.2. As expected, the reconstructed photon conversion points exhibit the least amount of structure. In both figures, the photon reconstruction efficiency and the proximity of the layers prevent the distinction of the three innermost layers of ITS2. The tungsten calibration wire, located at the conversion radius between 6 cm and 12 cm, is also not recognizable. The sixth and seventh ITS2 layers cause more photon conversions than the the fourth and fifth layers. The ITS2 support cones for the MLs and OLs do not cause a higher intensity of photon conversions, while the ITS2 CYSS does. The majority of photon conversions occur within a conversion radius of 45 cm and 55 cm, which are caused by the ITS2 CYSS as well as the ITS2 MFT barrel and cage. Next, the TPC inner containment vessel induces photon conversions visible at around 60 cm in conversion radius. Photon conversions induced by the TPC inner field cage vessel are visible between 75 cm and 85 cm in conversion radius. Subsequently, only a few photon conversions occur due to the limited interaction of photons with the gas in the TPC.

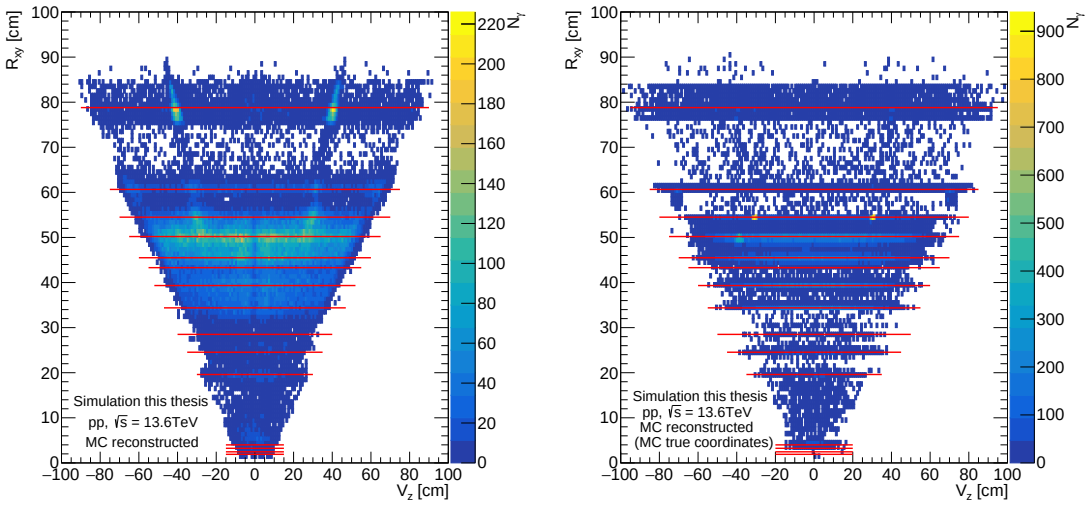

(a) **(b)**

Figure 7.3: **(a)** Mc reconstructed photon conversion points; **(b)** MC reconstructed photon conversion points matched to true conversion coordinartes; V_z = z component of conversion point, R_{xy} = conversion radius

The MC reconstructed photon conversion points have two diagonal routes with a higher intensity, which do not exist in the other two reconstructions. The routes start at -20 cm and 20 cm in the z-axis and 43 cm in the conversion radius. They then expand to -45 cm or 45 cm in z at 90 cm in the conversion radius. The higher intensities are a result of imprecise timing of the tracks to locate the photon conversion positions, which are assigned to $|\eta| = 0.5$ because it is the most probable η value. The diagonal routes exhibit a peak in photon conversions at 50 cm and 78 cm conversion radius, which is attributed to the ITS2 MFT barrel and TPC inner field cage vessel.

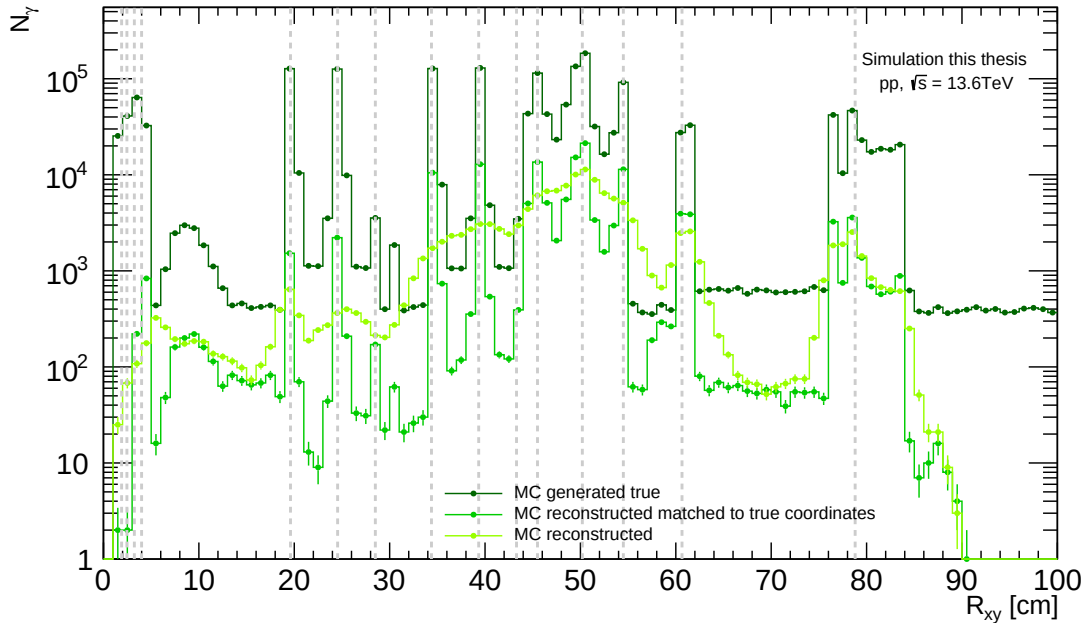

(a)

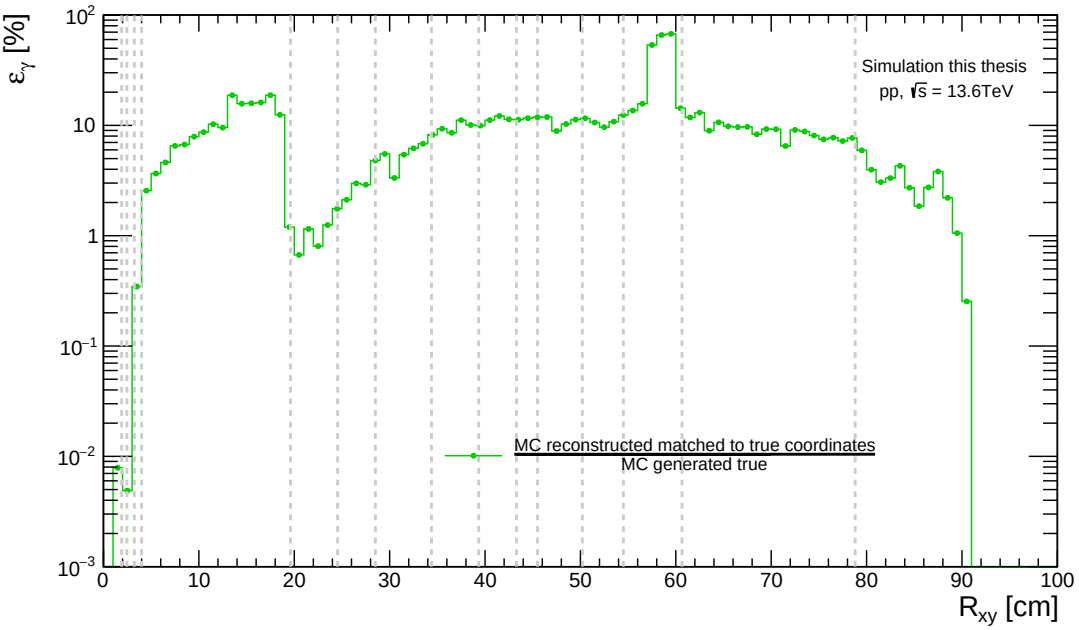

(b)

Figure 7.4: **(a)** The number of photon conversions N_γ depending on the conversion radius R_{xy} for MC generated true, MC reconstructed and MC reconstructed matched to true conversion coordinates; **(b)** photon reconstruction efficiency as a function of the conversion radius R_{xy}. The grey dashed lines are the average positions of the ITS2 and TPC components.

Figure 7.4a displays the quantity of photon conversions N_γ based on the conversion radius R_{xy} for the MC generated true (in dark-green), MC reconstructed (in light-green) and MC reconstructed matched to true conversion coordinates (in green). The locations of the ITS2 and TPC components are indicated by the grey dashed lines. The binning for all three reconstruction types was set to the same value, resulting in a relatively large binning compared to the three inner ITS2 layers. This larger binning is due to the reconstruction resolution. Due to the large binning, it is not possible to distinguish between the beam pipe and the three innermost ITS2 layers from each other. The distribution of photon conversion for MC generated true and MC reconstructed matched to MC true conversion coordinates is quite similar, with only a difference in counts. This similarity is because of the matching to the true conversion coordinates. The photon conversion distribution only deviates from the MC generated true distribution at a conversion radius of 0 cm and above 85 cm, where no photon conversions are reconstructed. At nearly all grey dashed lines, the MC generated true and MC reconstructed matched have peaks, except for the ITS2 support cones of the MLs and OLs, where the increase in photon conversions is not as prominent. Between 8 cm and 14 cm in conversion radius, there is a broad maximum caused by the calibration wire. The MC reconstructed photon conversion distribution has a lot less clear structure compared to the other two. Between 30 cm and 58 cm in conversion radius, there is just a broad maximum. Between the third and fourth ITS2 layers, there is no sharp decrease in photon conversions due to the calibration wire. Only between the TPC inner containment vessel and the TPC inner field cage vessel is a strong decrease in counts visible.

Figure 7.4b shows the reconstruction efficiency of the photon conversions as a function of the conversion radius R_{xy}. It was calculated by dividing the number of MC reconstructed photon conversions that were matched to the true conversion coordinates by the number of the MC generated true photon conversions for each conversion radius. The reconstruction efficiency typically ranges from 1% to 10%, with some minor fluctuations. The reconstruction efficiency is the closest to 100% between 56 cm and 60 cm in the conversion radius, which is the area between the ITS2 MFT cage and the TPC inner containment vessel. The reconstruction efficiency is 0% for the regions between 0 cm and 1 cm, as well as between 91 cm and 100 cm, due to the absence of reconstructed photon conversions in those regions.

7.1.3 Photon conversion probability and reconstruction efficiency

The created analysis task only considers photons that undergo photon conversion. Therefore, in order for a photon to be included in the reconstructed radiative decay of the χ_c, it has to interact with the detector's material and form photon conver-

sion. To determine the detectable photons among all photons, the photon conversion probability is calculated. This is done by dividing the number of converted photons $N_{\gamma}^{conversion}(p_{\mathrm{T}})$ at a specific transverse momentum by the MC generated true number of photons $N_{\gamma}^{\text{all }\gamma}(p_{\mathrm{T}})$ in the acceptance at the same momentum:

$$conversion_{\gamma}(p_{\mathrm{T}}) = \frac{N_{\gamma}^{\text{conversion}}(p_{\mathrm{T}})}{N_{\gamma}^{\text{MC true; photon in acceptance}}(p_{\mathrm{T}})}\Bigg|_{|y|<0.9} \tag{7.2}$$

Figure 7.5a shows the calculated photon conversion probability for the Monte Carlo simulations. The photon conversion probability is only displayed up to 4.5 GeV/c due to available statistics. The conversion probability begins at 8.8% and increases until it reaches a plateau of slightly above 11% from 2 GeV/c until 5 GeV/c.

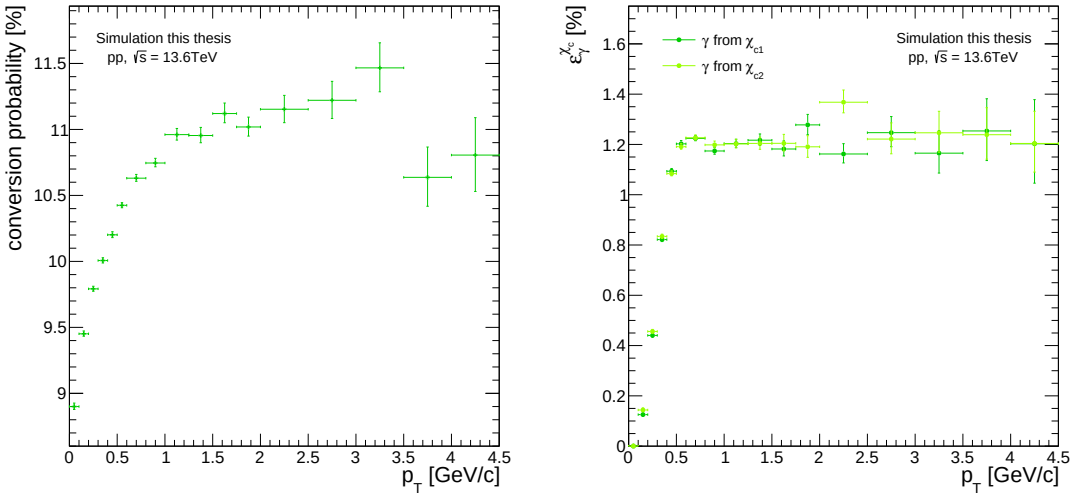

(a) **(b)**

Figure 7.5: (a) Photon conversion probability as a function of transverse momentum p_{T}; **(b)** reconstruction efficiency of γ from χ_{c1} and χ_{c2} depending on the transverse momentum p_{T}

candidates	**MC generated**	**MC matched**	**efficiency** [%]
γ from χ_{c1}	7173709	68215	0.95
γ from χ_{c2}	7064071	69700	1.00

Table 7.3: Number of reconstructable MC generated true and MC reconstructed matched photons from χ_{c1} and χ_{c2} as well as the resulting reconstruction efficiency

The number of reconstructable MC generated true and the number of MC reconstructed matched photons from χ_c are listed in Table 7.3. The average reconstruction efficiency of γ from χ_c can be calculated by dividing these numbers. The average reconstruction efficiency for photon from χ_{c1} is 0.95%, while for photons from χ_{c2} it is 1.00%. The

efficiency of reconstructing a photon at a specific transverse momentum p_{T} is calculated by dividing the number of reconstructed photons by the number of generated photons within the acceptance at that momentum:

$$\varepsilon_{\gamma}(p_{\mathrm{T}}) = \frac{N_{\gamma}^{\text{MC matched}}(p_{\mathrm{T}})}{N_{\gamma}^{\text{MC generated, photon in acceptance}}(p_{\mathrm{T}})}\Bigg|_{|y|<0.9} \tag{7.3}$$

Figure 7.5b shows the reconstruction efficiency of photons in context to χ_{c1} and χ_{c2} as a function of the transverse momentum p_{T}. At low transverse momentum p_{T}, there is a sharp increase in reconstruction efficiency from almost 0% to 1.2%. After reaching 1.2% reconstruction efficiency, a plateau ranging from 0.5 GeV/c to 4.0 GeV/c with some fluctuations is observed. The last point in the figure shows a decrease in efficiency again, which is probably due to low statistics.

All uncertainties related to efficiency and acceptance are calculated in accordance with the procedure outlined in reference [91].

7.2 Dielectron reconstruction

This section focuses on the reconstruction of dielectrons in general and from J/ψ decays with and without context to χ_c. First, the MC reconstructed electron-positron pairs are compared to the like-sign dielectrons. Secondly, MC reconstructed matched $J/\psi \rightarrow e^+e^-$ decays are characterised and then compare with the MC reconstructed electron-positron pairs with subtracted background estimated by the like-sign dilectrons. That is followed by the acceptance and reconstruction efficiency of $J/\psi \rightarrow e^+e^-$ decays. In Section 7.2.3 the transverse momentum p_{T} distributions of MC reconstructed matched dielectrons from χ_c are compared with MC generated true dielectrons from χ_c. The acceptance and reconstruction efficiency is considered as well and put in context with $J/\psi \rightarrow e^+e^-$.

Before the reconstruction of dielectrons are characterised the additional cuts applied to the electron, positron and dielectron tracks to the acceptance cuts are discussed. The 'jpsiO2MCdebugCuts2' barrel track cut was used which contains multiple cuts that are listed in Table 7.4. Three different cuts were applied to assess the track quality. The tracks in the TPC must have a χ^2 goodness-of-fit value between 0.0 and 4.0. In order to be considered, the tracks have to give a signal in at least 70 clusters in the TPC. The SPD any cut checks for hits in the first layer of the ITS2. Furthermore, three TPC $\mathrm{d}E/\mathrm{d}x$ cuts were applied to exclusively select electron tracks and reject any protons and pions. Electrons are selected based on whether they lie within the range of -3 σ to 3 σ around the expected $\mathrm{d}E/\mathrm{d}x$ of electrons. Whereas, protons or pions are selected if they are inside 3 σ to 3000 σ of the expected $\mathrm{d}E/\mathrm{d}x$ of the respective particle. With

Applied cuts	**min**	**max**
Transverse momentum p_{T}	1.0 GeV/c	1000.0 GeV/c
TPC track quality: χ^2	0.0	4.0
TPC track quality: number of clusters of a signal	70	161
TPC track quality: kIsSPDany	0.5	1.5
TPC accept electrons around $\frac{\mathrm{d}E}{\mathrm{d}x}\big\vert_e$	-3.0 σ_e	3.0 σ_e
TPC accept protons around $\frac{\mathrm{d}E}{\mathrm{d}x}\big\vert_p$	3.0 σ_p	3000.0 σ_p
TPC accept pions around $\frac{\mathrm{d}E}{\mathrm{d}x}\big\vert_\pi$	3.0 σ_π	3000.0 σ_π
Dilepton mass filter	2.5 GeV/c^2	3.2 GeV/c^2

Table 7.4: The cuts in 'jpsiO2MCdebugCuts2' applied to the barrel tracks and the dilepton mass filter applied to the dilepton tracks

this condition, almost all protons and pions are rejected. The $\mathrm{d}E/\mathrm{d}x$ of the electrons and positrons is shown in Appendix C Figure C.4.

Furthermore, a transverse momentum cut is applied to the electron or positron tracks to achieve a similar setting as in other analyses. Only electrons or positrons with transverse momentum between 1.0 GeV/c and 1000.0 GeV/c are considered for the dielectrons. Moreover, the dilepton mass filter is set to 2.5 GeV/c and 3.2 GeV/c in the configuration file because the electron-positron pairs originating from J/ψ are needed for the reconstruction of the radiative decay of χ_c.

7.2.1 Reconstruction of electron-positron pairs and like-sign dielectrons

The AnalysisSameEventPairing analysis task generates the dilepton tables. Figure 7.6 shows the mass distribution of the reconstructed electron-positron pairs and like-sign dielectrons. The pink markers represent the electron-positron pairs which show a clear peak at the PDG mass of the J/ψ which is marked with an arrow. The black markers represent the like-sign dielectrons which shows the combinatoric background of the electron-positron pairs. The representation of the combinatoric background through the like-sign dielectrons works so well because in the used Monte Carlo simulation all the electrons and positrons originate from J/ψ. This Monte Carlo simulation does not include correlated background, which would typically be present in addition to the combinatorial background. The dashed lines mark the area of the dilepton mass filter (2.5 GeV/c^2 < $m_{e^+e^-}$ < 3.2 GeV/c), which excludes many electron-positron pairs resulting from random combinatorics and cut a bit the Bremsstrahlungs tail.

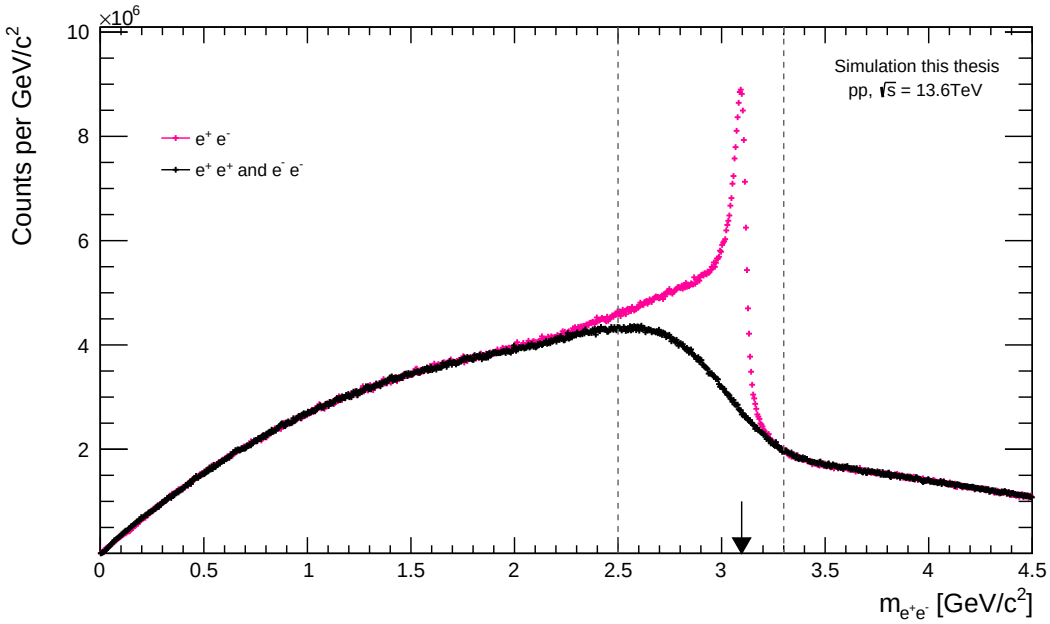

Figure 7.6: The mass distribution of electron-positron pairs e^+e^- is shown in pink. The mass of like-sign dielectrons ($e^+e^+ + e^-e^-$) is given by the black points.

7.2.2 MC reconstructed matched of $J/\psi \to e^+e^-$

In order to optimise the computing power needed for the simulation the J/ψ is forced to decay to an electron-positron pair in the Monte Carlo simulation. Figure 7.7 shows the mass distribution of the MC reconstructed matched of the electron-positron pair from J/ψ in cyan and the reconstructed e^+e^-after subtraction of like-sign dielectrons in pink. The MC reconstructed matched peak is a lot wider than the MC generated true peak in Figure 6.3. This is due to external Bremsstrahlung in addition to the internal Bremsstrahlung. In external Bremsstrahlung, the electron or positron can lose energy by emitting a photon. Furthermore, the peak is smaller as the MC generated true peak because MC reconstructed matched has less counts due to efficiency.

The mass distributions of MC reconstructed after like-sign background subtraction and MC reconstructed matched in Figure 7.7 are almost identical, with only minor differences in the number of counts. In reality, the background consists not only of combinatorial background but also of correlated background from semi-leptonic decays of heavy-flavour hadrons. The like-sign background subtraction method can only eliminate the combinatorial background, leaving behind the signal and the correlated background. Therefore, there would be more difference between MC reconstructed after like-sign background subtraction and MC reconstructed matched but in this Monte Carlo simulation there is no correlated background.

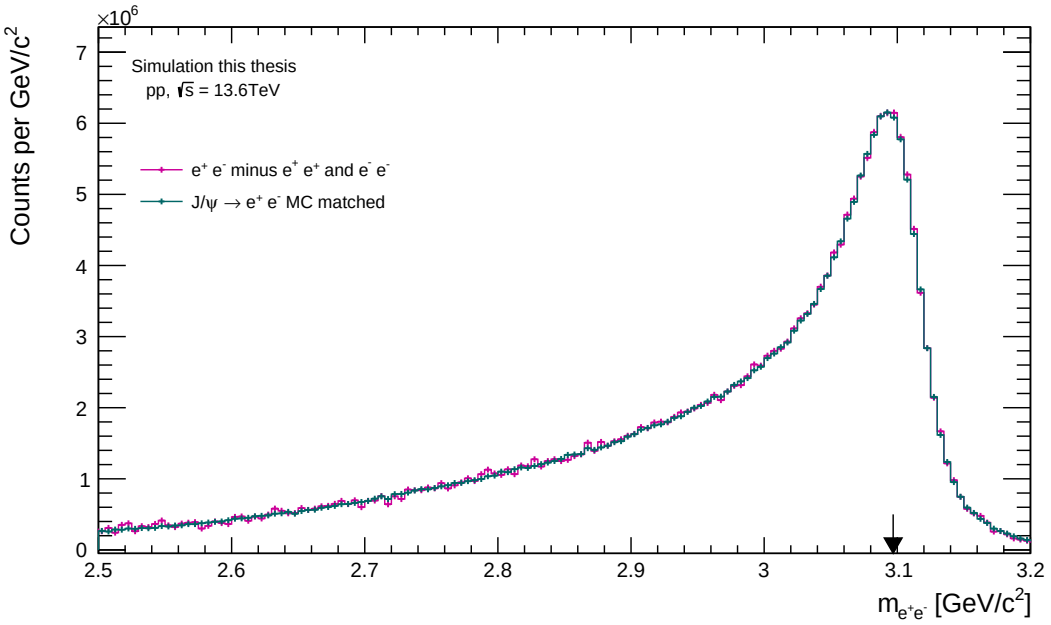

Figure 7.7: The mass distribution of $J/\psi \rightarrow e^+e^-$ MC reconstructed matched (in cyan) and e^+e^- without combinatorial background $e^+e^+ + e^-e^-$ (in pink)

The acceptance $A^{J/\psi}_{e^+e^-}$ and reconstruction efficiency $\varepsilon^{J/\psi}_{e^+e^-}$ of detecting dielectrons from the J/ψ particle using the ALICE detector can be calculated with the following equations:

$$A^{J/\psi}_{e^+e^-}(p_{\mathrm{T}}) = \left. \frac{N^{\text{electron, positron in acceptance}}_{e^+e^- \text{ from } J/\psi}(p_{\mathrm{T}})|_{|\eta|<0.9}}{N^{\text{MC generated}}_{J/\psi}(p_{\mathrm{T}})} \right|_{|y|<0.9} \tag{7.4}$$

$$\varepsilon^{J/\psi}_{e^+e^-}(p_{\mathrm{T}}) = \left. \frac{N^{\text{MC matched}}_{e^+e^- \text{ from } J/\psi}(p_{\mathrm{T}})|_{|\eta|<0.9}}{N^{\text{electron, positron in acceptance}}_{e^+e^- \text{ from } J/\psi}(p_{\mathrm{T}})} \right|_{|y|<0.9} \tag{7.5}$$

The acceptance and efficiency take for the number of electron-positron pairs at a specific transverse momentum p_{T} all e^+e^-between a mass of 2.5 GeV/c^2 and 3.2 GeV/c^2 due to the dilepton filter so most of the Bremsstrahlung tail is included in them.

Figure 7.8a displays the acceptance of J/ψ, as a function of transverse momentum when reconstructed in the e^+e^-decay mode. At low transverse momentum, the acceptance is just above 40%. As the transverse momentum increases, so does the acceptance due to decay kinematics (at 20 GeV/c the acceptance is close to 85%).

Figure 7.8b shows the efficiency of the dielectron from J/ψ. At 0.125 GeV/c transverse momentum, the efficiency is at its highest, reaching approximately 19.6%. Subsequently, the efficiency decreases to below 11% at approximately 2 GeV/c. This local minimum is probably due to the 1 GeV/c cut on both the electron and the positron. After reaching the local minimum, the efficiency increases again to above 14% at 5.5-

6 GeV/c. Following the local maximum, the efficiency constantly decreases until it reaches 1% efficiency at 20 GeV/c. The decrease in efficiency at high p_{T} is caused by the PID selection criteria (pion and proton rejection) [87]. Additional to the reconstruction efficiency depending on the transverse momentum, the overall reconstruction efficiency to reconstruct electron-positron pairs from J/ψ can be estimated. This can be done by dividing the total number of MC reconstructed matched (1098504) by the reconstructable MC generated true (8684527) $J/\psi \rightarrow e^+e^-$ resulting in an overall reconstruction efficiency of 12.65% (see Table 7.5).

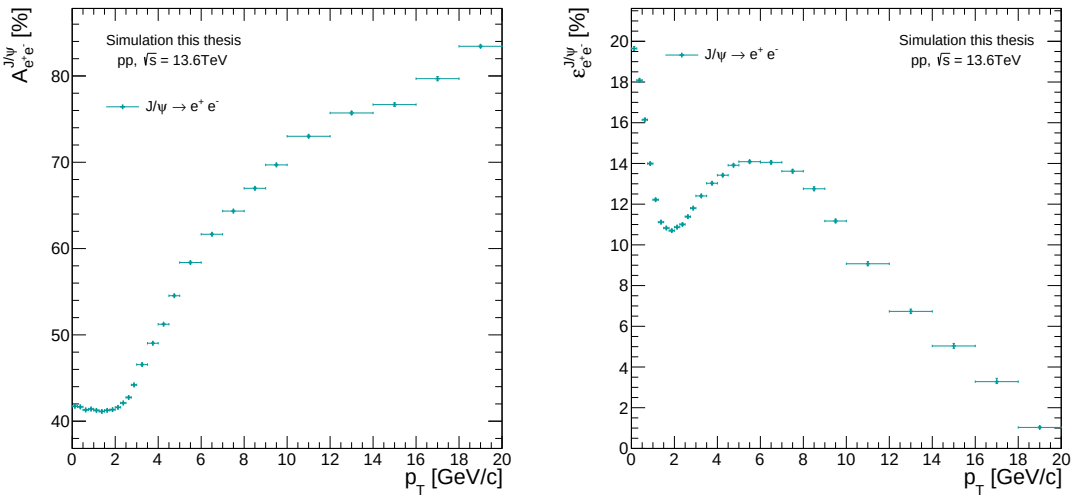

(a) **(b)**

Figure 7.8: (a) Acceptance and **(b)** reconstruction efficiency of $J/\psi \rightarrow e^+e^-$ of ALICE detector Run 3

7.2.3 MC reconstructed matched of e^+e^- from χ_c

In this part the reconstruction from electron-positron pair from χ_c is investigated. Figure 7.9a shows the p_{T}-distributions of MC generated true electron-positron pairs from J/ψ (in dark-blue), χ_{c1} (in blue) and χ_{c2} (in light-blue). At the start, there is a steep incline to the maximum. The peak of the electron-positron pairs from χ_{c2} is higher and occurs earlier than the peak of the $e^+e^-$from χ_{c1}. This is because the p_{T}-distributions of χ_{c1} and χ_{c2} in the Monte Carlo simulations. The two peaks lie approximately 0.3 GeV/c apart from each other. The peak of the $e^+e^-$from J/ψ lies between the peaks of χ_c because the $e^+e^-$from J/ψ are simply the combined events from χ_{c1} and χ_{c2}. After the peak the counts decrease fast because there are less χ_c (see Figure 6.2a).

Figure 7.9b displays the p_{T}-distributions of MC reconstructed matched electron-positron pair from J/ψ (in dark-cyan), χ_{c1} (cyan) and χ_{c2} (in light-cyan). Initially, there is a

sharp increase in counts until the peak at around 1.0 GeV/c, which is significantly earlier than the peaks of the MC generated true p_{T}-distributions. After reaching its the peak, there is a subsequent dip followed by a plateau before a decrease in the number of reconstructed $e^+e^-$from J/ψ, χ_{c1} and χ_{c2} counts. The dip and plateau observed in the momentum of the electron or positron is probably caused by the 1 GeV/c cut in transverse momentum p_{T}.

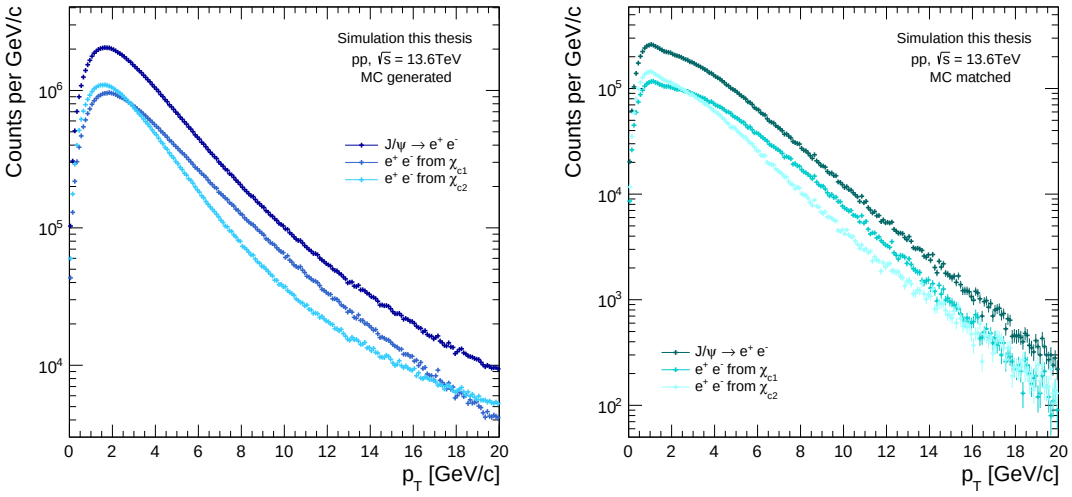

(a) **(b)**

Figure 7.9: The transverse momentum p_{T} distributions of e^+e^- from J/ψ, χ_{c1} and χ_{c2} **(a)** MC generated true and **(b)** MC reconstructed matched

The acceptance and efficiency of dielectrons from χ_c are similar to those calculated for electron-positron pair from J/ψ:

$$A^{\chi_c}_{e^+e^-}(p_{\mathrm{T}}) = \left. \frac{N^{\text{electron, positron in acceptance}}_{e^+e^- \text{ from } \chi_c}(p_{\mathrm{T}})|_{|\eta|<0.9}}{N^{\text{MC true}}_{\chi_c}(p_{\mathrm{T}})} \right|_{|y|<0.9} \tag{7.6}$$

$$\varepsilon^{\chi_c}_{e^+e^-}(p_{\mathrm{T}}) = \left. \frac{N^{\text{reconstructed}}_{e^+e^- \text{ from } \chi_c}(p_{\mathrm{T}})|_{|\eta|<0.9}}{N^{\text{MC true; electron, positron in acceptance}}_{e^+e^- \text{ from } \chi_c}(p_{\mathrm{T}})} \right|_{|y|<0.9} \tag{7.7}$$

The electron-positron pairs for the acceptance and efficiency are summed up for the different transverse momenta p_{T} with a mass filter between 2.5 GeV/c^2 and 3.2 GeV/c^2. The mass filter cuts for the acceptance around 3.5% of the internal Bremstrahlung tail in the MC generated true and for the efficiency it additionally cuts a bit of the Bremsstrahlungs tail in the MC reconstructed matched.

The acceptance of dielectrons from χ_c (as shown in Figure 7.10a) begins at 53% and then rapidly decreases to a minimum of 43% for χ_{c1} and to 41% for χ_{c2} acceptance at approximately 3 GeV/c. After the minimum the acceptance increases differently for

χ_{c1} and χ_{c2}. The acceptance of reconstructed electron-positron pairs from χ_{c1} increases until 11 GeV/c to around 53% and then slowly decrease to 49% at 20 GeV/c. While the acceptance of $e^+e^-$from χ_{c2} increases to above 65% until 20 GeV/c with some fluctuations in the rise. The acceptance of dielectrons from χ_c differs from that of dielectrons from J/ψ (Figure 7.8a). The $e^+e^-$from J/ψ do not have the drop before the minimum. The position of the minimal acceptance for dielectrons from J/ψ is before 2.0 GeV/c, whereas the $e^+e^-$from χ_c have their minimum at approximately 2.75 GeV/c. The shift in minimum position is because of the higher mass of the χ_c. After the minimum, all three acceptance rates increase. However, they reach different maxima like $J/\psi \to e^+e^-$ reach an acceptance rate of 84%, while dielectrons from χ_{c2} only reach just above 65% and from χ_{c1} only 53%.

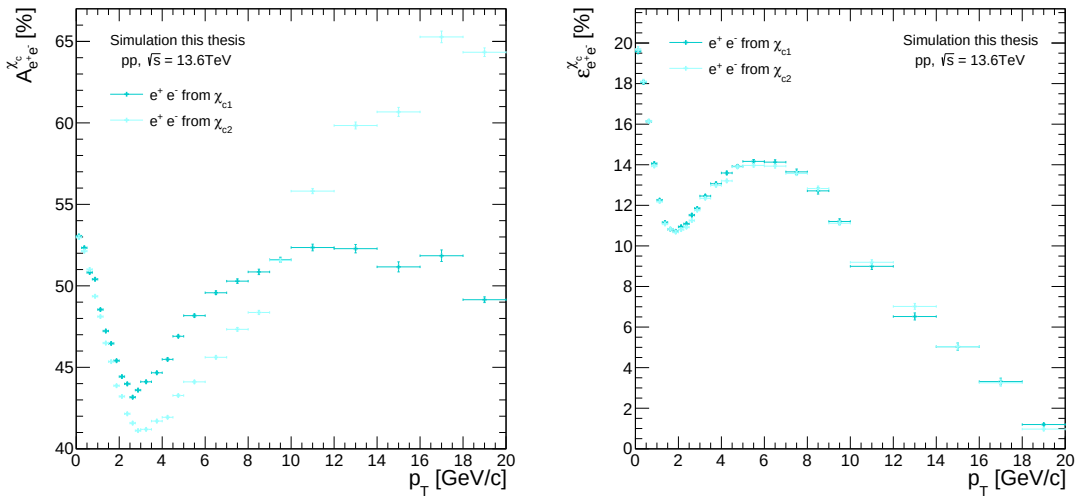

(a) **(b)**

Figure 7.10: **(a)** Acceptance and **(b)** reconstruction efficiency of e^+e^- from χ_{c1} and χ_{c2} in the Monte Carlo simulation

candidates	**MC generated**	**MC matched**	**efficiency** [%]
$J/\psi \to e^+e^-$	8684527	1098504	12.65
$e^+e^-$from χ_{c1}	4415135	560642	12.70
$e^+e^-$from χ_{c2}	4269392	537862	12.60

Table 7.5: Number of reconstructable MC generated true and MC reconstructed matched e^+e^- from J/ψ, χ_{c1} and χ_{c2} as well as the resulting reconstruction efficiency

The total reconstruction efficiency can be calculated by dividing the number of MC reconstructed matched $e^+e^-$from χ_c by the number of reconstructable MC generated true electron-positron pairs from χ_c, as listed in Table 7.5. For the total reconstruction

efficiency for $e^+e^-$from χ_{c1} is 12.70 % and for electron-positron pairs from χ_{c2} it is 12.60 %. Figure 7.10b shows the reconstruction efficiency of electron-positron pairs from χ_{c1} and χ_{c2} as a function of transverse momentum p_{T}. Both efficiencies have the same distribution, except for some differences in percentages. During the decrease to the local minimum of less than 11 %, the points of χ_{c2} are most of the time slightly lower than the percentage of χ_{c1}. This changes for the rise to the local maximum, where the dielectrons from χ_{c2} have a higher efficiency. After the local maximum, the efficiency with a higher percentage alternates between dielectrons from χ_{c1} and χ_{c2}. The efficiency distributions of dielectrons from χ_c is the same as the efficiency distribution of dielectrons from J/ψ (Figure 7.8b). The distribution is the same because all J/ψ are from the forced radiative decay of the χ_c and therefore only the J/ψ has to be connected to the χ_c.

7.3 Triple candidate reconstruction γe^+e^-

The radiative decay of the χ_c meson results in a electron-positron pair and a photon. Therefore, in order to reconstruct the χ_c, all possible γe^+e^- triple candidates are built. The triple candidates are classified into three distinct types: MC generated true triple candidates $\chi_c \to \gamma e^+e^-$ (Section 6.3), MC reconstructed triple candidates γe^+e^- (Section 7.3.1) and MC reconstructed matched triple candidates $\chi_c \to \gamma e^+e^-$ (Section 7.3.3). The mass $m_{\gamma e^+e^-}$ and the delta mass Δm (Equation 6.5) of the triple candidates are investigated and compared with each other. Furthermore, the acceptance and the efficiency of the triple candidates are calculated.

7.3.1 MC reconstructed triple candidates γe^+e^-

The reconstructed triple candidates use only information from the ALICE detector and not from Monte Carlo simulation. This means that particles from different decays that occur in the same event can be reconstructed as if they are from the same mother particle. In order to reject combinatorial background a mass cut around the J/ψ mass 2.5 GeV/c^2 $< m_{\gamma e^+e^-} <$ 3.2 GeV/c^2 is applied.

Figure 7.11a shows the mass distributions of the reconstructed triple candidates in the mass range 3.2 GeV/c^2 $< m_{\gamma e^+e^-} <$ 4.0 GeV/c^2. The chosen binning size was selected to ensure consistency when comparing it with the MC reconstructed matched triple candidates. The mass distribution exhibits a broad maximum across the entire range, peaking at approximately at 3.47 GeV/c^2. The gradient of the rise and fall before and after the maximum is approximately equal but with opposite signs. Due to that the broad maximum does not show any sharp peaks, the distribution is the combinatorial background of decay particles from different decays because there are 10 forced χ_c

decays per event.

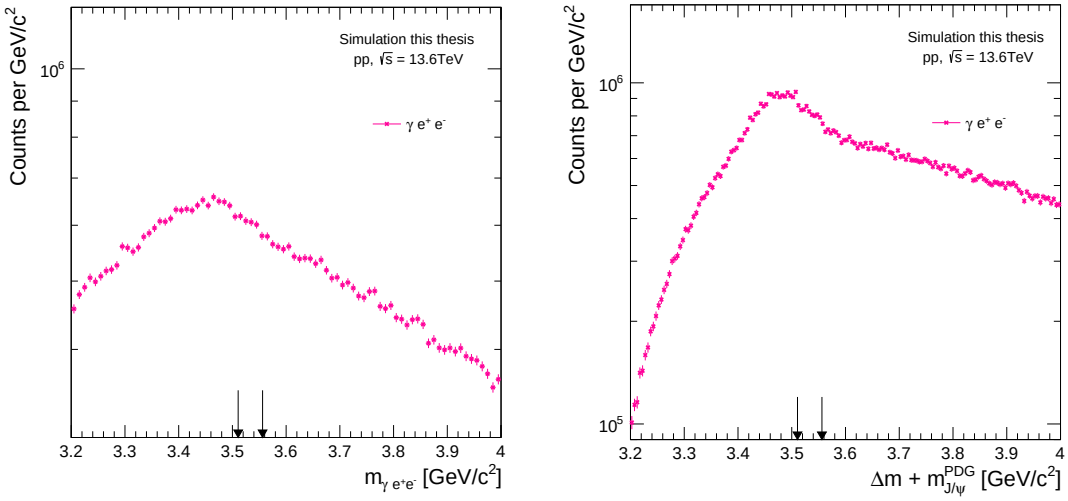

(a) **(b)**

Figure 7.11: **(a)** mass and **(b)** $\Delta m + m_{J/\psi}^{\mathrm{PDG}}$ of reconstructed triple candidates γe^+e^- in the MC simulation; In both figures the locations of the PDG masses of χ_{c1} and χ_{c2} are marked with arrows.

To remove the experimental mass resolution of reconstructed J/ψ, the Δm (see Equation 6.5) with added J/ψ PDG mass $m_{J/\psi}^{\mathrm{PDG}}$ (see Equation 6.6) is shown in Figure 7.11b. Without the width of the J/ψ the rise to the peak is sharper and higher. The position of the maximum shifts to 3.49 GeV/c^2 but the maximum is still before the rest mass of χ_{c1} and χ_{c2}. The decrease in counts after 3.55 GeV/c is linear. The shape of the peak in delta mass figure is different to the shape of the mass peak. Due to that there is still no sharp peaks visible, the peaks are probably too small compared to the combinatorial background.

7.3.2 MC reconstructed triple candidates γe^+e^- and MC reconstructed matched triple candidates $\chi_c \to \gamma e^+e^-$

This section focuses on comparing MC reconstructed triple candidates with MC reconstructed matched triple candidates. The MC reconstructed matched triple candidates $\chi_c \to \gamma e^+e^-$ consider the reconstructed particles in the ALICE detector and incorporate the Monte Carlo information. Therefore, the triple candidates are checked to verify if they originate from the same mother particle. Only if they match, are they added. This comparison checks if it is possible to see the mass peaks of χ_{c1} and χ_{c2}.

Figure 7.12a shows the mass of MC reconstructed triple candidates and MC reconstructed matched triple candidates in the mass range 3.4 GeV/c^2 $< m_{\gamma e^+e^-} <$ 3.6 GeV/c^2. Both do not show mass peaks corresponding to the χ_c rest masses which are

marked with arrows. Whereas in Figure 7.12b the delta mass with added PDG J/ψ the MC reconstructed matched displays two narrow peaks at the χ_c masses. The reconstructed triple candidates γe^+e^- show only a minimal increase in counts at the positions of the χ_{c1} mass, which could be the peak from the MC reconstructed matched triple candidates (true reconstructions) or a fluctuation. The high combinatiorial background in the MC reconstructed triple candidates γe^+e^- is due to the 10 forced radiative χ_c decays per event. The mass peaks from χ_{c1} and χ_{c2} are not visible on top of the combinatorial background based on the available statistics.

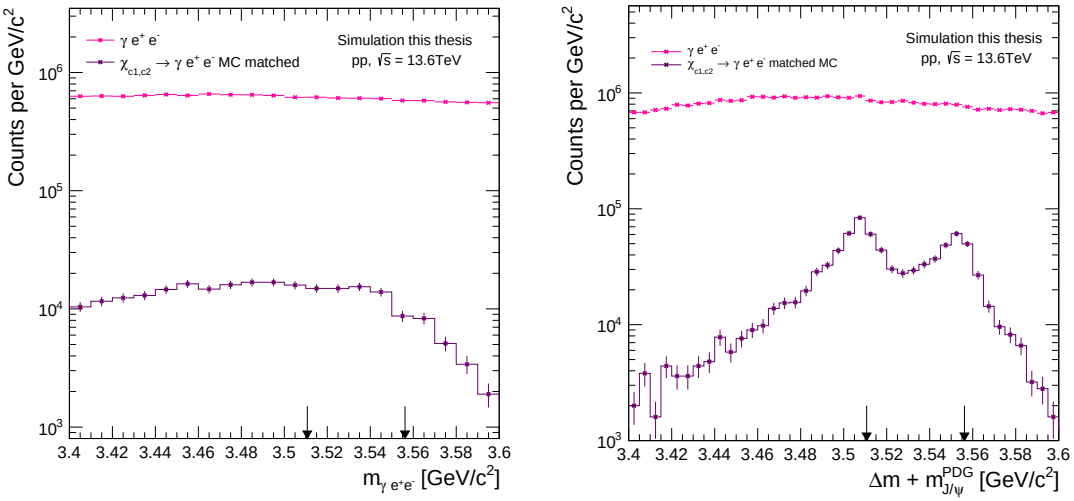

Figure 7.12: The mass **(a)** and $\Delta m + m_{J/\psi}^{\mathrm{PDG}}$ **(b)** of MC reconstructed triple candidates γe^+e^- and MC reconstructed matched triple candidates $\chi_c \to \gamma e^+e^-$. In both figures the locations of the PDG masses of χ_{c1} and χ_{c2} are marked with arrows.

7.3.3 MC reconstructed matched triple candidate $\chi_c \to \gamma e^+e^-$

This section examines the MC reconstructed matched triple candidates $\chi_c \to \gamma e^+e^-$ which use the reconstructed triple candidates and MC information to check that they originate from the same χ_c decay. The mass $m_{\gamma e^+e^-}$ and delta mass $\Delta m + m_{J/\psi}^{\mathrm{PDG}}$ distributions as well as the transverse momentum p_{T} distribution of the MC reconstructed matched triple candidates are discussed.

Figure 7.13a shows the mass distribution of the MC reconstructed matched triple candidates within the mass range 3.4 GeV/c^2 < $m_{\gamma e^+e^-}$ < 3.6 GeV/c^2. The triple candidates from χ_{c2} are drawn in light violet, and those from χ_{c1} are shown in violet. The mass of MC reconstructed matched triple candidates from χ_{c1} has a broad peak at 3.54 GeV/c^2 with a strong Bremsstrahlung tail to the left. The γe^+e^- from χ_{c1} have a smaller but wider mass peak at 3.5 GeV/c with also huge Bremsstrahlung tail. Both peaks are

located nearby the PDG mass of χ_{c1} and χ_{c2}. The mass distribution for all MC reconstructed matched triple candidates in dark-violet only shows a broad peak with some fluctuations. The mass distribution of γe^+e^- from χ_c does not show the two peaks due to the overlapping of the two peaks due to Bremsstrahlung.

When comparing the mass distributions of the MC reconstructed matched and MC generated true triple candidates $\chi_c \to \gamma e^+e^-$, they do not look similar. The two mass peaks of χ_{c1} and χ_{c2} in MC generated true (Figure 6.4a) are narrow with a small Bremsstrahlung tail and are well-separated. While MC reconstructed matched has two broad maxima with larger Bremsstrahlung tails. Despite this, the maxima are still recognisable, unlike in the MC reconstructed triple candidates γe^+e^- (Figure 7.11a).

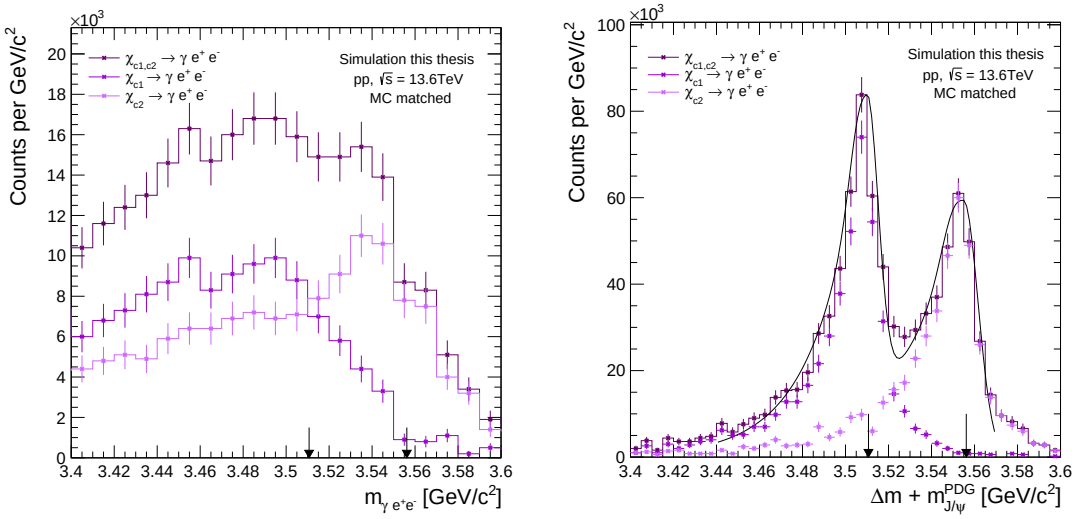

(a) **(b)**

Figure 7.13: **(a)** The mass $m_{\gamma e^+e^-}$ of MC reconstructed matched triple candidates $\chi_c \to \gamma e^+e^-$; **(b)** $\Delta m + m^{\mathrm{PDG}}_{J/\psi}$ of MC reconstructed matched triple candidates $\chi_c \to \gamma e^+e^-$ with asymmetric Gaussian fit to the peaks of χ_{c1} and χ_{c2}; In both figures the locations of the PDG masses of χ_{c1} and χ_{c2} are marked with arrows.

Once the J/ψ mass resolution is removed two clear peaks appear at the corresponding χ_{c1} and χ_{c2} rest mass. Figure 7.13b displays the delta mass Δm with the added PDG J/ψ mass of the MC reconstructed matched triple candidates γe^+e^- from χ_{c1} and χ_{c2}. The markers of the triple candidates from χ_{c1} and χ_{c2} have the same color scheme as in Figure 7.13a. The MC reconstructed matched triple candidates from χ_{c1} has a peak at approximately 3.51 GeV/c^2 whereas the MC reconstructed matched triple candidates from χ_{c2} peak at approximately 3.55 GeV/c^2 which corresponds to the PDG mass of χ_{c1} ($m^{\mathrm{PDG}}_{\chi_{c1}} = (3.51069 \pm 0.00005)$ GeV/c^2) and χ_{c2} ($m^{\mathrm{PDG}}_{\chi_{c2}} = (3.55617 \pm 0.00007)$ GeV/c^2) that are marked with black arrows in the figure. On the left of both peaks there are Bremsstrahlungs tails due to Bremsstrahlung from the electron-positron pairs from the

photon conversions. The Bremsstrahlungs tail of the mass peak of χ_{c2} reaches into the mass peak of χ_{c1}. The peaks from χ_{c1} and χ_{c2} have a difference in counts due to the different number of radiative χ_{c1} and χ_{c2} decays that lie in the acceptance cut. In the delta mass Δm of the MC reconstructed matched triple candidates from both χ_c the difference is even bigger because there the Bremsstrahlungs tail from χ_{c2} add to the counts of the peak from χ_{c1}.

To determine the exact position of the peaks an asymmetric Gaussian was fitted to the peaks:

$$f(x) = A \cdot \Big(G(x) + \exp\Big(\frac{x-\mu}{\lambda}\Big)(1 - G(x))\theta(x-\mu)\Big) \tag{7.8}$$

$$G(x) = \exp\Big(-\frac{1}{2}\Big(\frac{x-\mu}{\sigma}\Big)^2\Big) \tag{7.9}$$

The variable A is the amplitude. The Gaussian part of the fit is $G(x)$. The parameter λ represents the inverse slope of the exponential curve. The variable x corresponds to the delta mass Δm plus the PDG J/ψ mass: $x = \Delta m + m_{J/\psi}^{\mathrm{PDG}}$. The mean μ is equal to the mass of the χ_c. The width of the Gaussian part of the peak is σ. An asymmetric Gaussian was used due to the Bremsstahlung tails. For χ_{c1} a mass of $m_{\chi_{c1}} = (3509.9 \pm 0.5)$ MeV/$c^2$and for χ_{c2} a mass of $m_{\chi_{c2}} = (3554.9 \pm 0.7)$ MeV/c^2were determined. The determined width of the mass peaks are a lot bigger than the PDG values due to the reconstruction resolution from the Bremsstrahlungs tail. The parameter λ corresponds to the size of the Bremsstrahlungs tail, which shows that the Bremsstrahlungs tail of χ_{c2} ($\lambda_{\chi_{c2}} = (29.5 \pm 0.4)$ MeV/c^2) is bigger than of χ_{c1} ($\lambda_{\chi_{c1}} = (19.95 \pm 0.18)$ MeV/c^2).

	m [MeV/c^2]	**Γ or σ [MeV/c^2]**	**λ [MeV/c^2]**
χ_{c1} PDG	3510.69 ± 0.05	0.84 ± 0.04	-
χ_{c1} MC generated true	3510.65 ± 0.0007	1.3140 ± 0.0011	-
χ_{c1} MC rec. matched	3509.9 ± 0.5	5.3 ± 0.5	19.95± 0.18
χ_{c2} PDG	3556.17 ± 0.07	1.97 ± 0.09	-
χ_{c2} MC generated true	3556.14 ± 0.0010	2.5773±0.0023	-
χ_{c2} MC rec. matched	3554.9± 0.7	6.7± 0.5	29.5±0.4

Table 7.6: The mass and width parameters of $\chi_{c1}$and χ_{c2} were obtained from both the Particle Data Group (PDG) and Monte Carlo (MC) generated true and MC reconstructed matched fit functions on the $\Delta m + m_{J/\psi}^{\mathrm{PDG}}$ distributions.

In order to compare the delta mass of the MC reconstructed matched (Figure 7.13a) and MC generated true (Figure 6.4a) triple candidates $\chi_c \to \gamma e^+ e^-$ the fit parameters to the peaks from χ_{c1} and χ_{c2}, as well as the DPG values are listed in Table 7.6. A Breit-Wigner function was fit to the true delta mass peaks generated by the MC, while

an asymmetric Gaussian was used to fit the reconstructed MC. This already shows that the peaks have different shapes. The peaks in MC generated true are symmetric, whereas the MC reconstructed matched is asymmetric due to the Bremsstrahlung tails. The MC generated true fit parameters are naturally better than the MC reconstructed matched determined parameters. Furthermore, the MC reconstructed matched delta mass distribution has wider peaks due to the reconstruction resolution, compared to the MC generated true that contain only the natural width.

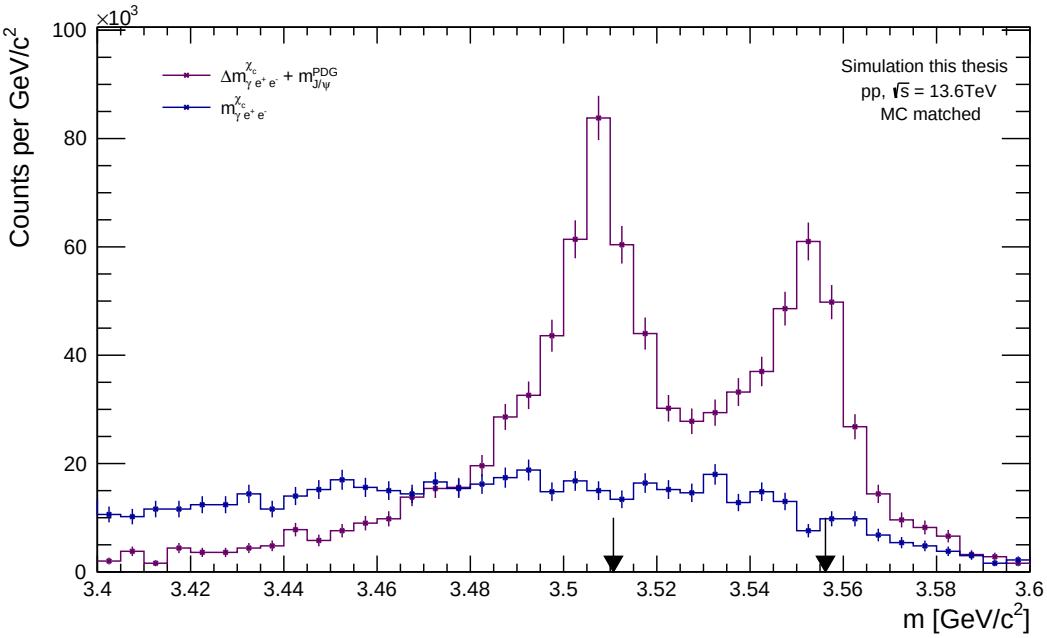

Figure 7.14: The mass $m_{\gamma e^+e^-}$ (in blue) and $\Delta m + m^{\mathrm{PDG}}_{J/\psi}$ (in violet) of MC reconstructed matched triple candidate $\chi_c \to \gamma e^+e^-$. The locations of the PDG masses of χ_{c1} and χ_{c2} are marked with arrows.

Figure 7.14 shows the mass and the delta mass (Δm) with the added J/ψ PDG mass of the MC reconstructed matched triple candidates $\chi_c \to \gamma e^+e^-$. The MC reconstructed matched delta mass has two clear peaks whereas the mass only shows a broad structure without any clear peaks. This figure demonstrates clearly the influence of the J/ψ mass resolution to the mass distribution.

Figure 7.15 shows the transverse momentum p_{T} distribution of MC reconstructed matched triple candidates $\chi_c \to \gamma e^+e^-$. The reconstruction of $\chi_c \to \gamma e^+e^-$ is possible down to 0 GeV/c. The transverse momentum p_{T} reaches the maximum at 4.5 GeV/c and then decreases slowly again.

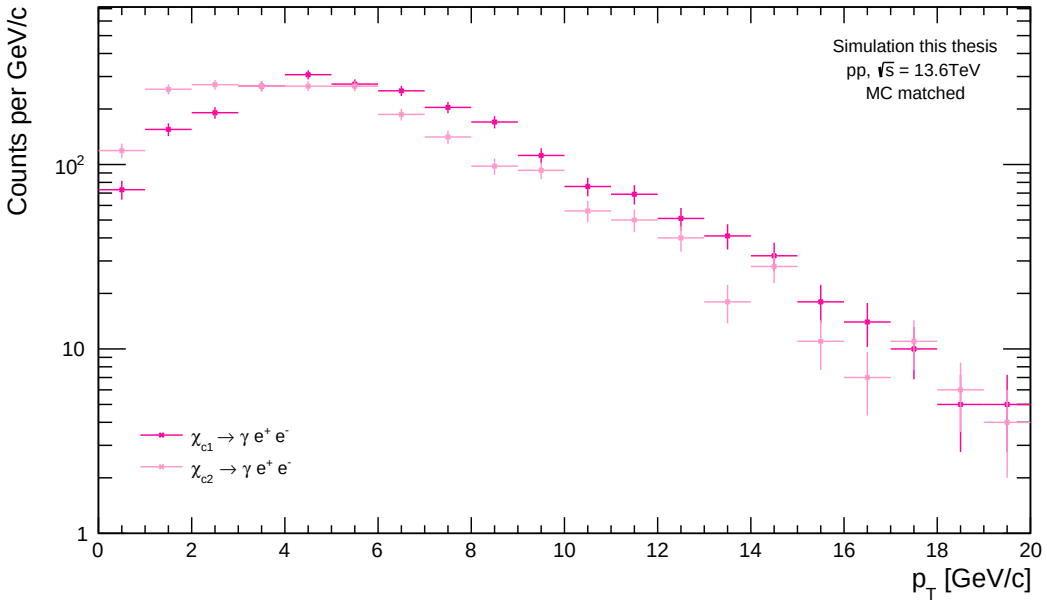

Figure 7.15: The transverse momentum p_{T} distribution of $\chi_c \to \gamma e^+ e^-$ for MC reconstructed matched

7.3.4 Acceptance and reconstruction efficiency of triple candidates $\chi_c \to \gamma e^+ e^-$

The acceptance of triple candidates $\chi_c \to \gamma e^+ e^-$ can be calculated by the ratio of the number of MC reconstructed matched photon-electron-positron triples from the χ_c with decay products in the acceptance at a specific transverse momentum to the number of MC generated true χ_c at that momentum:

$$A^{\chi_c}_{\gamma e^+ e^-}(p_{\mathrm{T}}) = \left. \frac{N^{\gamma e^+ e^- \text{ in acceptance}}_{\gamma e^+ e^- \text{ from } \chi_c}(p_{\mathrm{T}})|_{|\eta|<0.9}}{N^{\text{MC generated}}_{\chi_c}(p_{\mathrm{T}})} \right|_{|y|<0.9} \tag{7.10}$$

The χ_c, photons, electrons and positrons have to be in the rapidity and η cut. There is no mass filter applied to the triple candidates but only electron-positron pairs are used which lie in the mass range 2.5 GeV/c^2 $< m_{e^+e^-} <$ 3.2 GeV/c^2 to remove part of the Bremsstrahlung tail of the J/ψ. Figure 7.16a shows the acceptance of the reconstructable triple candidates $\chi_c \to \gamma e^+ e^-$ as a function of transverse momentum. The acceptance of χ_{c1} and χ_{c2} have the same shape with some differences in percentage. The acceptance distribution is similar to the acceptance of the electron-positron pair from J/ψ (Figure 7.8a). The acceptance at low momentum is so low due to the rapidity and η cut. With rising momentum the acceptance increases up to nearly 80%. The rise in acceptance is due to the decay kinematics.

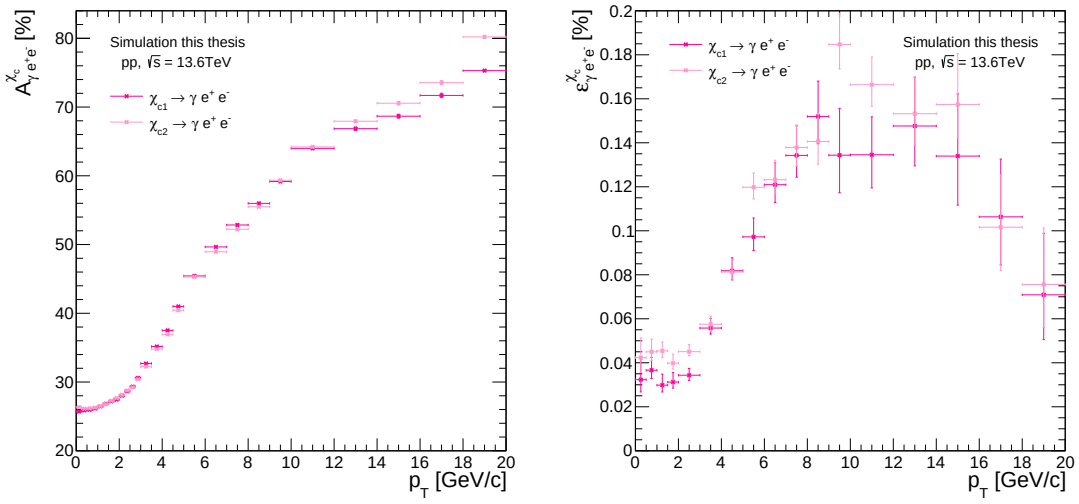

(a) **(b)**

Figure 7.16: **(a)** Acceptance and **(b)** reconstruction efficiency of $\chi_c \to \gamma e^+ e^-$ as a function of transverse momentum p_{T}

The overall reconstruction efficiency can be determined by dividing the total number of MC reconstructed matched triple candidates with the total number of reconstructable MC generated true triple candidates. The numbers for χ_{c1} and χ_{c2} triple candidates are listed in Table 7.7. The overall reconstruction efficiency for χ_{c1} is 0.0724% and for χ_{c2} is 0.0719% which is nearly the same. The reconstruction efficiency of the triple

candidates	**MC generated**	**MC matched**	**efficiency** [%]
$\chi_{c1} \to \gamma e^+ e^-$	3226492	2337	0.0724
$\chi_{c2} \to \gamma e^+ e^-$	3074983	2210	0.0719

Table 7.7: Number of reconstructable MC generated true and MC reconstructed matched $\chi_c \to \gamma e^+ e^-$ as well as the resulting reconstruction efficiency

candidates depending on the transverse momentum p_{T} can be calculated by dividing the number of the MC reconstructed matched triple candidates by the number of MC generated true triple candidates in acceptance at a given p_{T}:

$$\varepsilon^{\chi_c}_{\gamma e^+ e^-}(p_{\mathrm{T}}) = \left. \frac{N^{\text{reconstructed}}_{\gamma e^+ e^- \text{ from } \chi_c}(p_{\mathrm{T}})|_{|\eta|<0.9}}{N^{\text{MC generated; } \gamma e^+ e^- \text{ in acceptance}}_{\gamma e^+ e^- \text{ from } \chi_c}(p_{\mathrm{T}})} \right|_{|y|<0.9} \tag{7.11}$$

No mass cuts are applied to the triple candidates, only the mass filter is applied to the electron-positron pairs. Figure 7.16b shows the reconstruction efficiency of the triple candidates for χ_{c1} and χ_{c2} depending on the transverse momentum in the range 0 GeV/c < p_{T} < 20 GeV/c. The reconstruction efficiency for χ_{c1} and χ_{c2} differs slightly

in percentage but the distributions are the same. At low momentum the reconstruction efficiency is the lowest and increase after 2 GeV/c to a broad maximum of 0.155% for χ_{c1} and of approximately 0.19% for χ_{c2} between 6 GeV/c and 14 GeV/c. The peak has some fluctuations probably due to statistics. After the maximum the reconstruction efficiency decreases again to a similar percentage as at low momentum. This decrease can be due to the decrease in reconstruction efficiency of electron-positron pairs from χ_c at high momentum because of low PID efficiency (Figure 7.10b).

8. Summary and Outlook

The goal of this thesis was the development of an analysis task for the reconstruction of the radiative decay of χ_c mesons. The new analysis task, AnalysisDileptonPhoton, was successfully implemented in DQ. This tasks connects photon candidate tables from EM with dilepton tables from DQ, allowing for the χ_c reconstruction. A detailed description of the new AnalysisDileptonPhoton and other additions to the DQ framework, as well as the O2 executables were given in Chapter 5.

A specific Monte Carlo simulation (Chapter 6) with only forced radiative decays of χ_{c1} and χ_{c2} was used for debugging the analysis task in the developing phase and then it was analysed with the AnalysisDileptonPhoton to determine the acceptance and reconstruction efficiency. For all analysis steps, three different types are considered: MC generated true, MC reconstructed and MC reconstructed matched. Before taking a closer look at the triple candidates γe^+e^-, the photons and the dielectrons are analysed separately.

Firstly, the photon reconstruction was investigated. The photon conversion points provide a γ-ray tomography of the ITS2 and TPC detectors. The photon conversion probability start at 8.5% for transverse momentum values of 0 GeV/c and reaches a plateau between 1.5 GeV/c and 5 GeV/c with approximately 11.2%, albeit with some fluctuations. The efficiency to reconstruct a photon from a χ_c is mainly between 1.2% and 1.4% for $p_{\mathrm{T}} > 0.5$ GeV/c, decreasing rapidly for lower p_{T}. Therefore, the photons are the main limitation in reconstructing the radiative decay of the χ_c, particularly at low transverse momentum.

Next, the reconstruction of dileptons was characterised. The mass distribution of the MC reconstructed (matched) dileptons shows a Bremsstrahlungs tail at the peak of the J/ψ. The acceptance rate of the electron-positron pair from J/ψ or χ_c ranges from 40% to 85% or 60%. Until 3 GeV/c p_{T}, the minimum in acceptance is reached, after which the acceptance only increases. The reconstruction efficiency is the highest at very low pair momentum, with a nearly 20% efficiency rate. Between 6 GeV/c and 8 GeV/c, the efficiency reaches a local maximum of 14%. For higher transverse momentum the efficiency decreases to 1%. This is caused by the PID efficiency which drops at high transverse momentum.

Then, the triple candidates were analysed. The mass and delta mass distributions of the MC reconstructed triple candidates are continuous distributions without visible peaks in the mass area of χ_{c1} and χ_{c2}. In the MC reconstructed triple candidates, there are many incorrect combinations of detected photons, electrons, and positrons from different decays due to 10 radiative decays of χ_c per event included in the simulation. Those

incorrect combinations cause a high background, making it impossible to distinguish the peaks from the masses of χ_c's. The simulation does not include any underlying pp or PbPb event. This is important because particles produced in such underlying events such as neutral mesons can decay into electron-positron pairs for example $\pi^0 \to e^+e^-\gamma$ or photons like $\pi^0 \to \gamma\gamma$ which would also contribute to the background as well.

The MC reconstructed matched triple candidates exhibit a broad structure because the two peaks of χ_{c1} and χ_{c2} merge due to the experimental resolution. However, in the delta mass ($\Delta m = m_{\gamma e^+e^-} - m_{e^+e^-}$) figure, the peaks are narrower and resolved because the width of the reconstructed J/ψ is removed. The delta mass peaks have Bremsstrahlungs tails due to Bremsstrahlung of the dielectrons from Photon conversion. Thus, the peaks were fitted with an asymmetric Gaussian. The mass of χ_{c1} was estimated to be (3509.9 ± 0.5) MeV/c, while χ_{c2} was found to have a mass (3554.9 ± 0.7) MeV/c. The fitted masses match the PDG mass of χ_{c1} ($m^{\mathrm{PDG}}_{\chi_{c1}} = (3510.69 \pm 0.05)$ MeV/c) and χ_{c2} ($m^{\mathrm{PDG}}_{\chi_{c2}} = (3556.17 \pm 0.07)$ MeV/c). Furthermore, it was possible to reconstruct the two χ_c states down to 0 GeV/c.

The MC generated true triple candidates were analysed as well to demonstrate the proper setup of the simulation and functionality of the analysis task. The mass and the delta mass distributions two showed two narrow mass peaks for both χ_{c1} and χ_{c2}. The mass distribution had Bremsstrahlungs tails which are from the internal Bremsstrahlung of J/ψ decay. Those tails are not visible in the delta mass figure. A Breit-Wigner fit was applied to the two χ_c peaks in the delta mass figure. The mass of χ_{c1} was determined as (3510.31 ± 0.0003) GeV/c and the mass of χ_{c2} was obtained as (3556.13 ± 0.0010) GeV/c. The fitted masses and width parameters of the peaks correspond well with the PDG values.

The acceptance of the triple candidates from χ_c range between 25% and 80.5% with small differences between χ_{c1} and χ_{c2}. With increasing transverse momentum the acceptance of the triple candidates rises as well. The reconstruction efficiency of triple candidates from χ_c is always below 0.2%. The reconstruction efficiency varies slightly for χ_{c1} and χ_{c2}. Both reach a broad maximum with fluctuations between 6 GeV/c and 14 GeV/c. At low and high transverse momentum the reconstruction efficiency for χ_c is at its low with just above 0.025%.

The developed AnalysisDileptonPhoton analysis task together with all performance plots presented in Chapter 7.3 can now be used to calculate the expected number of χ_{c1} and χ_{c2} states for the recorded luminosity by ALICE in Run 3. Those numbers can be then compared to other estimations for example with [88].

This was just the beginning of the AnalysisDileptonPhoton analysis task, with many possible next steps. It is possible to include mixed events and like-sign dileptons with

photons in the analysis task as an additional process function or as an analysis task. This would make possible the estimation of the combinatorial background. DQ developers are currently implementing photon candidate tables to the DQ framework which could be used in the analysis task instead of the EM photon candidate tables. Furthermore, the AnalysisDileptonPhoton could benefit from the inclusion of photons detected with PHOS and EMCal. Currently, only photons from photon conversion are taken into account, as most of the photons in the radiative decay of χ_c have low momentum.

The AnalysisDileptonPhoton analysis task is not limited to analyse Monte Carlo simulations. Once the AnalysisDileptonPhoton analysis task commit to the DQ analysis is approved, it can be used to analyse data from ALICE Run 3. Furthermore, the AnalysisDileptonPhoton task cannot only analyse the radiative decay of χ_c, but also reconstruct other decays resulting in triple candidates consisting of a dilepton pair and a photon. For example, it can be used to analyse neutral meson Dalitz decay, like $\pi^0 \to \gamma e^+ e^-$ or $\eta \to \gamma e^+ e^-$.

The connection between the photon candidate tables from EM and the dilepton tables from DQ for the reconstruction of the χ_c meson caused several issues due to the different skimming processes used by both groups to select the events. After selecting the events, they are reindexed which prevents finding the photon and dileptons of the same event using their collision index (photon) or globalIndex (dileptons). For future analyses that use code or particles from multiple PWGs in the O^2Physics, I propose including a new event index and a new track index in the event tables that remain unchanged throughout the skimming process. This new event index and track indices would enable table connections between different PWGs in the O^2Physics, as well as future analyses that have not yet been considered.

To determine the MC generated true candidates in the runMCGen, the CheckSignal function receives as input MC particles sorted by their Monte Carlo index number. It is important to note that for the three-prong radiative χ_c decay signal, the order of the input particles is relevant. This is because the CheckSignal function will only return true if the photon is in the position where it was defined in the MCSignalLibrary. The electron-positron pair does not have an order problem on its own because the sign of the PDG code is not a condition for the signal (positive for particles and negative for anti-particles). The decay order of MC particles and their corresponding MC index numbering may not always be consistent. For instance, in the Monte Carlo simulation used, the MC generated true particles have the following decay order: $\chi_{c1} \to \gamma + J/\psi$ and $\chi_{c2} \to J/\psi + \gamma$. In other words when reconstructing a radiative χ_c event with a J/ψ and a photon, only χ_{c1} or χ_{c2} can be reconstructed. Therefore, I recommend implementing that the order of the particles in the defined signal in the MCSignalLibrary does not matter for specific cases. The testing of the possible combinations of the

input particles will increase the computing effort. This problem has not yet occured because the MCSignalLibrary contains one-prong signals or two-prong signals that are composed of the same particle. Previously, the MCSignalLibrary only contained one three-prong signal. This signal was used in the AnalysisDileptonTrack for MC reconstructed matched triple candidates consisting of an electron-positron pair and a Kaon. In the AnalysisDileptonTrack, only the MC reconstructed matched triple candidates are calculated, not the MC generated true triple candidates. When identifying MC reconstructed matched triple candidates the identity of each particle is known before using the CheckSignal function, thus the problem did not arise.

9. References

[1] Peter Braun-Munzinger and Johanna Stachel. "The quest for the quark-gluon plasma". In: *Nature Publishing Group, Insight Review* 448 (2007), pp. 302–309. DOI: https://doi.org/10.1038/nature06080.

[2] Andre Ståhl. *Experimental overview: Quarkonium production in relativistic particle collisions.* URL: https://indico.cern.ch/event/1139644/contributions/5344542/attachments/2711450/4708337/QM2023_talk.pdf. (accessed: 22.02.2024).

[3] Mark Thomas. *Modern Particle Physics.* Cambridge University Press, 2013. ISBN: 978-1-107-03426-6.

[4] CERN. *The Standard Model.* URL: https://home.cern/science/physics/standard-model. (accessed: 04.12.2023).

[5] Carsten Burgard. *Example: Standard model of physics.* URL: https://texample.net/tikz/examples/model-physics/. (accessed: 13.12.2023).

[6] Lucia Leardini. "Measurement of neutral mesons and direct photons in Pb-Pb collisions at $\sqrt{s_{\mathrm{NN}}} = 2.76$ TeV with the ALICE experiment at the LHC". In: (2017). DOI: 10.11588/heidok.00023756. URL: http://www.ub.uni-heidelberg.de/archiv/23756.

[7] Roman Pasechnik and Michal Sumbera. "Phenomenological Review on Quark-Gluon Plasma: Concepts vs. Observations". In: *Universe* 3.1 (2017), p. 7. DOI: 10.3390/universe3010007.

[8] CERN. *Heavy ions and quark-gluon plasma.* URL: https://www.home.cern/science/physics/heavy-ions-and-quark-gluon-plasma. (accessed: 04.12.2023).

[9] ALICE Collaboration. "The ALICE experiment: A journey through QCD". In: CERN-EP-2022-227 (2022). DOI: https://doi.org/10.48550/arXiv.2211.04384.

[10] CERN. *Charm is better than beauty at going with the flow.* URL: https://alice-collaboration.web.cern.ch/2023_Dec_Dmeson_flow. (accessed: 31.12.2023).

[11] Clint Young and Edward Shuryak. "Charmonium in strongly coupled quark-gluon plasma". In: *Physical Review C* 79.3 (2009). DOI: 10.1103/PhysRevC.79.034907.

[12] J.J. Aubert and Y. Y. Lee et al. "Experimental Observation of a Heavy Particle J". In: *Physical Review Letters* 33 (1974), pp. 1404–1406. DOI: https://doi.org/10.1103/PhysRevLett.33.1404.

[13] J.-E. Augustin and G.S. Abrams et al. "Discovery of a Narrow Resonance in e^+e^- Annihilation". In: *Physical Review Letters* 33 (1974), pp. 1406–1408. DOI: https://doi.org/10.1103/PhysRevLett.33.1406.

[14] R.L. Workman et. al. (Particle Data Group). "Review of Particle Physics". In: *Progress of Theoretical and Experimental Physics* 8 (2022), p. 083C01. DOI: 10.1093/ptep/ptac097. eprint: https://academic.oup.com/ptep/article-pdf/2022/8/083C01/49175539/ptac097.pdf. URL: https://doi.org/10.1093/ptep/ptac097.

[15] ALICE Collaboration. "Prompt and non-prompt J/ψ production and nuclear modification at mid-rapidity in p-Pb collisions at $\sqrt{s_{NN}}$=5.02TeV". In: *The European Physical Journal C* 78.466 (2018). DOI: https://doi.org/10.1140/epjc/s10052-018-5881-2.

[16] ALICE Collaboration. "Inclusive J/ψ production at midrapidity in pp collisions at $\sqrt{s}$ = 13TeV". In: *The European Physical Journal C* 81.12 (2021), pp. 1–18. DOI: https://doi.org/10.1140/epjc/s10052-021-09873-4.

[17] ALICE Collaboration. "Prompt and non-prompt J/ψ production cross sections at midrapidity in p-p collisions at $\sqrt{s_{NN}}$=5.02TeV and 13TeV". In: *Journal of High Energy Physics* 2022.190 (2022). DOI: 10.1007/JHEP03(2022)190. URL: https://doi.org/10.48550/arXiv.2108.02523.

[18] ATLAS Collaboration. "Measurement of χ_{c1} and χ_{c2} production with $\sqrt{s}$=7TeV pp collisions at ATLAS". In: *Journal of High Energy Physics* 2014.154 (2014). DOI: 10.1007/JHEP07(2014)154.

[19] Diego Bettoni and Roberto Calabrese. "Charmonium spectroscopy". In: *Progress in Particle and Nuclear Physics* 54.2 (2005), pp. 615–651. DOI: https://doi.org/10.1016/j.ppnp.2004.12.001.

[20] LHCb Collaboration. "Measurement of the cross-section ratio $\sigma(\chi_{c2})/\sigma(\chi_{c1})$ for prompt χ_c production at $\sqrt{s}$=7TeV". In: *Physics Letters B* 714.2-5 (2012), pp. 215–223. DOI: 10.1016/j.physletb.2012.06.077.

[21] Andrii Usachov. "Study of charmonium production using decays to hadronic final states with the LHCb experiment". In: *High Energy Physics - Experiment (hep-ex)* CERN-THESIS-2019-141 (2019). DOI: https://doi.org/10.48550/arXiv.1910.08796.

[22] CERN. *CERN's accelerator complex*. URL: https://www.home.cern/science/acceler%5C-ators/accelerator-complex. (accessed: 05.12.2023).

[23] CERN. *The Large Hadron Collider*. URL: https://home.cern/science/accelerators/large-hadron-collider. (accessed: 13.12.2023).

[24] CERN. *Our mission*. URL: https://alice-collaboration.web.cern.ch/content/mission-alice-collaboration. (accessed: 05.03.2024).

[25] CERN. *ALICE mission*. URL: https://alice-collaboration.web.cern.ch/. (accessed: 31.12.2023).

[26] Teun de Theije. "Improving the electron identification of the ALICE detector using machine learning". In: (2021). DOI: https://studenttheses.uu.nl/handle/20.500.12932/39147.

[27] CERN. *ALICE upgrade during LS2*. URL: https://home.cern/press/2022/ALICE-upgrades-LS2. (accessed: 02.01.2024).

[28] ALICE Collaboration. "ALICE upgrades during the LHC Long Shutdown 2". In: CERN-EP-2023-009 (2023). DOI: https://doi.org/10.48550/arXiv.2302.01238.

[29] CERN. *ALICE*. URL: https://home.cern/science/experiments/alice. (accessed: 18.12.2023).

[30] B Abelev et al. ALICE Collaboration. "Technical Design Report for the Upgrade of the ALICE Inner Tracking System". In: *Journal of Physics G: Nuclear and Particle Physics* 41.087002 (2014). DOI: 10.1088/0954-3899/41/8/087002.

[31] F. Reidt on behalf of the ALICE collaboration. "Upgrade of the ALICE ITS detector". In: *Nuclear Instruments and Methods in Physics Research* A.1032 (2022). DOI: https://doi.org/10.1016/j.nima.2022.166632.

[32] CERN. *ALICE ITS*. URL: https://alice-collaboration.web.cern.ch/menu_proj_items/its. (accessed: 13.12.2023).

[33] CERN. *ALICE TPC*. URL: https://alice-collaboration.web.cern.ch/menu_proj_items/tpc. (accessed: 13.12.2023).

[34] ALICE TPC collaboration. "The upgrade of the ALICE TPC with GEMs and continous readout". In: *Journal of Instrumentation (JINST)* 16 (2021). DOI: https://doi.org/10.1088/1748-0221/16/03/p03022.

[35] ALICE Collaboration. "The ALICE Transition Radiation Detector: construction, operation, and performance. The ALICE Transition Radiation Detector: construction, operation, and performance". In: *Nucl. Instrum. Methods Phys. Res., A* 881 (2017), 88–127. 40 p. DOI: 10.1016/j.nima.2017.09.028. URL: https://cds.cern.ch/record/2281131.

[36] CERN. *ALICE TRD*. URL: https://alice-collaboration.web.cern.ch/menu_proj_items/trd. (accessed: 13.12.2023).

[37] G. Dellacasa et al. "ALICE Time-Of-Flight System (TOF): Technical Design Report". In: (2000).

[38] CERN. *ALICE TOF*. URL: https://alice-collaboration.web.cern.ch/node/34978. (accessed: 13.12.2023).

[39] ALICE collaboration. "Performance of the ALICE Electromagnetic Calorimeter". In: *Journl of Intrumentation* 18 (2023). DOI: 10.1088/1748-0221/18/08/P08007. URL: https://doi.org/10.1088/1748-0221/18/08/P08007.

[40] CERN. *ALICE EmCal*. URL: https://alice-collaboration.web.cern.ch/menu_proj_items/emcal. (accessed: 02.01.2024).

[41] V. Manko, W. Klempt, L. Leistam, J. De Groot, J. Schükraft. *ALICE Photon Spectrometer (PHOS): Technical Design Report*. Tech. rep. 1999. URL: https://cds.cern.ch/record/381432.

[42] Shreyasi et al. Acharya. "Calibration of the photon spectrometer PHOS of the ALICE experiment". In: *JINST* 14.05 (2019), P05025. DOI: 10.1088/1748-0221/14/05/P05025. eprint: 1902.06145.

[43] CERN. *ALICE PHOS*. URL: https://alice-collaboration.web.cern.ch/node/34980. (accessed: 02.01.2024).

[44] Universität Heidelberg. *TPC Calibration*. URL: https://www.physi.uni-heidelberg.de/~sma/research/tpc.php. (accessed: 27.02.2024).

[45] Norbert Wermes Hermann Kolanoski. *Teilchendetektoren*. Springer-Verlag Berlin, 2016. ISBN: 978-3-662-45349-0. DOI: 10.1007/978-3-662-45350-6.

[46] Silvia Masciocchi. *Detectors for particle tracking and identification*. URL: https://www.physi.uni-heidelberg.de/~sma/teaching/GraduateDays2017/sma_Detectors_1_InteractionsWithMatter.pdf. (accessed: 27.02.2024).

[47] Wolfgang Kühn. *Detector Physics*. URL: https://indico.mitp.uni-mainz.de/event/65/attachments/1698/1781/Kuehn.pdf. (accessed: 27.02.2024).

[48] Christian Sonnabend. *ALICE TPC dE/dx performance - Run3 pp 13.6 TeV - With fitted ALEPH Bethe-Bloch parameterization*. URL: https://alice-figure.web.cern.ch/node/26843. (accessed: 27.02.2024).

[49] CMS Mattia Faggin on behalf of ALICE ATLAS and LHCb. *Tracking and Vertexing*. URL: https://alice-conferences.web.cern.ch/system/files/conferences/mfaggin/2023-05-19-LHCp2023_mfaggin_v3.pdf. (accessed: 11.01.2024).

[50] Matteo Concas for the ALICE collaboration. *A vendor-unlocked GPU reconstruction for the ALICE Inner Tracking System*. URL: https://indico.jlab.org/event/459/contributions/11383/attachments/9503/13777/CHEP2023_v3.pdf. (accessed: 24.02.2024).

[51] Marvin Hemmer. *Photon and Meson reconstruction with PCM.* URL: https://indico.cern.ch/event/1326201/contributions/5658157/attachments/2749990/4786147/Photon%20and%20Meson%20reconstruction%20with%20PCM.pdf. (accessed: 24.02.2024).

[52] R.L. Workman et al. (Particle Data Group). "34. Passage of Particles Through Matter". In: *Progress of Theoretical and Experimental Physics* 083C01 (2022). URL: https://pdg.lbl.gov/2022/reviews/rpp2022-rev-passage-particles-matter.pdf.

[53] Nikita Philip Tatsch. "Software development and validation for photon measurement in Run 3 using the photon conversion method in ALICE". In: (2022). URL: https://www.physi.uni-heidelberg.de/Publications/Bachelor_Thesis_Nikita_Philip_Tatsch.pdf.

[54] Christian Sonnabend. *Particle idenfication in ALICE and LHCb.* URL: https://alice-conferences.web.cern.ch/system/files/conferences/csonnabe/2023-05-23-LHCP2023.pdf. (accessed: 10.01.2024).

[55] ALICE Collaboration. "ALICE: Phyiscs Performance Report, Volume 2". In: *Journal of Physics G: Nuclear and Particle Physics* 32 (2006), pp. 1295–2040. DOI: 10.1088/0954-3899/32/10/001.

[56] David Baumeier. *V0 Decays: Documentation of the C++ Program AliESDv0KineCuts.cxx.* 2011. URL: https://www.uni-muenster.de/imperia/md/content/physik_kp/agwessels/thesis_db/ag_wessels/baumeier_2011_bachelor.pdf.

[57] M. Krzewicki P. Buncic and P. Vande Vyre. "Technical Design Report for the Upgrade of the Online-Offline Computing System". In: (2015). DOI: https://cds.cern.ch/record/2011297/files/ALICE-TDR-019.pdf.

[58] CERN. *ALICE O^2-PDP.* URL: https://alice-collaboration.web.cern.ch/menu_proj_items/O2-PDP. (accessed: 05.01.2024).

[59] David Rohr. *Overview of the ALICE O2 System.* URL: https://indico.phy.ornl.gov/event/112/contributions/469/attachments/496/1348/2021-12-09_Streaming_Readout_Workshop_O2.pdf. (accessed: 04.01.2024).

[60] CERN. *ALICE O^2 Project.* URL: https://alice-o2-project.web.cern.ch/. (accessed: 05.01.2024).

[61] Pierre Vande Vyvre. *ALICE Computing System for Run 3 and Run 4: the O^2 Project.* URL: https://indico.cern.ch/event/471309/contributions/1981065/attachments/1256961/1856091/O2_General_2016-04_DAQLHC_WS_PVV.pdf. (accessed: 16.01.2024).

[62] ALICE O2. *ALICEO2*. URL: https://github.com/AliceO2Group/AliceO2. (accessed: 13.01.2024).

[63] ALICE O2. *O2Physics*. URL: https://github.com/AliceO2Group/O2Physics. (accessed: 13.01.2024).

[64] David Dobrigkeit Chinellato. *Introduction to O2/O2Physics*. URL: https://indico.cern.ch/event/1326201/contributions/5580069/attachments/2746495/4779095/DDChinellato-O2AT3-Introduction-01.pdf. (accessed: 29.02.2024).

[65] AliceO2Group. *O2 Analysis Framework Documentation*. URL: https://aliceo2%5C-group.github.io/analysis-framework/. (accessed: 13.01.2024).

[66] AliceO2Group. *The O2Physics repository structure*. URL: https://aliceo2group.github.io/analysis-framework/docs/gettingstarted/theo2physicsrepo.html. (accessed: 13.01.2024).

[67] Mattia Faggin on behalf of the HF O^2 team. *HF O^2 analysis framework*. URL: https://indico.cern.ch/event/1326201/contributions/5656826/attach%5C-ments/2748212/4782703/2023Nov08_mfaggin_HFO2.pdf. (accessed: 15.01.2024).

[68] Michael Winn. *O2 DQ framework tutorial introduction: idea, structure and running*. URL: https://indico.cern.ch/event/1326201/contributions/5654566/attachments/2744511/4775105/QaT_2023_edition_Fall.pdf. (accessed: 04.01.2024).

[69] AliceO2Group. *Writing an analysis task*. URL: https://aliceo2group.github.io/analysis-framework/docs/basics-tasks/. (accessed: 16.01.2024).

[70] AliceO2Group. *Basic ingredients of an analysis task*. URL: https://aliceo2group.github.io/analysis-framework/docs/tutorials/analysistask.htmlf. (accessed: 16.01.2024).

[71] ALICE David Dobrigkeit Chinellato. *O2AT3: Hands-on session —*. URL: https://indico.cern.ch/event/1326201/contributions/5657379/attachments/2746779/4779618/DDChinellato-O2AT3-HandsOn-01.pdf. (accessed: 15.01.2024).

[72] AliceO2Group. *Dileptons-Quarkonia (DQ) analysis framework*. URL: https://aliceo2group.github.io/analysis-framework/docs/advanced-specifics/pwgdq.html. (accessed: 15.01.2024).

[73] ALICE O2. *O2Physics/PWGDQ/Tasks/TableReader.cxx*. URL: https://github.com/AliceO2Group/O2Physics/blob/master/PWGDQ/Tasks/tableReader.cxx. (accessed: 20.01.2024).

[74] Nicolas Bize. *O2 - DQ framework*. URL: https://twiki.cern.ch/twiki/bin/viewauth/ALICE/AliceO2DQFramework. (accessed: 16.01.2024).

[75] ALICE O2. *O2Physics/PWGDQ/Tasks/dqEfficiency.cxx*. URL: https://github.com/AliceO2Group/O2Physics/blob/master/PWGDQ/Tasks/dqEfficiency.cxx. (accessed: 20.01.2024).

[76] ALICE O2. *O2Physics/PWGDQ/Core/MCSignalLibrary.cxx*. URL: https://github.com/AliceO2Group/O2Physics/blob/master/PWGDQ/Core/MCSignal%5C-Library.cxx. (accessed: 29.02.2024).

[77] ALICE O2. *O2Physics/PWGDQ/Core/CutsLibrary.cxx*. URL: https://github.com/AliceO2Group/O2Physics/blob/master/PWGDQ/Core/CutsLibrary.cxx. (accessed: 29.02.2024).

[78] ALICE O2. *O2Physics/PWGDQ/Core/VarManager.h*. URL: https://github.com/AliceO2Group/O2Physics/blob/master/PWGDQ/Core/VarManager.h. (accessed: 29.02.2024).

[79] ALICE O2. *O2Physics/PWGDQ/Core/HistogramManager.cxx*. URL: https://github.com/AliceO2Group/O2Physics/blob/master/PWGDQ/Core/Histogram%5C-Manager.cxx. (accessed: 29.02.2024).

[80] ALICE O2. *O2Physics/PWGDQ/Core/HistogramManager.h*. URL: https://github.com/AliceO2Group/O2Physics/blob/master/PWGDQ/Core/Histogram%5C-Manager.h. (accessed: 29.02.2024).

[81] ALICE O2. *O2Physics/PWGDQ/Core/HistogramsLibrary.cxx*. URL: https://github.com/AliceO2Group/O2Physics/blob/master/PWGDQ/Core/HistogramsLibrary.cxx. (accessed: 29.02.2024).

[82] ALICE O2. *O2Physics/PWGDQ/Core/MCProng.cxx*. URL: https://github.com/AliceO2Group/O2Physics/blob/master/PWGDQ/Core/MCProng.cxx. (accessed: 29.02.2024).

[83] ALICE O2. *O2Physics/PWGDQ/Core/MCProng.h*. URL: https://github.com/AliceO2Group/O2Physics/blob/master/PWGDQ/Core/MCProng.h. (accessed: 29.02.2024).

[84] ALICE O2. *O2Physics/PWGDQ/Tasks/MCSignal.h*. URL: https://github.com/AliceO2Group/O2Physics/blob/master/PWGDQ/Core/MCSignal.h. (accessed: 23.02.2024).

[85] Felix Schlepper. *SVertexer with TPC-only tracks*. URL: https://indico.cern.ch/event/1351889/contributions/5696031/attachments/2762206/4810535/291123.pdf. (accessed: 28.02.2024).

[86] Alica Marie Endrich (Supervisor Silvia Masciocchi). *Performance study on photon measurements using the Photon Conversion Method with ALICE in Run 3*. 2024.

[87] Private Communication with Dr. A. Marin.

[88] Carlotta Rosenthal (Supervisor Yvonne Pachmayer). *Estimated number of χ_c-states in pp collisions at $\sqrt{s}$=13 TeV with ALICE in LHC Run 3*. 2022. URL: https://www.physi.uni-heidelberg.de/Publications/BSc_Rosenthal.pdf.

[89] LHCb Collaboration. "Measurement of the ratio of prompt χ_c to J/ψ production in pp collisions at $\sqrt{s}$=7TeV". In: *Physics Letters B* 718.2 (2012), pp. 431–40. DOI: https://doi.org/10.1016/j.physletb.2012.10.068.

[90] Elisabetta Barberio and Zbigniew Was. "PHOTOS - a universal Monte Carlo for QED radiative corrections: version 2.0". In: *Computer Physics Communications* 79 (1994), pp. 291–308. DOI: https://doi.org/10.1016/0010-4655(94)90074-4.

[91] Marc Paterno. "Calculating Efficiencies and their uncertainties". In: *FERMILAB-TM-2286-CD* (2004). DOI: 10.2172/15017262. URL: https://doi.org/10.2172/15017262.

A. Overview of variables

variables	Definition
A	Acceptance
A	Amplitude
A	Atomic mass of the medium
α_s	Strong coupling constant
β	Velocity of the particle
$\mathcal{BR}$	Branching ratio
C	Charge-conjugation
c	Speed of light
δ	Density correction
Δm	Delta mass
$\frac{\mathrm{d}E}{\mathrm{d}x}$	Specific energy loss
$\frac{d\sigma}{dx}$	Differential cross section
ε	Efficiency
η	Pseudorapidity
$E_{1,2}$	Energy of daughter 1,2 from V0 particle
$E_{e^+e^-}$	Energy of the electron or positron
E_γ	Photon energy
γ	Lorentz factor $\gamma = \frac{1}{\sqrt{1-\beta^2}}$
Γ	Full width
$G(x)$	Gaussian
I	Mean excitation energy
J	Spin

Appendix A. Overview of variables

variables	definition
K	$4\pi N_A r_e^2 m_e c^2 = 0.307$ MeV g^{-1}cm^2
λ	Inverse gradient of the exponential curve of the Gaussian
M	Mass of incident particle
m	Mass
$m_{1,2}$	Mass of daughter 1,2 from V0 particle
m_e	Electron mass
$m_{e^+e^-}$	Mass of electron-positron pair
$m_{\gamma e^+e^-}$	Mass of triple candidate (γe^+e^-)
m_{inv}	Invariant mass of the V0 particle
$m_{J/\psi}^{\text{PDG}}$	PDG mass of J/ψ
μ	Mean of the Breit-Wigner and asymmetric Gaussian functions
N_A	Avogadro constant
$N(p_{\text{T}})$	Number of candidates at a specific transverse momentum
P	Parity
$p_{1,2}$	Four momentum vector of daughter 1,2 from V0 particle
$p_{1,2}$	Three dimensional momentum vector of daughter 1,2 from V0 particle
p_{T}	Transverse momentum
ρ	Density of the medium
R_{max}	Maximal radius of ITS2 layer
R_{min}	Minimal radius of ITS2 layer
R_{xy}	Conversion radius in xy
σ	Width of the Gaussian peak
σ_P	Cross section of photon pair production
θ	Heaviside step function

variables	definition
θ_{PA}	Pointing angle
T_c	Critical temperature of the QGP
T_{max}	Maximum energy transfer in a single collision
V_z	z component of the conversion point
X_0	Absorption length
x	Fractional energy the electron or positron receive from the photon
x	$\Delta m + m_{J/\psi}^{\mathrm{PDG}}$ for Breit-Wigner and asymmetric Gaussian functions
y	Rapidity
Z	Charge number of the medium
z	Charge of incident particle

Table A.1: Variables definitions

B. Configuration file for AnalysisDileptonPhoton in dqEfficiency

```
{
    "internal-dpl-clock": "",
    "internal-dpl-aod-reader": {
        "time-limit": "0",
        "orbit-offset-enumeration": "0",
        "orbit-multiplier-enumeration": "0",
        "start-value-enumeration": "0",
        "end-value-enumeration": "-1",
        "step-value-enumeration": "1",
        "aod-file": "@fileMC_ChiC.txt"
    },
    "internal-dpl-aod-spawner": "",
    "internal-dpl-aod-index-builder": "",
    "timestamp-task": {
        "verbose": "false",
        "rct-path": "RCT\/Info\/RunInformation",
        "orbit-reset-path": "CTP\/Calib\/OrbitReset",
        "ccdb-url": "http:\/\/alice-ccdb.cern.ch",
        "isRun2MC": "false"
    },
    "track-propagation": {
        "ccdb-url": "http:\/\/alice-ccdb.cern.ch",
        "lutPath": "GLO\/Param\/MatLUT",
        "geoPath": "GLO\/Config\/GeometryAligned",
        "grpmagPath": "GLO\/Config\/GRPMagField",
        "mVtxPath": "GLO\/Calib\/MeanVertex",
        "minPropagationDistance": "83.0999985",
        "useTrackTuner": "false",
        "trackTunerParams": "debugInfo=0|updateTrackCovMat=1|updateCurvature=0|updatePulls=0|
isInputFileFromCCDB=1|pathInputFile=Users\/m\/mfaggin\/test\/inputsTrackTuner\/PbPb2022|nameInputFile=
trackTuner_DataLHC22sPass5_McLHC22l1b2_run529397.root|usePvRefitCorrections=0|oneOverPtCurrent=0|
oneOverPtUpgr=0",
        "processStandard": "false",
        "processStandardWithPID": "false",
        "processCovarianceMc": "false",
        "processCovariance": "true",
        "processCovarianceWithPID": "false"
    },
    "bc-selection-task": {
        "triggerBcShift": "999",
        "ITSROFrameBorderMargin": "30",
        "processRun2": "false",
        "processRun3": "true"
    },
    "event-selection-task": {
        "syst": "pp",
        "muonSelection": "0",
        "customDeltaBC": "300",
        "isMC": "true",
        "processRun2": "false",
        "processRun3": "true"
    },
    "track-selection": {
        "isRun3": "false",
        "produceTable": "-1",
        "produceFBextendedTable": "-1",
        "compatibilityIU": "false",
        "itsMatching": "0",
        "dcaSetup": "0",
        "ptMin": "0.100000001",
        "ptMax": "1e+10",
        "etaMin": "-0.800000012",
        "etaMax": "0.800000012"
    },
    "pid-multiplicity": {
        "processIU": "false",
        "processStandard": "true"
    },
    "multiplicity-table": {
        "doVertexZeq": "1",
```

Figure B.1: Configurations in the JSON file for running AnalysisDileptonPhoton task in the dqEfficiency.cxx, page 1

```
68          "fractionOfEvents": "2",
69          "enabledTables": {
70              "labels_rows": [
71                  "FV0Mults",
72                  "FT0Mults",
73                  "FDDMults",
74                  "ZDCMults",
75                  "TrackletMults",
76                  "TPCMults",
77                  "PVMults",
78                  "MultsExtra",
79                  "MultZeqs",
80                  "MultsExtraMC"
81              ],
82              "labels_cols": [
83                  "Enable"
84              ],
85              "values": [
86                  [
87                      "-1"
88                  ],
89                  [
90                      "-1"
91                  ],
92                  [
93                      "-1"
94                  ],
95                  [
96                      "-1"
97                  ],
98                  [
99                      "-1"
100                 ],
101                 [
102                     "-1"
103                 ],
104                 [
105                     "-1"
106                 ],
107                 [
108                     "-1"
109                 ],
110                 [
111                     "-1"
112                 ],
113                 [
114                     "-1"
115                 ]
116             ]
117         },
118         "ccdburl": "http:\/\/alice-ccdb.cern.ch",
119         "ccdbpath": "Centrality\/Calibration",
120         "processRun2": "false",
121         "processRun3": "true"
122     },
123     "tpc-pid-full": {
124         "param-file": "",
125         "ccdb-url": "http:\/\/alice-ccdb.cern.ch",
126         "ccdbPath": "Analysis\/PID\/TPC\/Response",
127         "recoPass": "",
128         "ccdb-timestamp": "0",
129         "useNetworkCorrection": "false",
130         "autofetchNetworks": "true",
131         "skipTPCOnly": "false",
132         "networkPathLocally": "network.onnx",
133         "networkPathCCDB": "Analysis\/PID\/TPC\/ML",
134         "enableNetworkOptimizations": "true",
135         "networkSetNumThreads": "0",
136         "pid-el": "1",
137         "pid-mu": "1",
```

Figure B.2: Configurations in the JSON file for running AnalysisDileptonPhoton task in the dqEfficiency.cxx, page 2

```
138         "pid-pi": "1",
139         "pid-ka": "1",
140         "pid-pr": "1",
141         "pid-de": "-1",
142         "pid-tr": "-1",
143         "pid-he": "-1",
144         "pid-al": "-1"
145     },
146     "create-emevent": {
147         "processEvent": "false",
148         "processEventMC": "true",
149         "processEvent_Cent": "false",
150         "processEventMC_Cent": "false",
151         "processDummy": "false"
152     },
153     "photon-conversion-builder": {
154         "ccdb-url": "http:\/\/alice-ccdb.cern.ch",
155         "grpPath": "GLO\/GRP\/GRP",
156         "grpmagPath": "GLO\/Config\/GRPMagField",
157         "lutPath": "GLO\/Param\/MatLUT",
158         "geoPath": "GLO\/Config\/GeometryAligned",
159         "skipGRPOquery": "true",
160         "d_bz": "-999",
161         "useMatCorrType": "0",
162         "min_ncluster_tpc": "10",
163         "mincrossedrows": "10",
164         "maxchi2tpc": "4",
165         "maxchi2its": "5",
166         "maxpt_itsonly": "0.150000006",
167         "maxTPCNsigmaEl": "4",
168         "dcanegtopv": "0.100000001",
169         "dcapostopv": "0.100000001",
170         "min_pt_leg": "0.0500000007",
171         "maxX": "83.0999985",
172         "min_v0cospa_tpconly": "0.99000001",
173         "min_v0cospa_its": "0.99000001",
174         "max_dcav0dau_tpconly": "3",
175         "max_dcav0dau_its": "0.5",
176         "max_dcav0dau_itsibss": "1",
177         "max_dcav0dau_tpc_inner_fc": "1.5",
178         "min_v0radius": "1",
179         "margin_r_its": "3",
180         "margin_r_tpconly": "7",
181         "margin_z": "7",
182         "max_alpha_ap": "0.949999988",
183         "max_qt_ap": "0.0149999997",
184         "min_pt_v0": "0.100000001",
185         "max_pt_v0_itsonly": "0.300000012",
186         "max_eta_v0": "0.899999976",
187         "kfMassConstrain": "-1",
188         "max_r_req_its": "16",
189         "min_r_tpconly": "10",
190         "max_r_itsmft_ss": "66",
191         "max_dcatopv_xy_v0": "1e+10",
192         "max_dcatopv_z_v0": "1e+10",
193         "processRec": "false",
194         "processMC": "true"
195     },
196     "tof-signal": {
197         "ccdb-url": "http:\/\/alice-ccdb.cern.ch",
198         "ccdb-timestamp": "-1",
199         "timeShiftCCDBPath": "",
200         "distanceForGoodMatch": "999",
201         "distanceForGoodMatchLowMult": "999",
202         "multThreshold": "0",
203         "processRun3": "true",
204         "processRun2": "false"
205     },
206     "associate-photon-to-emevent": {
207         "processPCM": "true",
```

Figure B.3: Configurations in the JSON file for running AnalysisDileptonPhoton task in the dqEfficiency.cxx, page 3

```
208         "processDalitzEE": "false",
209         "processDalitzMuMu": "false",
210         "processPHOS": "false",
211         "processEMC": "false",
212         "processZeroPadding": "true"
213     },
214     "associate-mc-info": {
215         "max_rxy_gen": "100",
216         "processMC_PCM": "true",
217         "processMC_PCM_DalitzEE": "false",
218         "processMC_PCM_DalitzEE_DalitzMuMu": "false",
219         "processMC_PHOS": "false",
220         "processMC_EMC": "false",
221         "processMC_PCM_PHOS": "false",
222         "processMC_PCM_PHOS_DalitzEE": "false",
223         "processMC_PCM_EMC": "false",
224         "processMC_PCM_EMC_DalitzEE": "false",
225         "processMC_PHOS_EMC": "false",
226         "processMC_PCM_PHOS_EMC": "false",
227         "processMC_PCM_PHOS_EMC_DalitzEE": "false",
228         "processDummy": "false"
229     },
230     "tof-event-time": {
231         "inheritFromBaseTask": "true",
232         "ccdb-url": "http:\/\/alice-ccdb.cern.ch",
233         "ccdb-timestamp": "-1",
234         "minMomentum": "0.5",
235         "maxMomentum": "2",
236         "maxEvTimeTOF": "100000",
237         "sel8TOFEvTime": "false",
238         "maxNtracksInSet": "10",
239         "paramFileName": "",
240         "parametrizationPath": "TOF\/Calib\/Params",
241         "passName": "",
242         "loadResponseFromCCDB": "false",
243         "enableTimeDependentResponse": "false",
244         "fatalOnPassNotAvailable": "true",
245         "processRun2": "false",
246         "processNoFT0": "true",
247         "processFT0": "false",
248         "processOnlyFT0": "false"
249     },
250     "tof-pid": {
251         "inheritFromBaseTask": "true",
252         "ccdb-url": "http:\/\/alice-ccdb.cern.ch",
253         "ccdb-timestamp": "-1",
254         "paramFileName": "",
255         "parametrizationPath": "",
256         "passName": "",
257         "timeShiftCCDBPath": "",
258         "loadResponseFromCCDB": "false",
259         "enableTimeDependentResponse": "false",
260         "fatalOnPassNotAvailable": "true",
261         "enableParticle": {
262             "labels_rows": [
263                 "El",
264                 "Mu",
265                 "Pi",
266                 "Ka",
267                 "Pr",
268                 "De",
269                 "Tr",
270                 "He",
271                 "Al"
272             ],
273             "labels_cols": [
274                 "Enable"
275             ],
276             "values": [
277                 [
```

Figure B.4: Configurations in the JSON file for running AnalysisDileptonPhoton task in the dqEfficiency.cxx, page 4

```
278                     "-1"
279                 ],
280                 [
281                     "-1"
282                 ],
283                 [
284                     "-1"
285                 ],
286                 [
287                     "-1"
288                 ],
289                 [
290                     "-1"
291                 ],
292                 [
293                     "-1"
294                 ],
295                 [
296                     "-1"
297                 ],
298                 [
299                     "-1"
300                 ],
301                 [
302                     "-1"
303                 ]
304             ]
305         },
306         "processWSlice": "true",
307         "processWoSlice": "false"
308     },
309     "tof-pid-full": {
310         "inheritFromBaseTask": "true",
311         "ccdb-url": "http:\/\/alice-ccdb.cern.ch",
312         "ccdb-timestamp": "-1",
313         "paramFileName": "",
314         "parametrizationPath": "",
315         "passName": "",
316         "timeShiftCCDBPath": "",
317         "loadResponseFromCCDB": "false",
318         "enableTimeDependentResponse": "false",
319         "fatalOnPassNotAvailable": "true",
320         "enableParticle": {
321             "labels_rows": [
322                 "El",
323                 "Mu",
324                 "Pi",
325                 "Ka",
326                 "Pr",
327                 "De",
328                 "Tr",
329                 "He",
330                 "Al"
331             ],
332             "labels_cols": [
333                 "Enable"
334             ],
335             "values": [
336                 [
337                     "-1"
338                 ],
339                 [
340                     "-1"
341                 ],
342                 [
343                     "-1"
344                 ],
345                 [
346                     "-1"
347                 ],
```

Figure B.5: Configurations in the JSON file for running AnalysisDileptonPhoton task in the dqEfficiency.cxx, page 5

```
348                 [
349                     "-1"
350                 ],
351                 [
352                     "-1"
353                 ],
354                 [
355                     "-1"
356                 ],
357                 [
358                     "-1"
359                 ],
360                 [
361                     "-1"
362                 ]
363             ]
364         },
365         "processWSlice": "true",
366         "processWoSlice": "false"
367     },
368     "pcm-qc-mc": {
369         "cfgPCMCuts": "nocut",
370         "maxY": "0.899999976",
371         "maxRgen": "100",
372         "margin_z_mc": "7",
373         "processQCMC": "true",
374         "processGen": "true",
375         "processDummy": "false"
376     },
377     "tof-pid-beta": {
378         "tof-expreso": "80",
379         "paramFileName": "",
380         "ccdb-url": "http:\/\/alice-ccdb.cern.ch",
381         "parametrizationPath": "TOF\/Calib\/Params",
382         "passName": "",
383         "ccdb-timestamp": "-1",
384         "fatalOnPassNotAvailable": "true",
385         "enableTOFParams": "false"
386     },
387     "table-maker-m-c": {
388         "cfgEventCuts": "eventStandardtest",
389         "cfgBarrelTrackCuts": "jpsiO2MCdebugCuts2",
390         "cfgMuonCuts": "muonQualityCuts",
391         "cfgAddEventHistogram": "triggerall,cent,mc",
392         "cfgAddTrackHistogram": "dca,its,tpcpid,tofpid,mc",
393         "cfgAddMuonHistogram": "muon,mc",
394         "cfgAddMCTruthHistogram": "",
395         "cfgBarrelLowPt": "0.5",
396         "cfgMuonLowPt": "0.5",
397         "cfgMinTpcSignal": "30",
398         "cfgMaxTpcSignal": "300",
399         "cfgMCsignals": "electronFromPC,dielectronFromPC,eFromJpsi,eeFromJpsi,Jpsi,Chic1,Chic2,
    JpsiFromChic1,eFromJpsiFromChic1,eeFromJpsiFromChic1,PhotonFromChic1,JpsiFromChic2,eFromJpsiFromChic2,
    eeFromJpsiFromChic2,PhotonFromChic2,PhotonFromChic12",
400         "cfgIsRun2": "false",
401         "cfgQA": "true",
402         "cfgDetailedQA": "false",
403         "cfgIsAmbiguous": "false",
404         "ccdb-url": "http:\/\/alice-ccdb.cern.ch",
405         "cfgPropMuon": "false",
406         "geoPath": "GLO\/Config\/GeometryAligned",
407         "grpmagPath": "GLO\/Config\/GRPMagField",
408         "grpmagPathRun2": "GLO\/GRP\/GRP",
409         "processFull": "false",
410         "processFullWithCov": "false",
411         "processBarrelOnly": "false",
412         "processBarrelOnlyWithMults": "false",
413         "processBarrelOnlyWithCent": "false",
414         "processBarrelOnlyWithCentAndMults": "false",
415         "processBarrelOnlyWithCov": "true",
```

Figure B.6: Configurations in the JSON file for running AnalysisDileptonPhoton task in the dqEfficiency.cxx, page 6

```
416         "processBarrelOnlyWithDalitzBits": "false",
417         "processMuonOnly": "false",
418         "processMuonOnlyWithCov": "false",
419         "processMuonOnlyWithCent": "false",
420         "processOnlyBCs": "true",
421         "processAmbiguousMuonOnly": "false",
422         "processAmbiguousMuonOnlyWithCov": "false",
423         "processAmbiguousBarrelOnly": "false"
424     },
425     "analysis-event-selection": {
426         "cfgEventCuts": "eventStandardtest",
427         "cfgQA": "true",
428         "processSkimmed": "true",
429         "processDummy": "false"
430     },
431     "analysis-muon-selection": {
432         "cfgMuonCuts": "muonQualityCuts",
433         "cfgMuonMCSignals": "muFromJpsi",
434         "cfgQA": "true",
435         "processSkimmed": "false",
436         "processDummy": "true"
437     },
438     "analysis-track-selection": {
439         "cfgTrackCuts": "jpsiO2MCdebugCuts2",
440         "cfgTrackMCSignals": "eFromJpsi,eFromLMeeLF",
441         "cfgQA": "true",
442         "processSkimmed": "true",
443         "processDummy": "false"
444     },
445     "analysis-same-event-pairing": {
446         "cfgTrackCuts": "jpsiO2MCdebugCuts2",
447         "cfgMuonCuts": "muonQualityCuts",
448         "cfgBarrelMCRecSignals": "dielectronFromPC,eeFromJpsi,Jpsi,Chic1,Chic2,eeFromJpsiFromChic1,
    eeFromJpsiFromChic2,PhotonFromChic2",
449         "cfgBarrelMCGenSignals": "electronFromPC,dielectronFromPC,eFromJpsi,eeFromJpsi,Jpsi,Chic1,Chic2,
    JpsiFromChic1,eFromJpsiFromChic1,eeFromJpsiFromChic1,PhotonFromChic1,JpsiFromChic2,eFromJpsiFromChic2,
    eeFromJpsiFromChic2,PhotonFromChic2,PhotonFromChic012",
450         "cfgFlatTables": "false",
451         "cfgUseKFVertexing": "false",
452         "cfgUseRemoteField": "false",
453         "cfgMagField": "5",
454         "ccdburl": "http:\/\/alice-ccdb.cern.ch",
455         "grpmagPath": "GLO\/Config\/GRPMagField",
456         "cfgUseAbsDCA": "false",
457         "cfgPropToPCA": "false",
458         "cfgCorrFullGeo": "false",
459         "cfgNoCorrFwdProp": "false",
460         "lutPath": "GLO\/Param\/MatLUT",
461         "geoPath": "GLO\/Config\/GeometryAligned",
462         "processDecayToEESkimmed": "true",
463         "processDecayToEEVertexingSkimmed": "false",
464         "processDecayToMuMuSkimmed": "false",
465         "processDecayToMuMuVertexingSkimmed": "false",
466         "processDummy": "false"
467     },
468     "analysis-dilepton-photon": {
469         "cfgPhotonCuts": "nocut",
470         "cfgDileptonLowMass": "2.79999995",
471         "cfgDileptonHighMass": "3.20000005",
472         "cfgFillCandidateTable": "false",
473         "cfgBarrelMCRecSignals": "eeFromJpsi,eFromJpsiFromChic1,eeFromJpsiFromChic1,PhotonFromChic1,
    eeFromJpsiFromChic2,PhotonFromChic2,PhotonFromChic012,eePhotonFromChic1,eePhotonFromChic2,
    eePhotonFromChic12",
474         "cfgBarrelMCGenSignals": "electronFromPC,dielectronFromPC,eFromJpsi,eeFromJpsi,Jpsi,Chic1,Chic2,
    JpsiFromChic1,eFromJpsiFromChic1,eeFromJpsiFromChic1,PhotonFromChic1,JpsiFromChic2,eFromJpsiFromChic2,
    eeFromJpsiFromChic2,PhotonFromChic2,PhotonFromChic012,eePhotonFromChic1,eePhotonFromChic2,
    eePhotonFromChic12",
475         "cfgAcceptanceCut": "true",
476         "processDielectronPhotonSkimmed": "true",
477         "processDummy": "false"
```

Figure B.7: Configurations in the JSON file for running AnalysisDileptonPhoton task in the dqEfficiency.cxx, page 7

```
478     },
479     "analysis-dilepton-track": {
480         "cfgLeptonCuts": "muonQualityCuts",
481         "cfgFillCandidateTable": "false",
482         "cfgBarrelMCRecSignals": "eeFromJpsi,eeFromJpsiFromChic1,eeFromJpsiFromChic2",
483         "cfgBarrelMCGenSignals": "eFromJpsi,Jpsi,Chic1,Chic2,JpsiFromChic1,eFromJpsiFromChic1,
    PhotonFromChic1,JpsiFromChic2,eFromJpsiFromChic2,PhotonFromChic2,PhotonFromChic012",
484         "processDimuonMuonSkimmed": "false",
485         "processDielectronKaonSkimmed": "true",
486         "processDummy": "false"
487     },
488     "internal-dpl-aod-writer": "",
489     "internal-dpl-aod-global-analysis-file-sink": "",
490     "internal-dpl-injected-dummy-sink": ""
491 }
```

Figure B.8: Configurations in the JSON file for running AnalysisDileptonPhoton task in the dqEfficiency.cxx, page 8

C. Distributions of cut variables

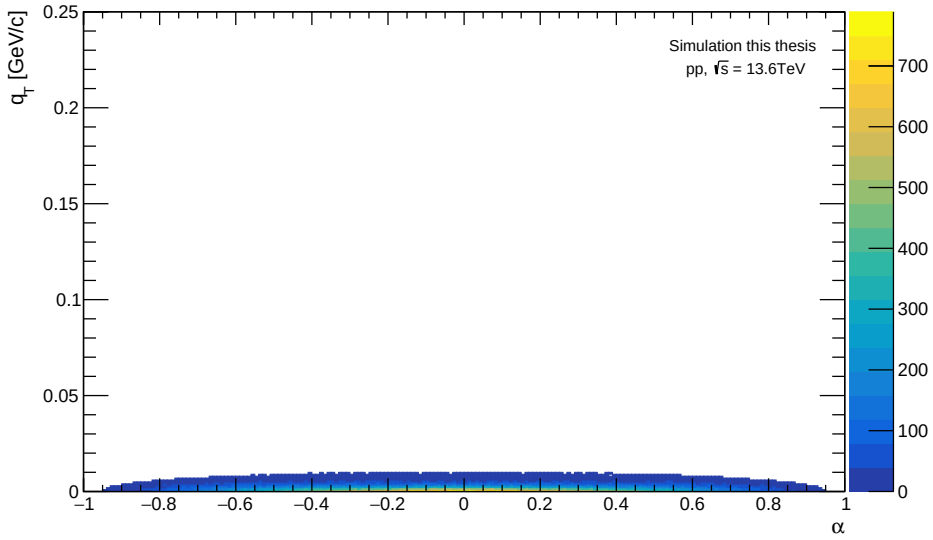

Figure C.1: Armenteros-Podolanski distribution for γ candidates

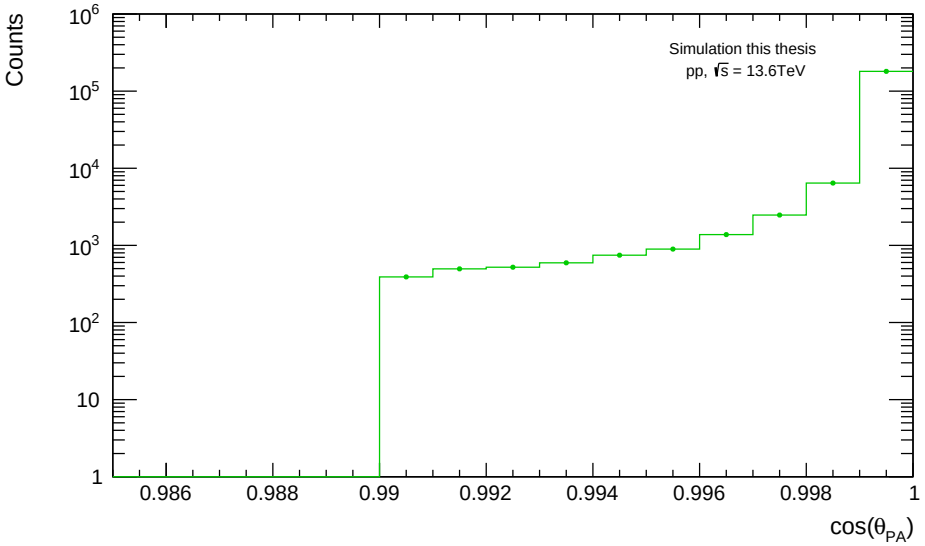

Figure C.2: Cosine of pointing angle

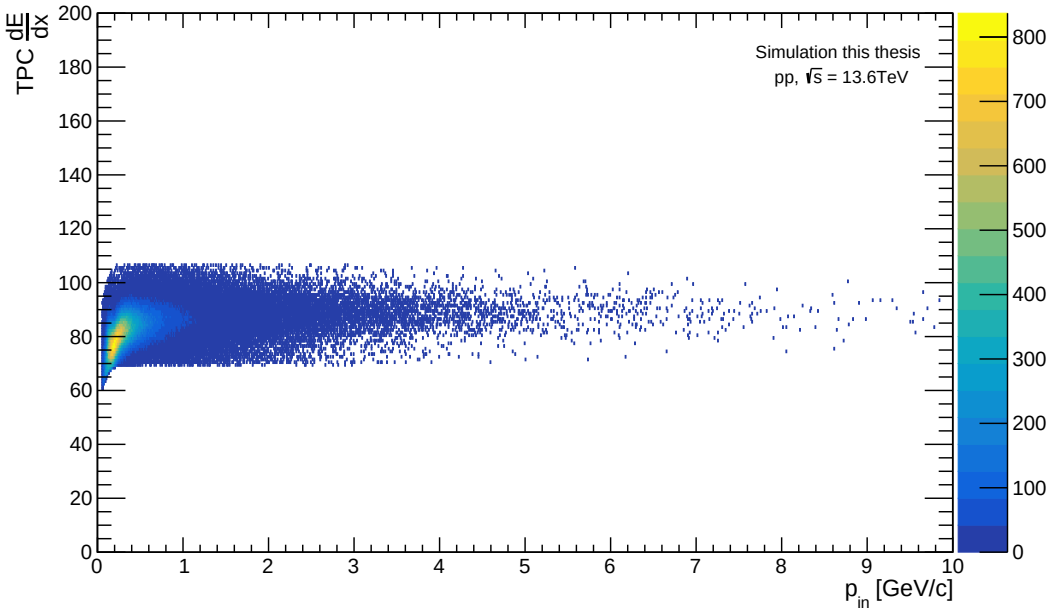

Figure C.3: $\mathrm{d}E/\mathrm{d}x$ signal of electrons from Photon conversion as a function of momentum

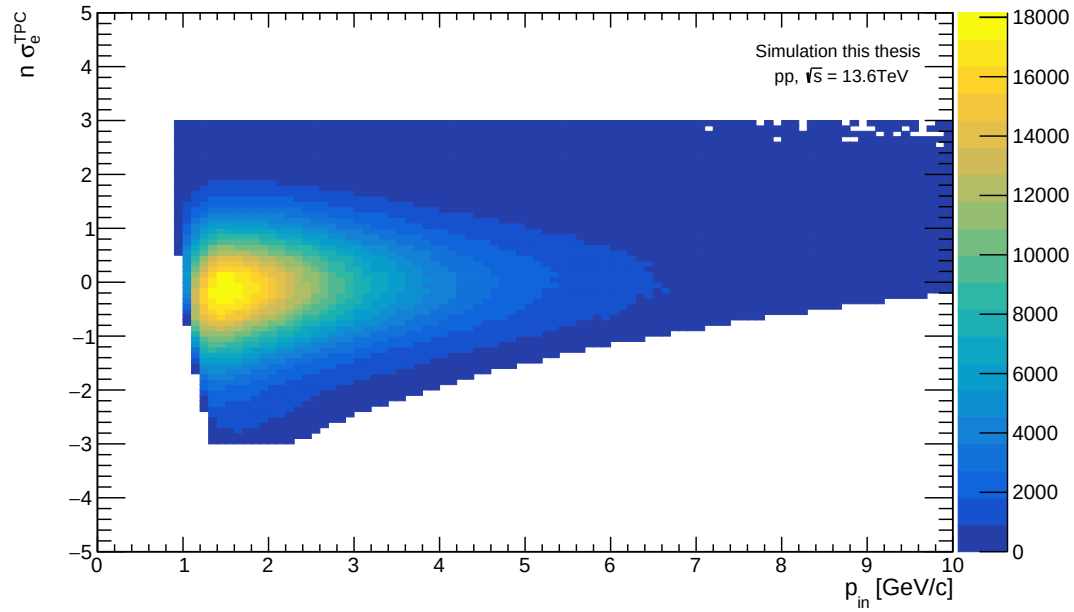

Figure C.4: $\mathrm{d}E/\mathrm{d}x$ signal in number of sigmas with respect to the expected electron line as a function of momentum for primary electrons

D. Difficulties

During the coding of the AnalysisDileptonPhoton task in the DQ analysis framework, several difficulties were encountered. The photons are so far not a part of the DQ analysis framework. Therefore, the photons for the AnalysisDileptonPhoton task were taken from the EM analysis framework which lead to two main index difficulties.

Firstly, the various analysis frameworks have different skimming processes because they need different events. After the event selection, all events are reindexed. Therefore, it is not possible to get the electron-positron pair and the photon from the same event by calling the globalIndex for the dileptons and collisionId for the photons. This index problem was temporarily solved by avoiding to cut any events in the event selection process in the DQ and EM.

Secondly, another index problem occured when matching the EM photon to DQ MC tracks because the EM MC particles keep less particles than the DQ MC tracks which results in different indices. This was solved by identifying the EM photon in the DQ MC track with the PDG code (photon = 22) and the MC transverse momentum p_{T} value of the photon. It was necessary to determine the track of the photon in order to verify the origin of the photon from a χ_c.

Furthermore, in the coding process it was discovered that the input particles in the CheckSignal function must have the same order as the defined MC signal except for particle and antiparticle. This is a problem for the MC generated true candidates because there the MC particles are put into the CheckSignal function after their globalIndex. The triple candidates in the MC signal for the radiative decay of χ_c were defined as $e^+e^-\gamma$ or $e^-e^+\gamma$. However, the photon always has a smaller globalIndex than the electron and positron because they are decay products from the J/ψ. This problem was solved by switching the order of the input particles of the CheckSignal function in the three-prong case of the runMCGen. Now the input particle with the smallest globalIndex is given at the third position. The order of the input particles of the CheckSignal function was also considered for the MC reconstructed matched triple candidates. However, it is important to note that the identity of each particle is known with certainty in that case.

E. Acknowledgements

Firstly, I would like to thank Prof. Dr. Johanna Stachel for giving me the opportunity to write my bachelor thesis under her supervision in the ALICE Group at the Physikalische Institut. I also want to thank Prof. Dr. Klaus Reygers for being the second examiner of my thesis.

I would like to express my heartfelt appreciation to Dr. Ana Marin for her guidance, her great commitment and her enduring support throughout the entire process of this thesis. I am grateful for her guidance regarding the O^2Physics analysis framework and for her explanations of the O^2 or O^2Physics error messages. Additionally, I am thankful for her assistance during the extensive debugging process. Moreover, I want to thank her for answering all my questions as well as for her proofreading and providing valuable feedback. Thank you for your time! I really enjoyed and appreciated working with you.

Furthermore, I am grateful for the support of my friends. Finally, I would like to express my deepest gratitude to my family for their love, encouragement and support before and throughout my studies.

F. Erklärung

Ich versichere, dass ich diese Arbeit selbstständig verfasst und keine anderen als die angegebenen Quellen und Hilfsmittel benutzt habe.

Heidelberg, den 07. März 2024

Isabel Kantak